AD-A035 032 MOTOROLA INC SCOTTSDALE ARIZ GOVERNMENT ELECTRONICS DIV F/G 17/9
PERFORMANCE OF COHERENT-ON-RECEIVE SYNTHETIC APERTURE SIDE LOOK--ETC(U)
OCT 76 D E FRASER, G V MORRIS F42600-75-A-1861
UNCLASSIFIED GED-2213 USCG-D-109-76 NL

1 OF 2
AD
A035032

PREFACE

This test program was the product of the cooperative, dedicated effort of individuals representing a number of organizations. The authors would like to acknowledge the contributions of:

(1) Russel Vollmers and Lt. Les Wiley, United States Coast Guard for sponsoring and coordinating the entire effort.

(2) The U.S. Army Electronic Proving Ground test team commanded by Major Scamahorn.

(3) The Motorola test team led by Don Fraser.

(4) John Estes and his staff at the University of California at Santa Barbara for ground truth.

(5) Motorola Management for supporting the research and development of the synthetic array radar equipment.

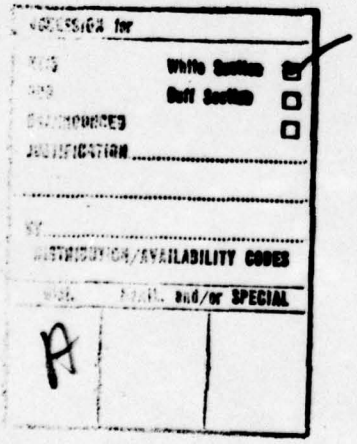

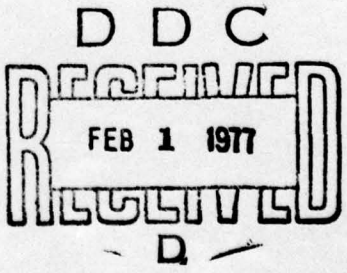

(12) 165p.

(19)

(18)

Technical Report Documentation Page

1. Report No.	2. Government Accession No.	3. Recipient's Catalog No.
USCG-D-109-76		

(6)

4. Title and Subtitle
Performance of Coherent-on-Receive Synthetic Aperture Side Looking Airborne Radar

(11)

5. Report Date
October 1976

6. Performing Organization Code
80063

(14)

8. Performing Organization Report No.
GED-2213

(10)

7. Author(s)
D. E. Fraser and G. V. Morris

9. Performing Organization Name and Address
Motorola Inc., Government Electronics Div.*
8201 E. Mc Dowell Rd.
Scottsdale, Az. 85252

10. Work Unit No. (TRAIS)

11. Contract or Grant No.

(9)

13. Type of Report and Period Covered
Final Report.
April - July 1976

12. Sponsoring Agency Name and Address
U.S. Department of Transportation
United States Coast Guard
Office of Research and Development
Washington, D.C. 20590

14. Sponsoring Agency Code

(15)

15. Supplementary Notes *Under contract to:
United States Army Electronic Proving Ground
Ft. Huachuca, Az. 85613

FH2600-75-A-1861

P1-1

16. Abstract

The Coast Guard's Oil Slick Detection Side Looking Airborne Radar was modified to add a synthetic aperture mode. The modification used the technologies of real time digital synthetic aperture processing and making the existing magnetron transmitter/receiver unit coherent-on-receive. Improvement in resolution by a factor of ten and imaging of the ocean surface and moving vessels were demonstrated. Synthetic oil slicks, generated using Oleyl alcohol, were detected by the synthetic aperture radar at a range of 25 km under 10 knot wind conditions and at 9 km under 4 knot wind. Comparison imagery was taken by a standard AN/APS-94D. The OSDR provided greater detection ranges of oil, due primarily to the higher sea return of the 8-foot vertically polarized antenna of the OSDR. The AN/APS-94D, with the higher gain 16-foot horizontally polarized antenna, detected vessels at longer ranges.

17. Key Words	18. Distribution Statement
Coherent-on-Receive Synthetic Aperture Radar Oil Slick Detection Side Looking Airborne Radar	Document is available to the U.S. public through the National Technical Information Service, Springfield, Virginia 22161

19. Security Classif. (of this report)	20. Security Classif. (of this page)	21. No. of Pages	22. Price
Unclassified	Unclassified		

Form DOT F 1700.7 (8-72)

401679

LB

METRIC CONVERSION FACTORS

Approximate Conversions to Metric Measures

Symbol	When You Know	Multiply by	To Find	Symbol
		LENGTH		
in	inches	*2.5	centimeters	cm
ft	feet	30	centimeters	cm
yd	yards	0.9	meters	m
mi	miles	1.6	kilometers	km
		AREA		
in^2	square inches	6.5	square centimeters	cm^2
ft^2	square feet	0.09	square meters	m^2
yd^2	square yards	0.8	square meters	m^2
mi^2	square miles	2.6	square kilometers	km^2
	acres	0.4	hectares	ha
		MASS (weight)		
oz	ounces	28	grams	g
lb	pounds	0.45	kilograms	kg
	short tons (2000 lb)	0.9	tonnes	t
		VOLUME		
tsp	teaspoons	5	milliliters	ml
Tbsp	tablespoons	15	milliliters	ml
fl oz	fluid ounces	30	milliliters	ml
c	cups	0.24	liters	l
pt	pints	0.47	liters	l
qt	quarts	0.95	liters	l
gal	gallons	3.8	liters	l
ft^3	cubic feet	0.03	cubic meters	m^3
yd^3	cubic yards	0.76	cubic meters	m^3
		TEMPERATURE (exact)		
°F	Fahrenheit temperature	5/9 (after subtracting 32)	Celsius temperature	°C

*1 in = 2.54 (exactly). For other exact conversions and more detailed tables, see NBS Misc. Publ. 286, Units of Weights and Measures, Price $2.25, SD Catalog No. C13.10:286.

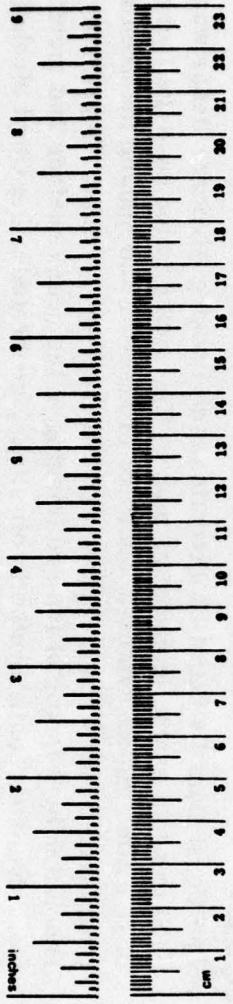

Approximate Conversions from Metric Measures

Symbol	When You Know	Multiply by	To Find	Symbol
		LENGTH		
mm	millimeters	0.04	inches	in
cm	centimeters	0.4	inches	in
m	meters	3.3	feet	ft
m	meters	1.1	yards	yd
km	kilometers	0.6	miles	mi
		AREA		
cm^2	square centimeters	0.16	square inches	in^2
m^2	square meters	1.2	square yards	yd^2
km^2	square kilometers	0.4	square miles	mi^2
ha	hectares (10,000 m^2)	2.5	acres	
		MASS (weight)		
g	grams	0.035	ounces	oz
kg	kilograms	2.2	pounds	lb
t	tonnes (1000 kg)	1.1	short tons	
		VOLUME		
ml	milliliters	0.03	fluid ounces	fl oz
l	liters	2.1	pints	pt
l	liters	1.06	quarts	qt
l	liters	0.26	gallons	gal
m^3	cubic meters	35	cubic feet	ft^3
m^3	cubic meters	1.3	cubic yards	yd^3
		TEMPERATURE (exact)		
°C	Celsius temperature	9/5 (then add 32)	Fahrenheit temperature	°F

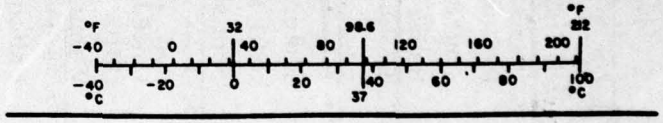

CONTENTS

CONTENTS (Cont)

CONTENTS (Cont)

ILLUSTRATIONS

TABLES

1. INTRODUCTION

For several years, Motorola has been developing real-time processing techniques applicable to Synthetic Aperture Radar (SAR). During 1973, design and fabrication was begun on a "modification kit" which could be installed on an AN/APS-94D or one of the AN/APS-94D derivative systems such as the Coast Guard's Oil Slick Detection Radar (OSDR). The modifications and reasons are described in detail in Section 3. The principal changes are:

a. Add motion sensors to the antenna.

b. Make the transmitter coherent-on-receive.

c. Substitute a synthetic array processor for the one previously in the system.

d. Modify the display sweeps to accommodate different data rates.

Synthetic processing theory is based on the condition that all objects on the ground are fixed with respect to each other. As explained in paragraph 3.1.1.4, the imagery process is degraded for objects not satisfying this condition. Target motion causes the image to be offset from its true position by an amount proportional to the radial velocity. For radial velocities greater than approximately 2 knots, detections will not be achieved by conventional synthetic array processing. The over water missions of the Coast Guard require the detection of various surface targets independent of the target velocity at various sea states.

During 1975, Motorola devised a relatively simple modification to its synthetic array processor (which at this time was nearing completion) to demonstrate an over water capability. The object of this modification, described in paragraph 3.1.1.5, is to provide detection of all targets, fixed or moving. Although not optimized and having a 6 dB detection sensitivity loss (which would be eliminated in any operational system), Motorola believed the "over water mode" to be satisfactory to confirm the concept and recommended that a test program be undertaken.

Contract F42600-75-A-1861 was initiated to flight test these concepts. The program involved modifying the Coast Guard's Oil Slick Detection Radar (OSDR) to incorporate a synthetic aperture processor, installing the radar on an Army C-47 aircraft, and conducting a flight test of the modified radar. The flight test program was conducted from March through May 1976. A standard AN/APS-94D in an Army Mohawk was also flown on some of the ocean mapping missions to obtain comparison imagery.

2. PROGRAM OBJECTIVES

The primary objective of this program was to examine the application of synthetic aperture radar processing for detecting and mapping targets of interest to the Coast Guard on the surface of the ocean at various sea states and aircraft velocities. A list of the specific objectives follows:

a. Demonstrate resolution improvement of an SAR.

b. Determine the best approach to solving motion compensation and clutter lock problems.

c. Maximum detection ranges for boat and ship targets.

d. Maximum detection range for oil slick detection in various sea states.

e. Evaluate the effects of an unstabilized antenna.

f. Obtain comparison imagery between an AN/APS-94D and the SAR.

g. Explain any image degradation.

h. Feasibility of using SAR with an unstabilized 4-foot antenna.

3. SYSTEM DESCRIPTION

In this section of the report, the following will be discussed:

a. A general theory of operation which describes the more important technical concepts and then unifies these concepts in simplified system block diagram.

b. A detailed system description in which numerous specific equipment parameters are presented.

c. Bench test results relating to the more significant parameters affecting synthetic processing.

d. Predicted detection and resolution performance.

3.1 GENERAL THEORY OF OPERATION

The system which Motorola has assembled on an internal research and development program is most commonly referred to as the "COR" system. COR is an acronym for Coherent-on-Receive. Actually the system has two independent technological advances which will be described separately:

a. Real time, digital, airborne synthetic array processing for achieving improved azimuth resolution.

b. Video coherency through the use of a magnetron transmitter in lieu of a more complex klystron or travelling wave tube transmitter.

3.1.1 Synthetic Array Processing

A number of references, such as the Radar Handbook[1], contain a description of the basic principles of synthetic array processing. The most common explanations draw analogies with antenna theory. Hence, the art has become known as "synthetic array processing" or "synthetic aperture processing". The antenna analogy will be briefly summarized so that the reader can relate the Motorola system to other approaches. In addition, the resolution improvement will be explained from the viewpoint of doppler signal processing. This latter method of explanation should be especially helpful because it provides a more direct insight into the system mechanization.

---

[1] Radar Handbook, Merril I. Skolnik, McGraw Hill, 1970, Chapter 23.

3.1.1.1 Antenna Analogy

In a side-looking radar, the antenna is essentially fixed to the aircraft, except for a small degree of angular motion which is sometimes incorporated to stabilize against air turbulence. The beam is pointed perpendicular to the aircraft flight path (figure 3-1). As the aircraft flies a straight line path, the ground to each side of the aircraft is mapped.

In a "real aperture radar", the radar returns are recorded directly on film to produce a continuous strip map image. A point reflector on the ground, with sufficient signal strength to be detected, will appear on the image as a spot with dimensions equal to a resolution cell. As shown in figure 3-1, the azimuth resolution is proportional to both range and the antenna beamwidth. Since antenna beamwidth is directly proportional to azimuth resolution and inversely proportional to antenna length, a long antenna will provide better azimuth resolution than a short antenna. In practice however, physical antennas with a length greater than 16 to 20 feet are difficult to install on aircraft; therefore another approach to azimuth resolution improvement is required.

It is possible, in concept, to construct a long array, L_S, (figure 3-2) by properly phasing a number of smaller radiators of length L_R. As the aircraft flies a distance, L_S, returns from a single antenna are put in the proper phase and then added to create a "synthetic aperture". In order to properly phase the returns, the radar transmitter/receiver must have a property called "coherence" which will be defined and described in a subsequent paragraph.

Figure 3-2 is also helpful in defining two terms commonly used in synthetic aperture processing discussions. "Unfocussed" processing assumes that the returns come from such a great distance compared to the dimensions of the array that the individual rays are parallel. This is the same simplification which usually applies in the design and test of physical arrays and is referred to as operating in the "far field" of the antenna pattern. Actually, "unfocussed" is somewhat of a misnomer. "Fixed-focus" or "focussed-at-infinity" would be more descriptive. The Motorola synthetic aperture processor is an "unfocussed" type.

As seen in figure 3-2, the wave emanating from a distant point, P, is actually spherical. If the ultimate in resolution improvement is to be achieved, the wave must be collected by a spherical antenna aperture. In practice, this is accomplished by adjusting the phase of the individual returns to generate the equivalent of a "focussed" spherical collector. Clearly the ideal radius of curvature of this synthetically generated collector is different for each range. This technique is actually "focussed at each individual range".

3.1.1.2 Doppler Beam Sharpening

A second method of describing how resolution improvement is achieved involves doppler beam sharpening. This description should be helpful since it relates more directly to the specific Motorola implementation.

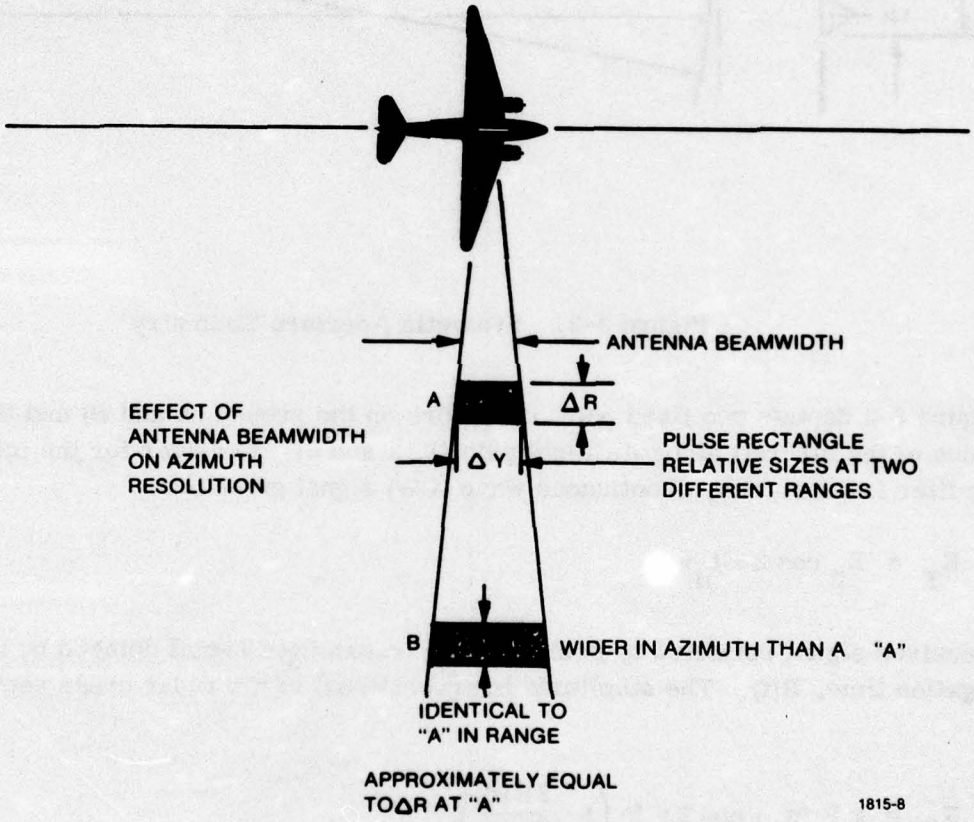

Figure 3-1. Real Aperture Resolution

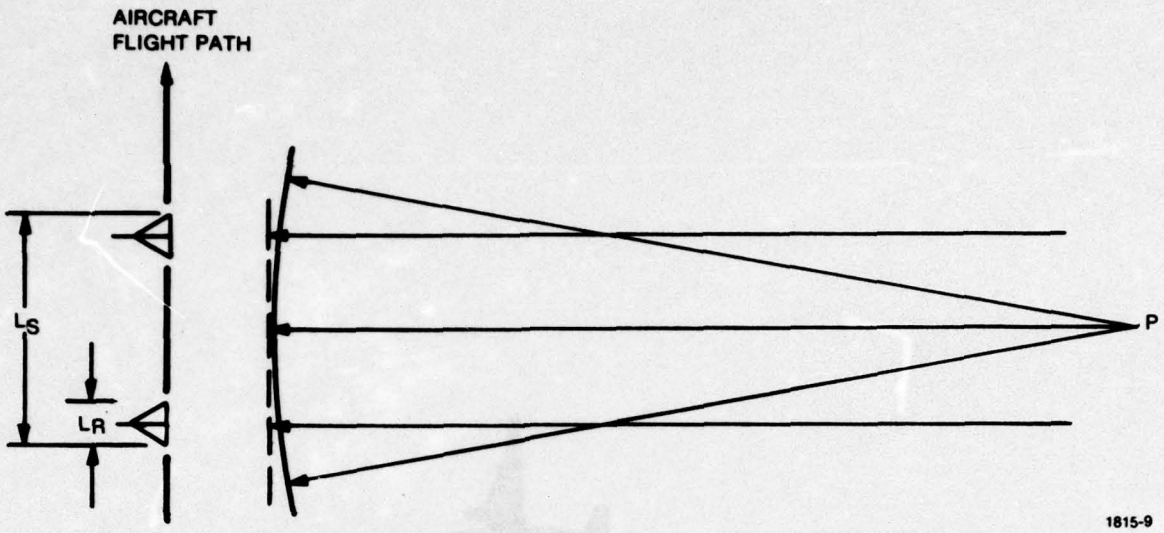

Figure 3-2. Synthetic Aperture Geometry

Figure 3-3 depicts two fixed point reflectors on the ground (A and B) and three sequential locations of the aircraft along its flight path (1, 2 and 3). Consider for the moment that the transmitter is generating a continuous wave (CW) signal given by:

$$E_T = E_0 \cos 2\pi f_o t \tag{3-1}$$

The received signal reflected by point A is the transmitted signal delayed by the round trip propagation time, R(t). The amplitude is proportional to the radar cross section of point A, σ_T:

$$E_R = k E (\sigma_T) \cos 2\pi fo \left(t - \frac{2R(t)}{c}\right) \tag{3-2}$$

where c is the velocity of propagation. The video signal which results from mixing the return signal with a sample of the transmitted signal is given by:

$$E_{VA} = k E (\sigma_T) \cos \left(\frac{2 R(t)}{c}\right) 2\pi f_o \tag{3-3}$$

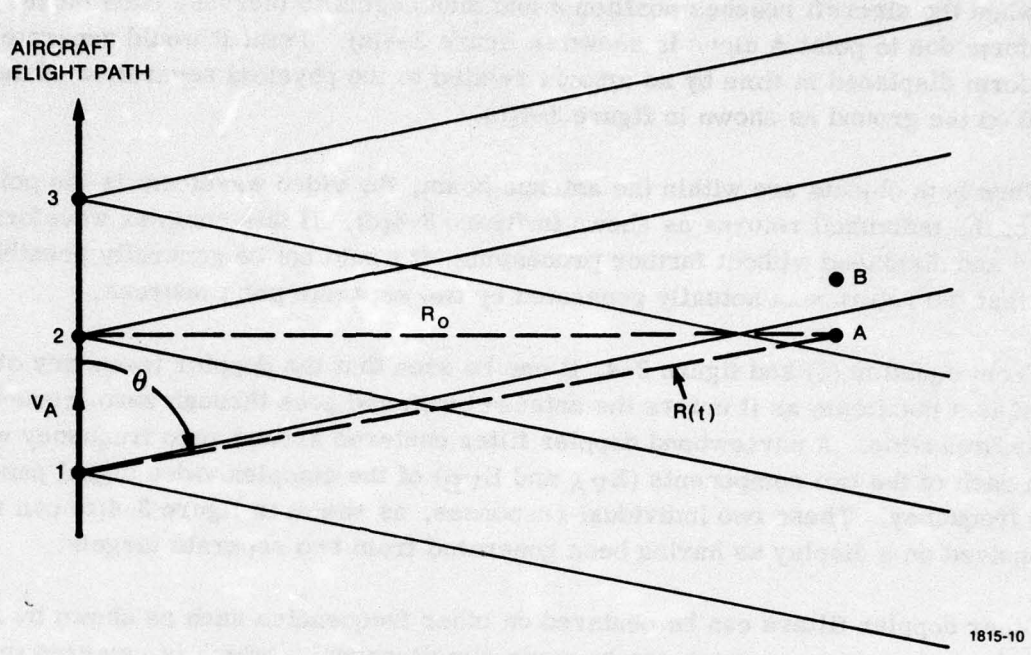

Figure 3-3. Doppler Processing Geometry

The type of transmitter/receiver described preserves the phase information and is referred to as "coherent". As the distance to point A, R(t), changes by a transmitter wavelength, then the video return varies through a complete sinusoidal cycle and thus is said to be "bipolar". Bipolar video differs from non-coherent radar unipolar video in which only the amplitude information $E(\sigma_T)$ is retained.

It might be helpful to examine the argument of the cosine function and consider the "instantaneous doppler frequency". Frequency is defined as the rate of change of phase with respect to time. In this case:

$$\text{Doppler frequency} = f_D = \frac{d}{dt}\left(\frac{2\ R(t)\ fo}{c}\right) = \left(\frac{2\ fo}{c}\right)\dot{R} \qquad (3\text{-}4)$$

where $\dot{R}$ = radial velocity. This is the familiar equation for doppler shift.

In a side-looking radar, the radial velocity cannot be assumed to be constant during the time the target is within the beamwidth as it is sometimes permissible to do in other types of radars. As can be seen from figure 3-3, the radial velocity at any instant is given by:

$$\dot{R} = V_A \cos\theta \qquad (3\text{-}5)$$

As the aircraft flies along the path of figure 3-3, R(t) decreases to its minimum value, R_o, when the aircraft reaches position 2 and then begins to increase once more. The video waveform due to point A alone is shown in figure 3-4(a). Point B would generate the same waveform displaced in time by an amount related to the physical separation of the objects A and B on the ground as shown in figure 3-4(b).

When both objects are within the antenna beam, the video waveform is the point-by-point sum of the individual returns as shown in figure 3-4(c). If this complex waveform were detected and displayed without further processing, it would not be generally possible to recognize that the return was actually generated by two separate point sources.

From equation (5) and figure 3-4, it can be seen that the doppler frequency of the point target is a maximum as it enters the antenna beam and goes through zero frequency at directly broadside. A narrowband doppler filter centered around zero frequency will respond when each of the two components (E_{VA} and E_{VB}) of the complex video signal pass through zero frequency. These two individual responses, as shown in figure 3-4(d) can readily be recognized on a display as having been generated from two separate targets.

Other doppler filters can be centered on other frequencies such as shown by figure 3-4(e). Therefore, two or more maps can be made simultaneously, which is referred to as a "multiple look" capability. The resulting individual maps are adjusted in time and overlayed to generate a single map. The multiple look capability will be discussed in more detail in paragraph 3.1.1.4.

In the system actually implemented by Motorola, the transmitted signal is not CW but pulsed. The received video is sampled at intervals equal to the transmitted pulse width as shown in figure 3-5(a). The signals in range cell N, which contains the return from point A, are depicted in figure 3-5(b). These are simply samples of the CW waveform described earlier and shown in figure 3-4.

3.1.1.3 Aircraft Motion Considerations

A synthetic array radar system must compensate for the departure of the aircraft from the idealized straight-line flight path assumed in the prior discussion. Figure 3-6 will be used to define the types of motions which are sensed and compensated for in the Motorola system. The axis "i" is the aircraft longitudinal axis, axis "j" is perpendicular to "i" and along the right wing, and axis "k" is perpendicular to both "i" and "j". To maintain a desired ground track in the presence of a cross wind, the aircraft must establish a heading into the wind. The average value or "DC component" of this difference between heading and flight path is defined as the "drift angle". About this average drift angle, an aircraft will exhibit short term angular excursions which will be referred to as "yaw".

The center of the antenna beam is not orthogonal to the array but has a small squint angle on the order of 2 degrees, which is a function of transmitter frequency. This angle is added to the drift angle in the corrections described below.

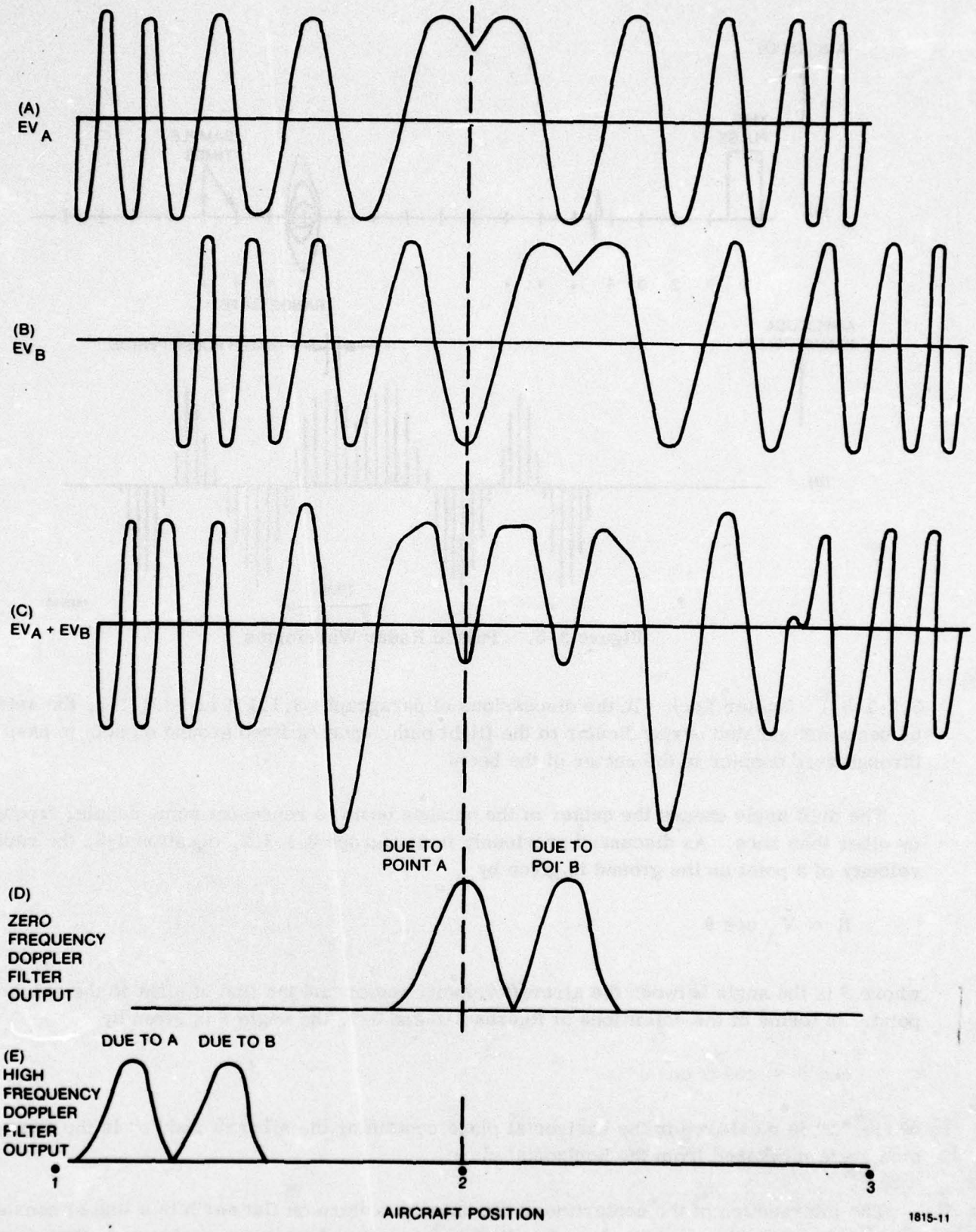

Figure 3-4. Video Waveforms

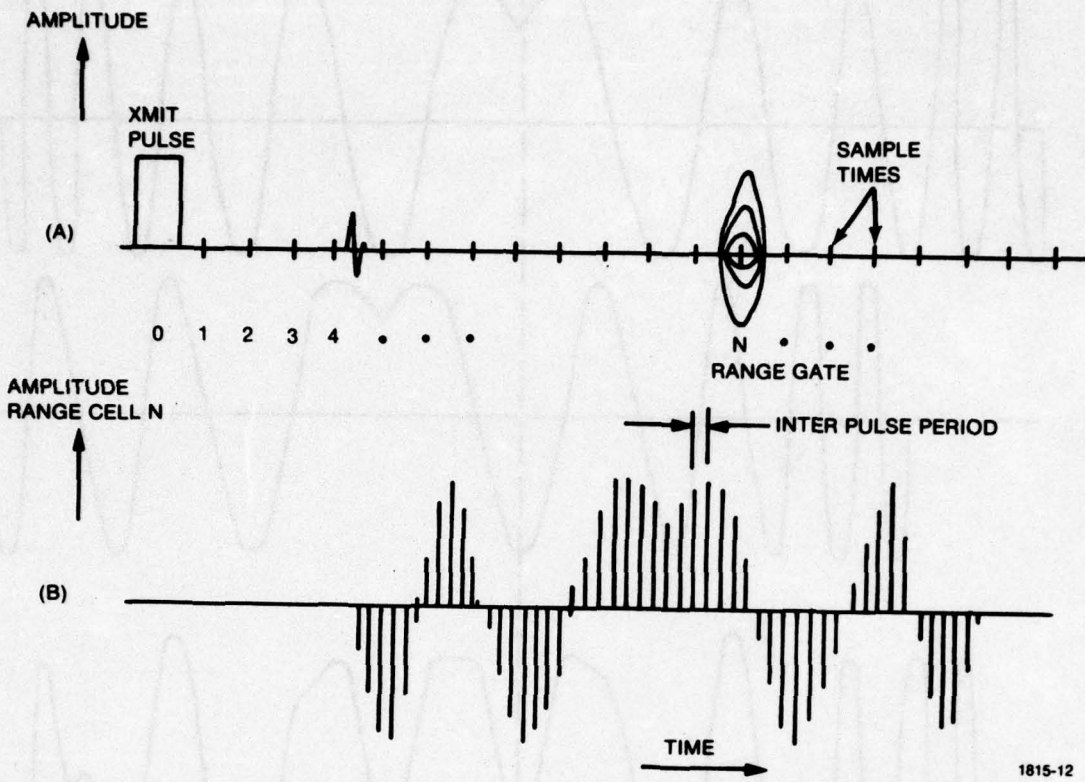

Figure 3-5. Pulsed Radar Waveforms

3.1.1.3.1 Clutter Lock. In the discussions of paragraphs 3.1.1.1 and 3.1.1.2, the antenna beam was pointed perpendicular to the flight path, causing fixed ground objects to pass through zero doppler in the center of the beam.

The drift angle causes the center of the antenna beam to represent some doppler frequency other than zero. As discussed previously in paragraph 3.1.1.2, equation 3-5, the radial velocity of a point on the ground is given by

$$\dot{R} = V_A \cos \theta \tag{3-6}$$

where θ is the angle between the aircraft velocity vector and the line of sight to the ground point. In terms of the definitions of figures 3-6 and 3-7, the angle θ is given by

$$\cos \theta = \cos \alpha \cos \epsilon \tag{3-7}$$

where "α" is measured in the horizontal plane containing the aircraft and "ϵ" is the depression angle measured from the horizontal plane.

The intersection of the centerline of the antenna pattern on flat earth is a line of constant angle "α". However, points along this line have varying depression angles and, therefore,

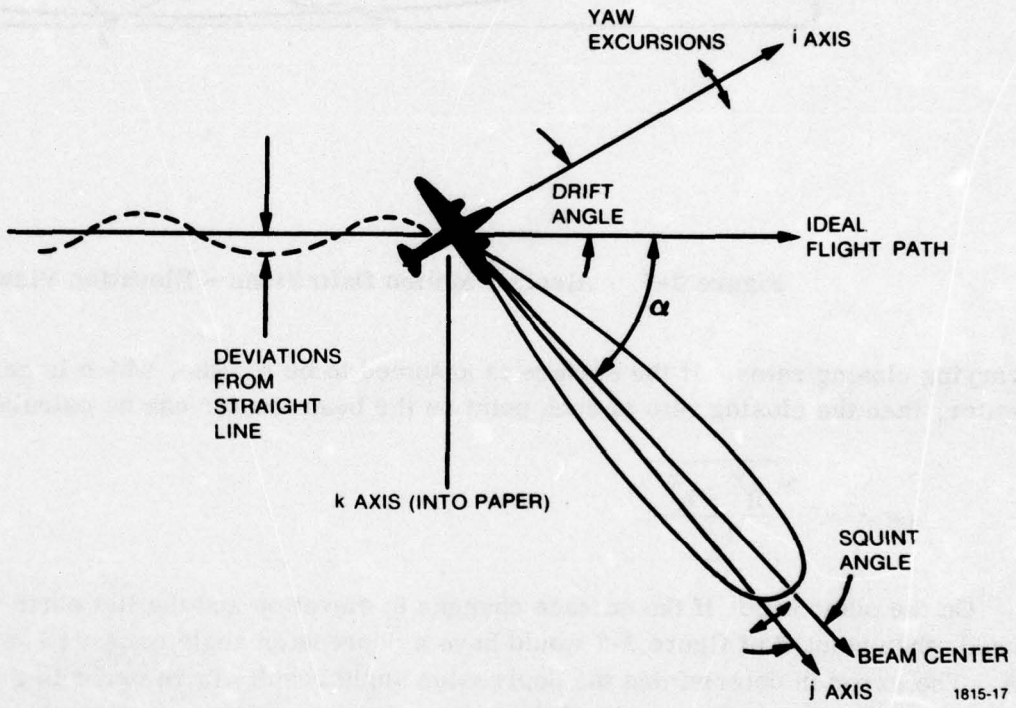

Figure 3-6. Aircraft Motion Definitions – Plan View

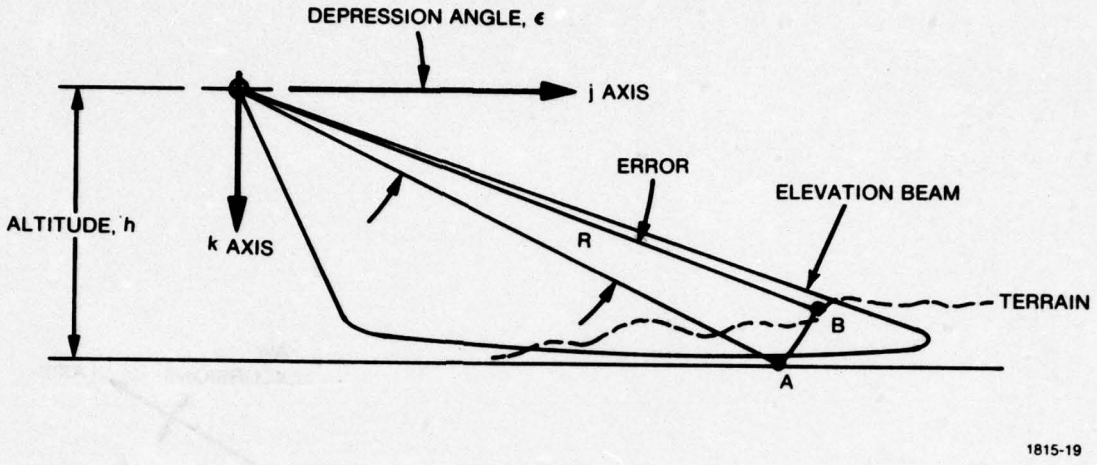

Figure 3-7. Aircraft Motion Definitions - Elevation View

varying closing rates. If the surface is assumed to be a plane, which is certainly valid over water, then the closing rate of each point on the beam center can be calculated by using

$$\cos \epsilon = \frac{\sqrt{R^2 - h^2}}{R} \tag{3-8}$$

On the other hand, if the surface changes in elevation and the flat earth assumption is used, then point B of figure 3-7 would have a depression angle computed as if it were at point A. The error in determining the depression angle results in an error in the computed doppler corresponding to the center of the beam. Improper determination of the beam center results in azimuth distortions of the map.

A better approach than the flat earth assumption for use over land with elevation variations is to measure the center of the actual received spectrum using a frequency discriminator. In the limit, individual discriminators would be used for each range cell. Hardware considerations temper the judgment on the number of discriminators to be provided. As a mechanization convenience, Motorola chose to implement the azimuth resolution improvement doppler filters at fixed frequencies near zero doppler. This then necessitates that the doppler frequency corresponding to the true center of the beam be determined and then the

received frequency spectrum be translated to place the center of the beam at zero doppler. Two fundamental methods have been implemented:

a. An open loop method in which the center frequency is calculated from aircraft drift angle and velocity inputs.

b. A closed loop method in which 64 frequency discriminator tracking loops adjust the center of the actual receive spectra to zero doppler. The closed loop method is commonly referred to as "clutter lock".

3.1.1.3.2 Yaw Compensation. The antenna contains a gyro which senses yaw motion of the array and mechanically drives the array to null these motions so that the antenna continues to point at the same angle.

3.1.1.3.3 Motion Compensation. As described in paragraph 3.1.1.2, a change in round trip path length to the target of a transmitter wavelength causes the bipolar video to go through a complete sinusoidal cycle. Therefore, if the aircraft were to deviate from the ideal flight path as shown in figure 3-6 by one quarter wavelength (8 millimeters), then the round trip path length change is one half wavelength, and a 180 degree phase error would be introduced. To sense these motions, three mutually perpendicular accelerometers are attached to the antenna. The displacement from the ideal flight path is calculated by integrating these accelerations and is used to correct the phase of the radar returns. A vertical gyro is also provided so that the gravity acceleration can be resolved into the proper coordinates and removed from the calculation.

3.1.1.4 Multiple Look Capability

As suggested previously in paragraph 3.1.1.2 and figure 3-4, it is possible to provide additional doppler filters which are tuned to correspond to other parts of the antenna beam besides the beam center. Figure 3-8 depicts a three-look mode showing the position of the filters within the physical beam. Thus, at all times, three distinct synthetic aperture maps are being produced simultaneously which are displaced from each other by the distance "d". The CRT traces for each of the three synthetic beams can be offset by "d" on the display so that the video from the same point on the ground is recorded on the same film spot.

Figure 3-9 depicts the instantaneous doppler frequency of a fixed target. As it passes through the main beam of the antenna, it is sequentially detected by filters, a, c and b. (In the diagram, one of the sets of sampling rate ambiguities or image frequencies is shown at the PRF of 750 Hz and depicted by dash lines.) The frequency locations of the filters in figure 3-9 are those which are appropriate for over land mapping.

Synthetic processing theory is based on the condition that all objects on the ground are fixed with respect to each other, i.e., not producing a doppler shift themselves. For objects not satisfying this condition, the imaging process is degraded. Target motion causes the image to be offset from its true position on the map in proportion to its velocity.

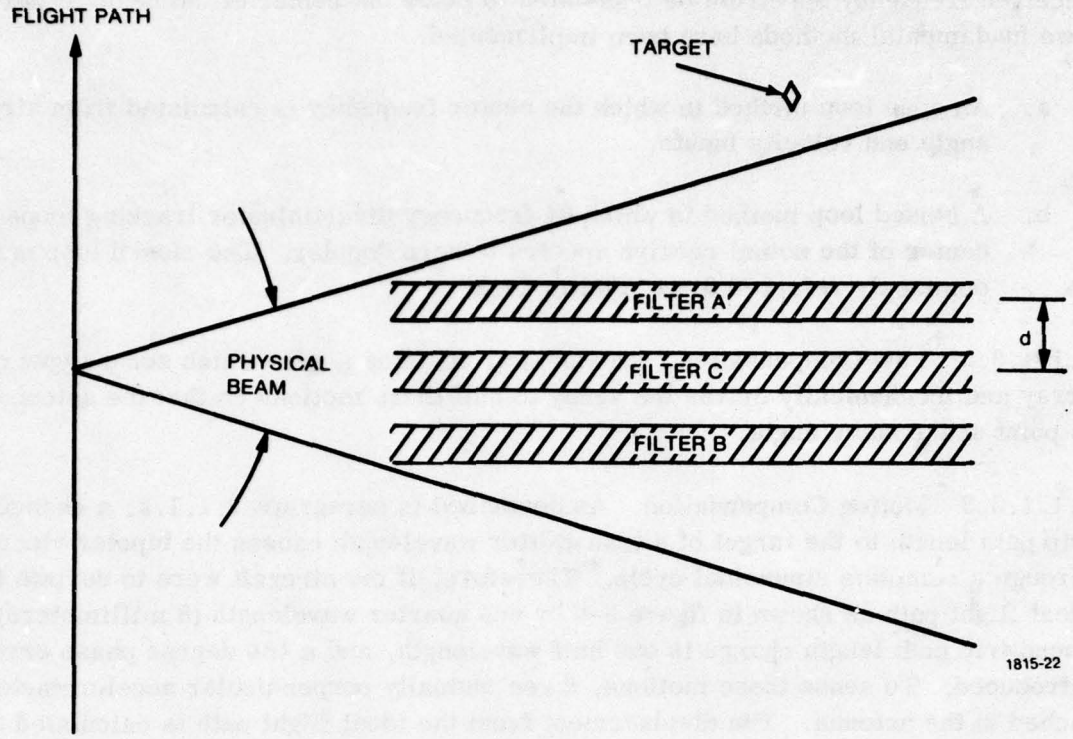

Figure 3-8. Multiple-Look Filters

Another effect illustrated in figure 3-9 is the loss of detection in filter b since the moving target did not achieve that specific doppler frequency during its time in the antenna main beam. For radial velocities greater than approximately 2 knots in the over land mode, detections will not be achieved in the main beam.

3.1.1.5 Modifications for Over Water Mode Feasibility Tests

The azimuth filters had been designed, fabricated, and tested to provide optimum results for land mapping missions. To suit the requirements of the Coast Guard, a different arrangement of the filters was indicated in order to detect both fixed and moving targets. Lack of time and funding ruled out major redesign. To demonstrate the system for possible Coast Guard use, the existing filter implementation was changed. Every other pulse period was discarded by setting the filter input to zero, which reduced the required spectrum coverage by a factor of 2 (from 750 Hz to 375 Hz). The reference function generator was modified by incorporating new ROM's to change the filter center frequencies to 32, 96, and 160 Hz. This filter spacing of 64 Hz was based on the fact that the doppler spread at the antenna 3 dB points is 64 Hz at the 150 knot nominal aircraft velocity. Additionally, the quadrature channel was disabled which causes the system to be unable to discriminate between positive and negative doppler frequencies. Therefore, each filter has a second response (image frequency) within the 375 Hz band, thereby effectively doubling the number of filters.

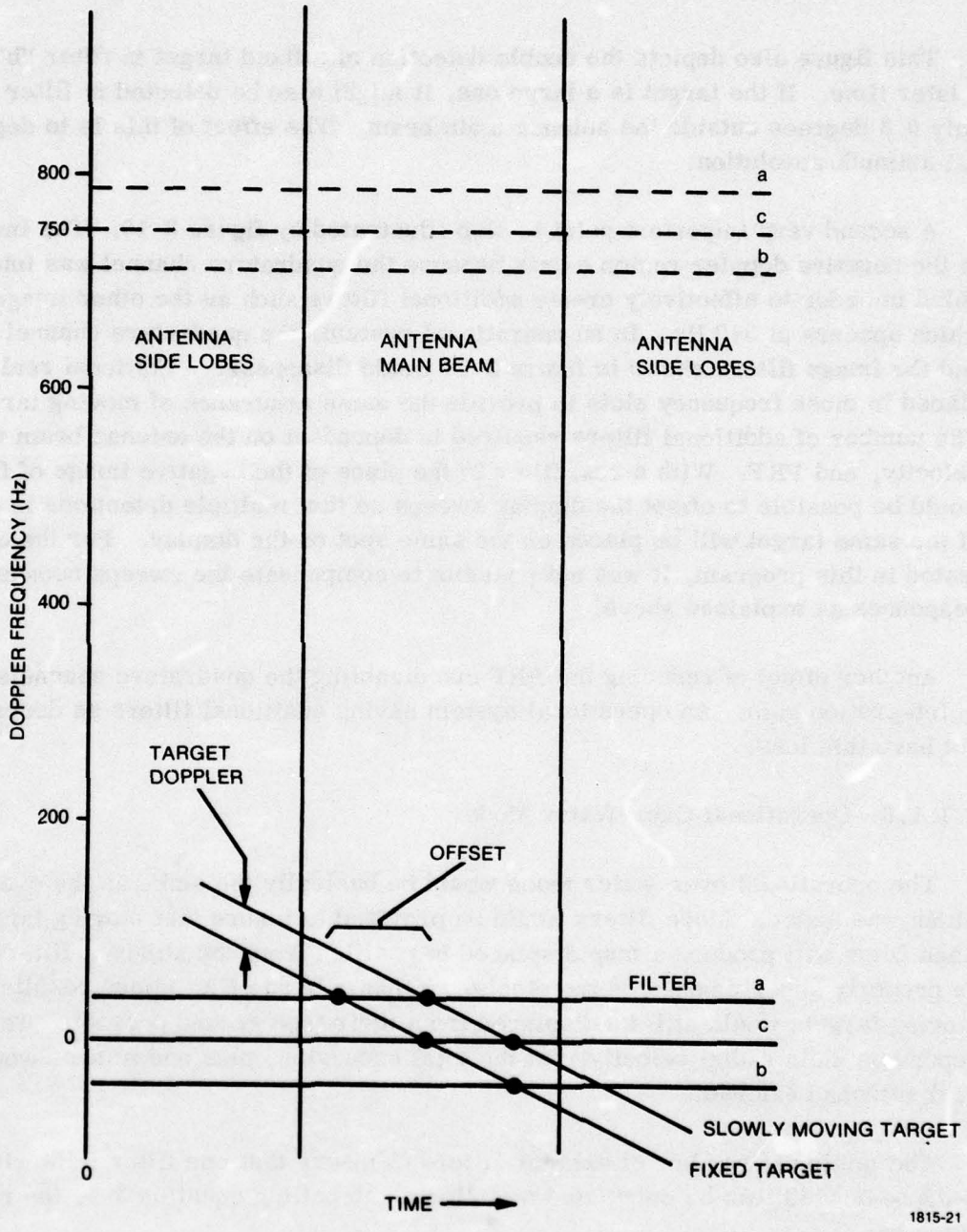

Figure 3-9. Over-Land Mode Filter Arrangement

This filter arrangement is shown graphically in figure 3-10. Any moving target will intercept at least one filter (either at base band or one of the image frequencies). Thus, detection of moving targets is assured although the apparent position will be displaced in azimuth anywhere within the antenna physical beamwidth, depending on target velocities, as described earlier.

This figure also depicts the double detection of a fixed target in filter "b" and its image at a later time. If the target is a large one, it might also be detected in filter "c" since it is only 0.3 degrees outside the antenna main beam. The effect of this is to degrade the apparent azimuth resolution.

A second very important point is also illustrated by figure 3-10. The image of filter "b" in the negative doppler region exists because the quadrature channel was intentionally disabled in order to effectively create additional filters such as the other image of filter "b" which appears at 340 Hz. In an operational system, the quadrature channel would be used, and the image filters shown in figure 3-10 would disappear. Additional real filters would be placed in those frequency slots to provide the same assurance of moving target detection. The number of additional filters required is dependent on the antenna beam width, aircraft velocity, and PRF. With a real filter in the place of the negative image of filter "b", it would be possible to offset the display sweeps so that multiple detections in different filters of the same target will be placed on the same spot on the display. For the over-water mode tested in this program, it was not possible to compensate the sweeps because of the image responses as explained above.

Another effect of reducing the PRF and disabling the quadrature channels was a 6 dB loss in integration gain. An operational system having additional filters as described above would not have this loss.

3.1.1.6 Operational Over-Water Mode

The operational over-water mode would be basically the same as the over-water mode which was tested. More filters would be provided to insure that moving targets are not lost. Each filter will produce a map displaced in position from the adjacent filters. Each map will be properly superimposed on the display so that only one film image results. However, moving targets would still be displaced from their true ground position. The amount would depend on their radial velocity, but the total excursion, plus and minus, would not exceed the real antenna beamwidth.

The minimum number of azimuth filters to insure that one filter falls within the antenna 3-dB beamwidth can be calculated as follows. Recalling equation 3-5, the radial velocity is given by:

$$\dot{R} = V_A \cos \theta \qquad (3\text{-}9)$$

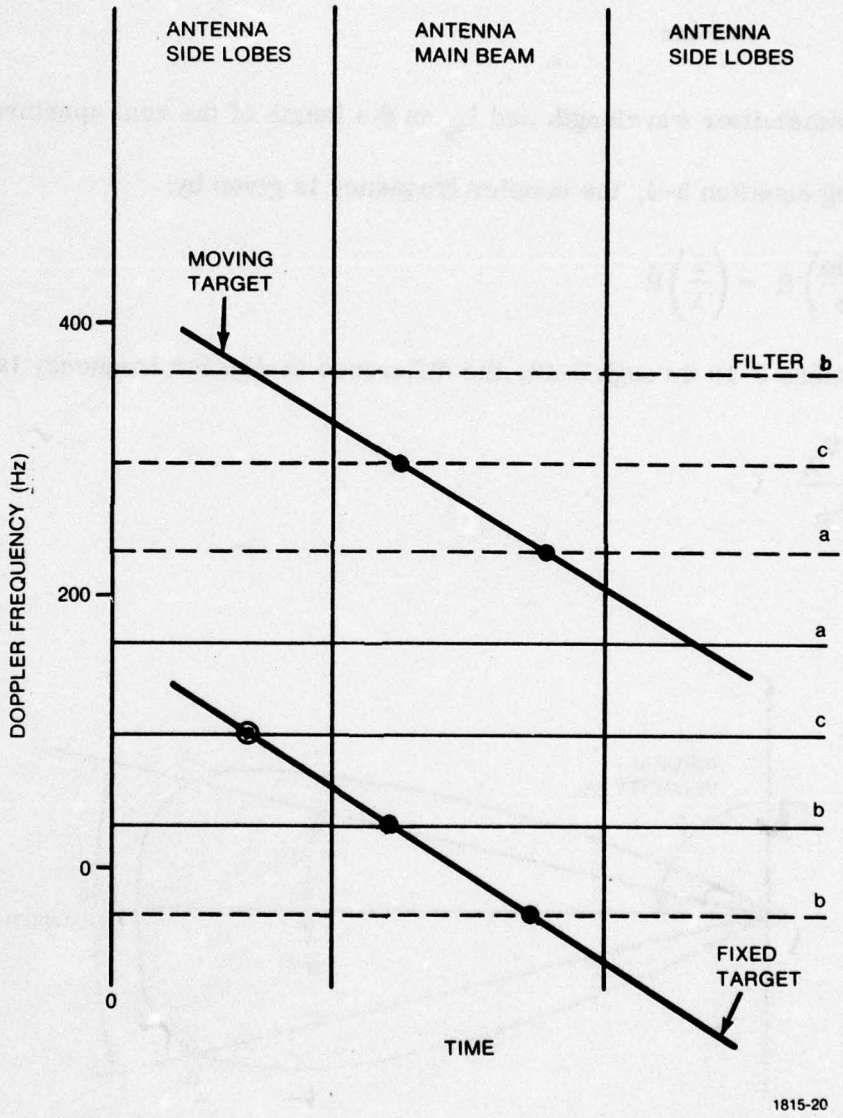

Figure 3-10. Over-Water Mode Filter Arrangement

Using the definitions of figure 3-11, the difference in radial velocity between points A and B is given by:

$$\Delta\dot{R} = V_A W \tag{3-10}$$

The antenna beamwidth is given by the following relationship:

$$W = \frac{\lambda}{L_R} \quad \text{radians} \tag{3-11}$$

where λ is the transmitter wavelength and L_R is the length of the real aperture.

Also recalling equation 3-4, the doppler frequency is given by:

$$f_D = \left(\frac{2\,fo}{c}\right)\dot{R} = \left(\frac{2}{\lambda}\right)\dot{R} \tag{3-12}$$

Combining equations 3-10 through 3-12, the difference in doppler frequency is given by:

$$\Delta f_D = \frac{2V_A}{L_R} \tag{3-13}$$

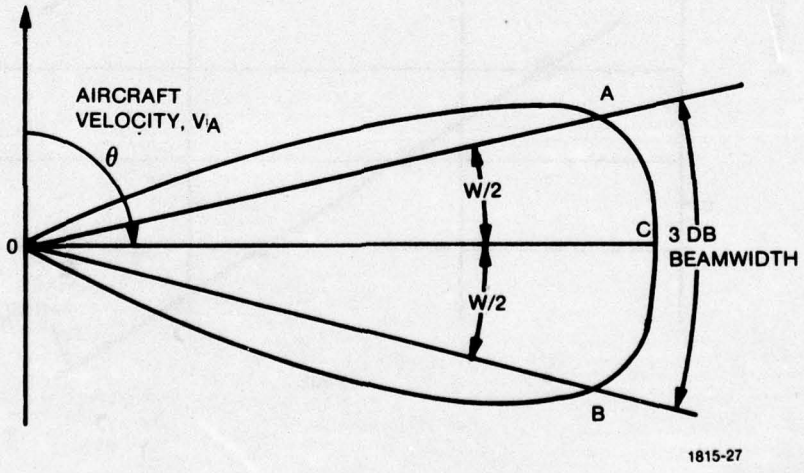

Figure 3-11. Antenna Beam Geometry

This frequency difference represents the bandwidth that the doppler from the target will sweep as the target passes through the antenna beamwidth. Moving targets contribute to the total radial velocity and can cause this swept bandwidth to lie anywhere within the total unambiguous doppler bandwidth of the radar, which is equal to the PRF. Therefore, the minimum number of filters is given by:

$$N_{min} = \frac{PRF}{\Delta f_D} = \frac{PRF\ L_R}{2\ V_{Amin}} \text{ rounded up to the nearest higher integer.} \quad (3\text{-}14)$$

where V_{Amin} is the minimum aircraft velocity.

One filter would be positioned to correspond to point C of figure 3-11, and the others would be spaced at intervals of Δf_D. This minimum filter spacing would insure detection of moving targets but would only be a single look system and not have the image enhancement provided by multiple looks. Therefore, two additional filters are recommended, providing a three-look map.

As can be appreciated from figure 3-11, placement of the multiple-look filters to correspond to points A and B would result in a system which would be very sensitive to yaw motions of the aircraft. The angular spacing between each of the filters in the three-look over land mode used in the test system is on the order of two milliradians. The beamwidth of the OSDR antenna is 16 milliradians. The beamwidth of a four foot antenna would be 32 milliradians.

If the same filter spacing were used in conjunction with an unstabilized four foot antenna having a beamwidth of 32 milliradians, then the ground patch being processed by each of the multiple-look filters would remain within the antenna 3 dB beamwidth for yaw motions of ±14 milliradians. To answer conclusively whether an unstabilized antenna is satisfactory, it is necessary to determine the yaw excursions at the antenna mounting point of the specific aircraft of interest while flying under those various operationally representative conditions for which radar operation is desired. As a point of reference, the experimental data from the B-66 which was used in the motion compensation analysis of Appendix A shows a yaw excursion of 15 milliradians rms.

3.1.1.7 4-Foot Antenna Tradeoffs

A 4-foot antenna has been considered for future radars because of the potential for size and weight reduction. The primary tradeoffs, which are discussed in more detail below and summarized in table 3-1, are as follows:

a. Detection.

Table 3-1. Antenna Comparisons

	8-Foot	4-Foot	Notes
1. DETECTION			
a. Antenna Gain dB	35	32	
b. Normalized detection range (same transmitter power)	1.0	0.71	
c. Effective peak transmitter power, Rw (same detection range)	50	200	
2. RESOLUTION (meters)			
a. Real aperture mode	0.016 R	.032 R	R is range in meters
b. Synthetic aperture mode	$0.173\sqrt{R}$	$.173\sqrt{R}$	
3. SYNTHETIC PROCESSOR CHARACTERISTICS			
a. Moving target position uncertainty	±0.008R	±0.016R	
b. Number of azimuth filters	20	10	PRF = 1500, V_{MIN} = 300 ft/sec
4. ANTENNA MECHANICAL CHARACTERISTICS			
a. Mechanical stabilization	Yaw	Yaw	
b. Weight, pounds	275[1] 200[2]	125	[1] No redesign, includes motion sensor
c. Frontal area, sq. ft.	4[1] 2.4[2]	1.5	[2] Redesigned

b. Resolution.

c. Synthetic processing characteristics.

d. Antenna mechanical characteristics.

3.1.1.7.1 Detection. Using the 8-foot antenna as a reference, the 4-foot antenna will have 3 dB less one way gain. If all other parameters remain the same, then relative detection range is given by:

$$\frac{R_4}{R_8} = \sqrt[4]{\frac{G_4^2 P_4}{G_8^2 P_8}}$$

where G is the one way antenna gain, P is the transmitter peak power and the subscripts refer to the antenna size.

If the transmitter power is the same, then $R_4/R_8 = 0.71$. Similarly, if the transmitter of the 4-foot antenna is increased from the current 50 KW nominal so that the same detection range is maintained, then $P_4 = 4P_8 = 200$ KW.

3.1.1.7.2 Resolution. The azimuth resolution of the real aperture mode is

$$\Delta a = WR$$

where W is the antenna beamwidth and R is the range to the target.

The beamwidth is 16 milliradians for the 8-foot antenna and 32 milliradians for the 4-foot antenna.

The azimuth resolution of the synthetic aperture mode is:

$$\Delta a = \sqrt{\lambda R}$$

where λ is the transmitter wavelength. A transmitter wavelength of 3 cm (X-band) has been assumed. Note that the resolution is independent of antenna length.

3.1.1.7.3 Synthetic Processor Characteristics. The angular uncertainty in position caused by target motion, described in paragraphs 3.1.1.4, 3.1.1.5, and 3.1.1.6, is limited to a

total excursion equal to the real antenna beamwidth. Stated in terms of range, this uncertainty is:

$$\text{Uncertainty} = \pm \frac{WR}{2}$$

An expression for the minimum number of azimuth filters, which is a measure of processor complexity, was derived in paragraph 3.1.1.6 and is repeated below:

$$N_{min} = \frac{PRF\ L_R}{2\ V_{amin}} \text{ rounded up to the nearest higher integer}$$

where L_R is the length of the real aperture and V_{amin} is the minimum aircraft velocity.

A system was assumed in which the transmitter operated at 1500 Hz alternating pulses between the right and left antennas. A minimum aircraft velocity of 300 feet/sec was used in the calculation.

3.1.1.7.4 Antenna Mechanical Characteristics. An antenna unit similar to the OSDR was assumed, i.e., it is an independent, structurally sound unit which attaches to the aircraft at two hardpoints similar to a fuel tank or ordnance. The antenna unit therefore includes not only the left and right array, but the yaw compensation mechanism, motion sensors, radome, aircraft attachment hooks and structure and aerodynamic end caps.

If a specific aircraft were identified, it might be possible to work out a tailored weight saving installation. In considering various approaches, care must be exercised to get a valid comparison to insure that apparent antenna "weight savings" are not achieved by passing weight off to the airframe in the form of fairings, etc.

The weight and frontal area for the 8-foot antenna noted as "no redesign" is the existing OSDR antenna with the motion sensor package added. The width of the existing antenna was established by the swept volume requirements of the 16-foot AN/APS-94D antenna. By redesign with attention to weight control, it is estimated that 75 pounds could be saved.

As discussed in paragraph 3.1.1.6, a synthetic aperture mode appears feasible which will tolerate yaw motions of ±14 milliradians in a 4-foot antenna. What is not known is the expected yaw motions of the aircraft which would carry this radar. It was judged that yaw stabilization should be assumed in this tradeoff until more conclusive data is available.

3.1.2 Coherent-on-Receive

With a coherent receiver/transmitter, the echo pulses received back from a point reflector will appear at point A of figure 3-12 to have been gated from a continuous wave as shown in figure 3-13. As described in paragraph 3.1.1.2, the property of coherence is essential to being able to reconstruct the doppler waveforms and therefore provide resolution improvement. The pulsed power amplifier is usually a klystron or travelling wave tube. The cost of an amplifier tube is 10 to 20 times that of a magnetron. Also, multiple high-voltage supplies are usually required for the amplifier tubes. For these reasons, Motorola developed a transmitter/receiver built around a magnetron transmitter. The method for producing video which is suitable for synthetic array processing will now be described using figure 3-14.

The pulse train from the magnetron transmitter is non-coherent, i.e., the RF phase of successive pulses is random when compared to a continuous wave. Therefore, the IF phase appearing at the output of the AFC mixer will be non-coherent. Similarly, the echos returned from a stationary object and appearing as IF pulses at the output of the signal mixer will be non-coherent. However, these echose will be replicas of the transmitted signal delayed by the round trip propagation time to the object. By measuring the phase of each transmitter pulse relative to a CW source and applying this correction to each signal received, the output video can be made coherent.

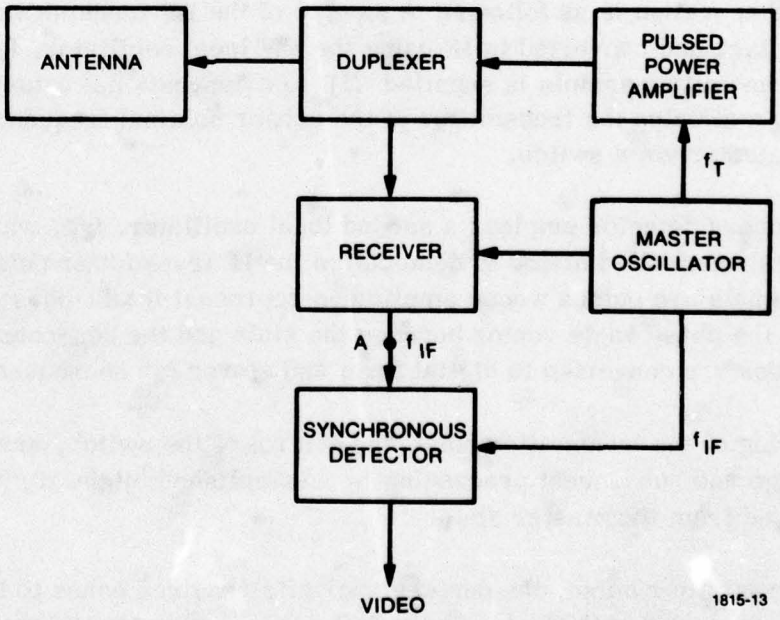

Figure 3-12. Coherent Radar

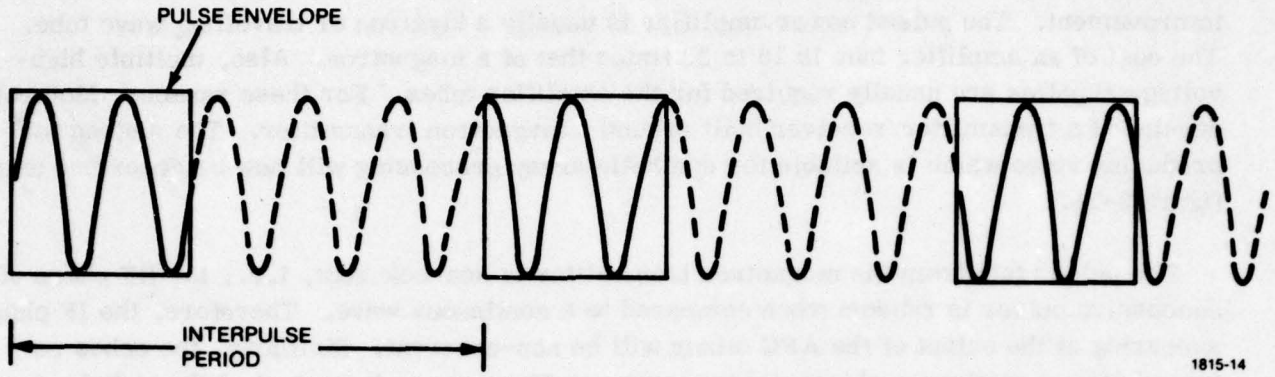

Figure 3-13. Coherent Train of IF Pulses

The detailed operation is as follows. A sample of the RF transmitter pulse is coupled into the AFC mixer and converted to IF using the CW local oscillator, f_{LO}. After amplification, the transmitter sample is supplied (1) to a conventional automatic frequency control loop which maintains the transmitter at the proper nominal frequency, and (2) to a synchronous detector via a switch.

The synchronous detector employs a second local oscillator, f_{IF}, which is derived from the same crystal-controlled stalo, to demodulate the IF transmitter pulse to video. The output video signals are pulses whose amplitudes represent the in-phase and quadrature components of the phase angle vector between the stalo and the non-coherent transmitter. These amplitudes are converted to digital form and stored for subsequent use.

The triggering of the transmitter pulse and control of the switch, analog-to-digital conversion, storage and subsequent processing is accomplished by the timing generator. The timing is derived from the master stalo.

After the transmitter pulse, the duplexer permits received echos to be converted to IF, using the same f_{LO}, and amplified. The switch now disconnects the transmitter IF sample and connects the signal IF to the synchronous detector. In-phase and quadrature components of the received signals are extracted as before and converted to digital form. The

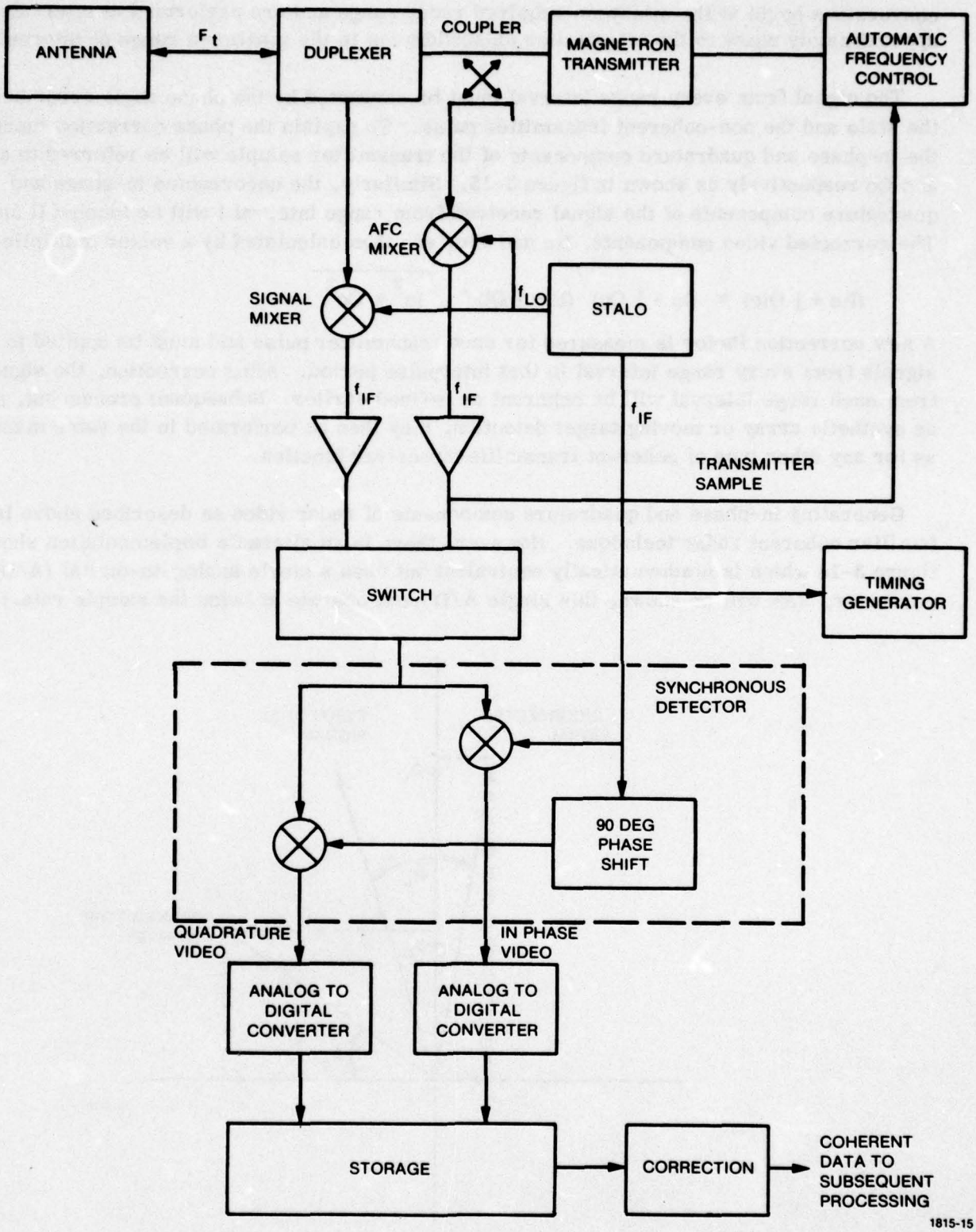

Figure 3-14. Coherent-on-Receive System

conversions begin at the minimum required radar range and are performed at intervals approximately equal to the transmitter pulsewidth out to the maximum range of interest.

The signal from every range interval must be corrected by the phase angle error between the stalo and the non-coherent transmitter pulse. To explain the phase correction function, the in-phase and quadrature components of the transmitter sample will be referred to as Io and Qo respectively as shown in figure 3-15. Similarly, the uncorrected in-phase and quadrature components of the signal received from range interval i will be labeled Ii and Qi. The corrected video components, Iic and Qic, are then calculated by a vector multiplication

$$(Iic + j\ Qic) = (Io - j\ Qo)\ (Ii + j\ Qi) / \sqrt{Io^2 + Qo^2}$$

A new correction factor is measured for each transmitter pulse and must be applied to the signals from every range interval in that interpulse period. After correction, the signals from each range interval will be coherent as defined earlier. Subsequent processing, such as synthetic array or moving target detection, may then be performed in the same manner as for any other type of coherent transmitter/receiver function.

Generating in-phase and quadrature components of radar video as described above is a familiar coherent radar technique. However, there is an alternate implementation shown in figure 3-16 which is mathematically equivalent but uses a single analog-to-digital (A/D) converter. (As will be shown, this single A/D must operate at twice the sample rate.)

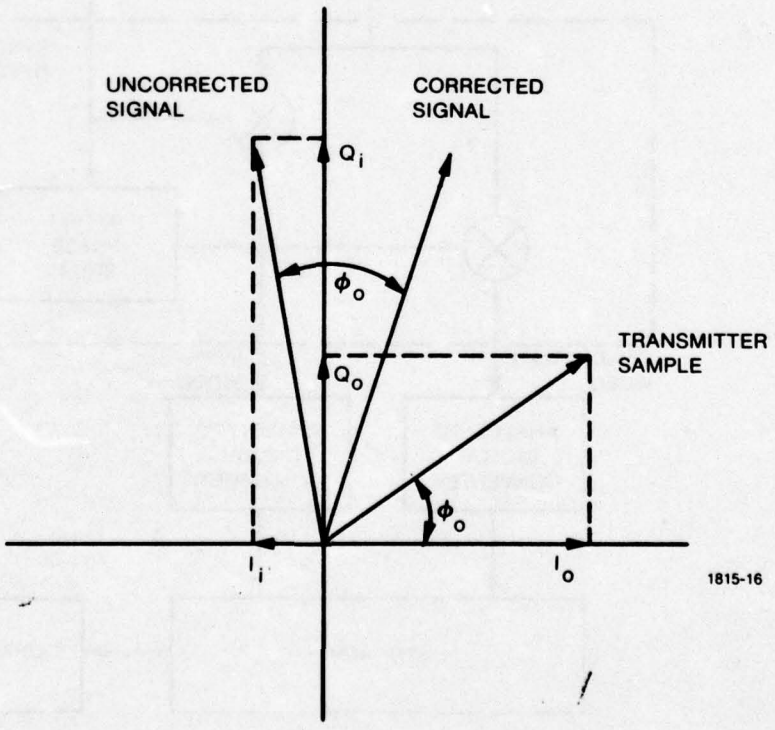

Figure 3-15. Video Phase Correction

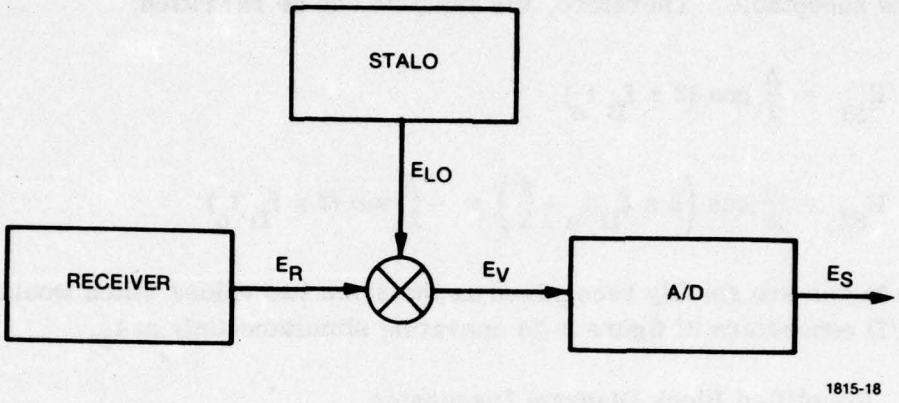

Figure 3-16. Alternate Video Implementation

Consider a received signal which is offset from the IF center frequency by the doppler shift, f_D:

$$E_R = A \cos 2\pi (f_{IF} + f_D)t \tag{3-16}$$

Let the other input to the mixer be at the IF center frequency plus an offset, f_B:

$$E_{LO} = \cos 2\pi (f_{IF} + f_B)t \tag{3-17}$$

Then the output of the mixer is given by:

$$E_V = \frac{A}{2} \cos 2\pi (f_D - f_B)t \tag{3-18}$$

If the A/D samples at t_o and $t_o + \tau/2$, where τ is the transmit pulse width, and if the offset frequency is chosen so that $f_B = 1/2\tau$, then the two video samples are:

$$E_{S1} = \frac{A}{2} \cos \left(2\pi f_D t_o - 2\pi \frac{t_o}{2\tau} \right) \tag{3-19}$$

$$E_{S2} = \frac{A}{2} \cos \left(2 \pi f_D t_o - 2 \pi \frac{t_o}{2\tau} + \pi f_D - \frac{\pi}{2} \right) \quad (3\text{-}20)$$

The term $(2 \pi t_o/2\tau)$ is a constant phase term appearing in both samples and may be disregarded. Also, since f_D is typically 100 Hz and $\tau = 0.2 \times 10^{-6}$ sec, ignoring the term $(2 \pi f_D \tau)$ is acceptable. Therefore, the samples can be rewritten:

$$E_{S1} = \frac{A}{2} \cos (2 \pi f_D t_o) \quad (3\text{-}21)$$

$$E_{S2} = \frac{A}{2} \cos \left(2 \pi f_D t_o - \frac{\pi}{2} \right) = - \frac{A}{2} \sin (2 \pi f_D t_o) \quad (3\text{-}22)$$

These terms are readily recognized as the same two values which would be generated by the two A/D converters of figure 3-14 operating simultaneously at t_o.

3.1.3 Simplified Block Diagram Discussion

Having now established some of the more important technical concepts, the simplified block diagram of figure 3-17 will now be discussed. The more significant additions to the Oil Slick Detection Radar, which were added for this program only and then removed, are shaded.

3.1.3.1 Antenna Unit

Motion sensors to perform the functions described in 3.1.1.3 were mounted on the OSDR antenna.

3.1.3.2 Receiver/Transmitter Unit

A crystal-controlled stable master oscillator was substituted for the klystron local oscillator. This assembly provides the CW coherent reference with which the transmitter pulse is compared to determine the phase correction. The single A/D method of extracting in-phase and quadrature video components, as described in paragraph 3.1.2, was implemented. During the receive time, the same synchronous detector and video amplifiers are used to process radar returns.

3.1.3.3 Signal Processor

The synthetic array processing functions, shown in figure 3-17, were housed in a new unit which was substituted for the OSDR processor unit for the duration of the test.

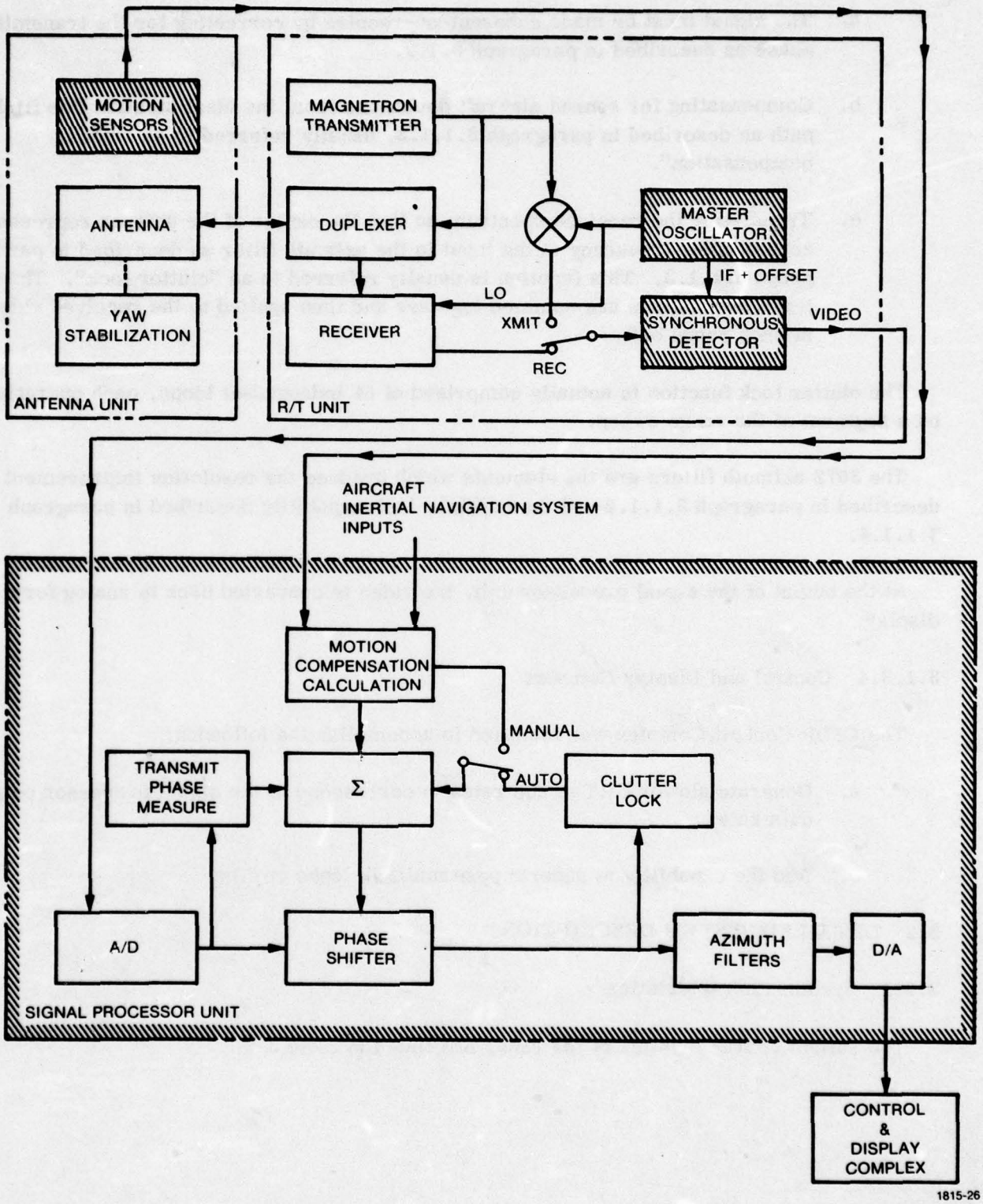

Figure 3-17. Simplified Block Diagram

Before doppler filtering, three phase corrections must be made:

a. The signal must be made coherent-on-receive by correcting for the transmitter phase as described in paragraph 3.1.2.

b. Compensating for sensed aircraft deviations from the ideal straight line flight path as described in paragraph 3.1.1.3, usually referred to as "motion compensation".

c. Translating the received spectrum so that the center of the antenna represents zero doppler frequency at the input to the azimuth filter as described in paragraph 3.1.1.3. This function is usually referred to as "clutter lock". These three corrections are summed together and then applied to the received video in each range cell.

The clutter lock function is actually comprised of 64 independent loops, each operating on a segment of the range sweep.

The 3072 azimuth filters are the elements which produce the resolution improvement described in paragraph 3.1.1.2 and the multiple-look capability described in paragraph 3.1.1.4.

At the output of the signal processor unit, the video is converted back to analog form for display.

3.1.3.4 Control and Display Complex

The OSDR Cockpit Complex was modified to accomplish the following:

a. Generate slower CRT sweep rates to correspond to the signal processor output data rate.

b. Add the capability to superimpose multiple looks on film.

3.2 DETAILED SYSTEM DESCRIPTION

3.2.1 System Characteristics

The salient characteristics of the radar are listed in table 3-2.

Table 3-2. Radar System Characteristics

Radar Type	Coherent-on-Receive, Side Looking
Transmitter:	
Power	45 KW min.
Frequency	9315 MHz
Pulse Width	0.2 usec
PRF	750 PPS
Antenna:	
Length	≈ 8 ft.
Gain	35 dB
Polarization	Vertical
Azimuth Beamwidth	0.9°
Elevation Pattern	$\text{Csc}^2 \theta \cos \theta$
Yaw Stabilization Range	±3°
Receiver:	
Noise Figure	13 dB maximum
Noise Bandwidth	5 MHz
IF Frequency	60 MHz
L.O. Freq. Stability	<1 part in 10^{10}, 1 sec. period
L.O. Phase Stability	0.1 radians, 1 msec period
AFC Error	<170 KHz
AGC Range	±6 dB
Video Output	2.3 MHz offset
Video Processing:	
Type	Digital, 6 bits A/D
Sampling Rate	9.23×10^6/sec.
Number of Range Bins	3072
Number of Looks	1, 2, or 3

Table 3-2. Radar System Characterisitcs (Cont)

Filter Bandwidth	0.015 x Va (Aircraft Velocity - ft./sec.) (~4.5 Hz Typically)
Peak Side Lobes	-30 dB max.
Processing Gain:	
Land Mode	20 dB nom.
Water Mode	14 dB nom.
Azimuth Resolution	Approach $\sqrt{\lambda R}$
Output Dynamic Range	Selectable
Output Detector	Linear or Logarithmic
Clutter Spectrum Compensation	Automatic, Calculated, or Multiple Filter
Motion Compensation	Mechanical Yaw Stabilization Electrical Platform Phase Correction
Display Format:	
Type	Real Time, Permanent Film
Swath Widths	25, 50, or 100 Km
Range Delay	0, 20, 40, or 60 Km

3.2.2 Receiver/Transmitter

Figure 3-18 is a block diagram of the Receiver/Transmitter. The R/T is a basic AN/APS-94D unit that was modified mainly in the areas of the Local Oscillator, Automatic Frequency Control, and IF circuits. A brief description of these changes follows.

The basic reference for the system is a very stable, oven-controlled 5 MHz Crystal Oscillator. All system timing is derived from this one source, as is the local oscillator, by the use of a X 1875 frequency multiplier. This approach was chosen to obtain the short term phase stability required by the SAR.

The system used the AN/APS-94 Transmitter with only minor changes in the modulator to slightly widen the pulse width to 0.2 μsec. The standard L6543A magnetron was used. The automatic frequency control was modified to ensure that the tuning rates would be slow compared to the system integration times.

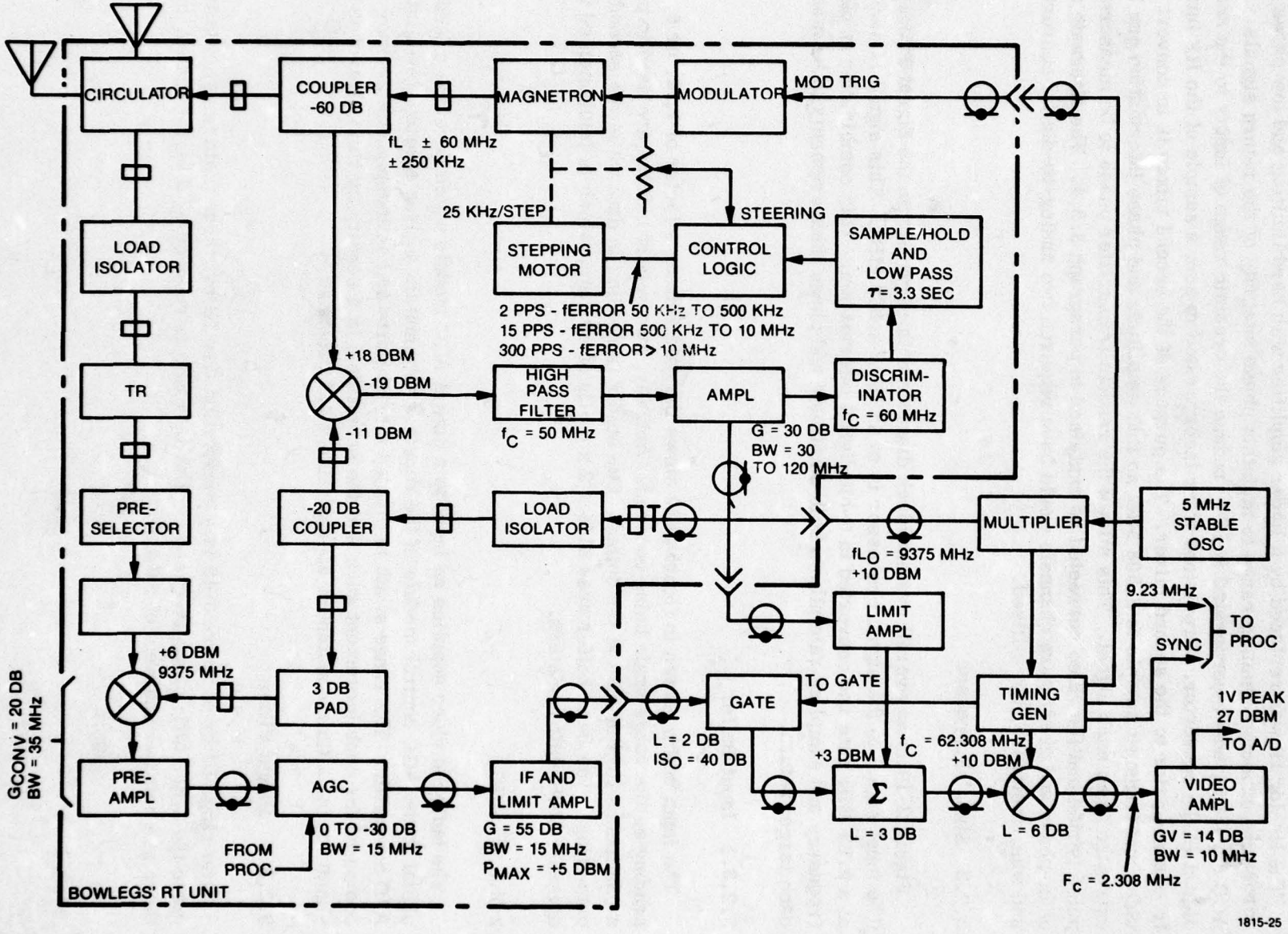

Figure 3-18. R/T Unit Block Diagram

The lin-log IF was replaced by a linear amplifier with hard limiting and low phase shift across the expected dynamic range to maintain phase integrity of the return signals. An AGC capability was incorporated at IF to reduce the dynamic range of inputs to the analog-to-digital (A/D) converter. Provisions were incorporated to sum a sample of the RF into the IF channel prior to the second mixer. The purpose of the second mixer is to convert the video and transmit sample to 2.308 MHz so that amplitude and phase information can be extracted from each signal. This allows the random transmitter phase to be measured each pulse period and the video corrected as explained in paragraph 3.3.4. The alternate approach of in-phase and quadrature channels would have required two analog-to-digital converters and was, therefore, not utilized.

3.2.3 Signal Processor

Figure 3-19 is an overall system block diagram with emphasis on the Signal Processor. The input signal to the signal processor is at an IF of 2.308 MHz. This signal is sampled at a 9.23 MHz rate and converted to 6-bit digital information. This combination of offset frequency and sampling rate allows both amplitude and phase measurements to be made for each target return.

3.2.3.1 Input Buffer

The input buffer shown in figure 3-19 slows the data rate by a factor of 2, 4, or 6, depending on the range scale being covered. Actually, two sets of buffers are used to provide a continuous flow of data at the output. One buffer is reading in data while the second is outputting. The input buffer uses 6144 x 2 x 6 bits of storage, which is implemented with dynamic MOS shift registers.

3.2.3.2 AGC

The buffered video supplies an input to a digital AGC module which develops a feedback signal to the AGC control module in the receiver to maintain a given average level into the A/D converter. The range swath is divided into 64 parts and an independent average is computed for each increment such that the output then is a sensitivity time control (STC) signal having a time constant of approximately 2.7 seconds.

3.2.3.3 Range Filter

The range filter of figure 3-19 is a convolution type filter whose main function is to remove the 2.308 MHz offset frequency. The data rate is reduced by a factor of two, but there are now two channels of data.

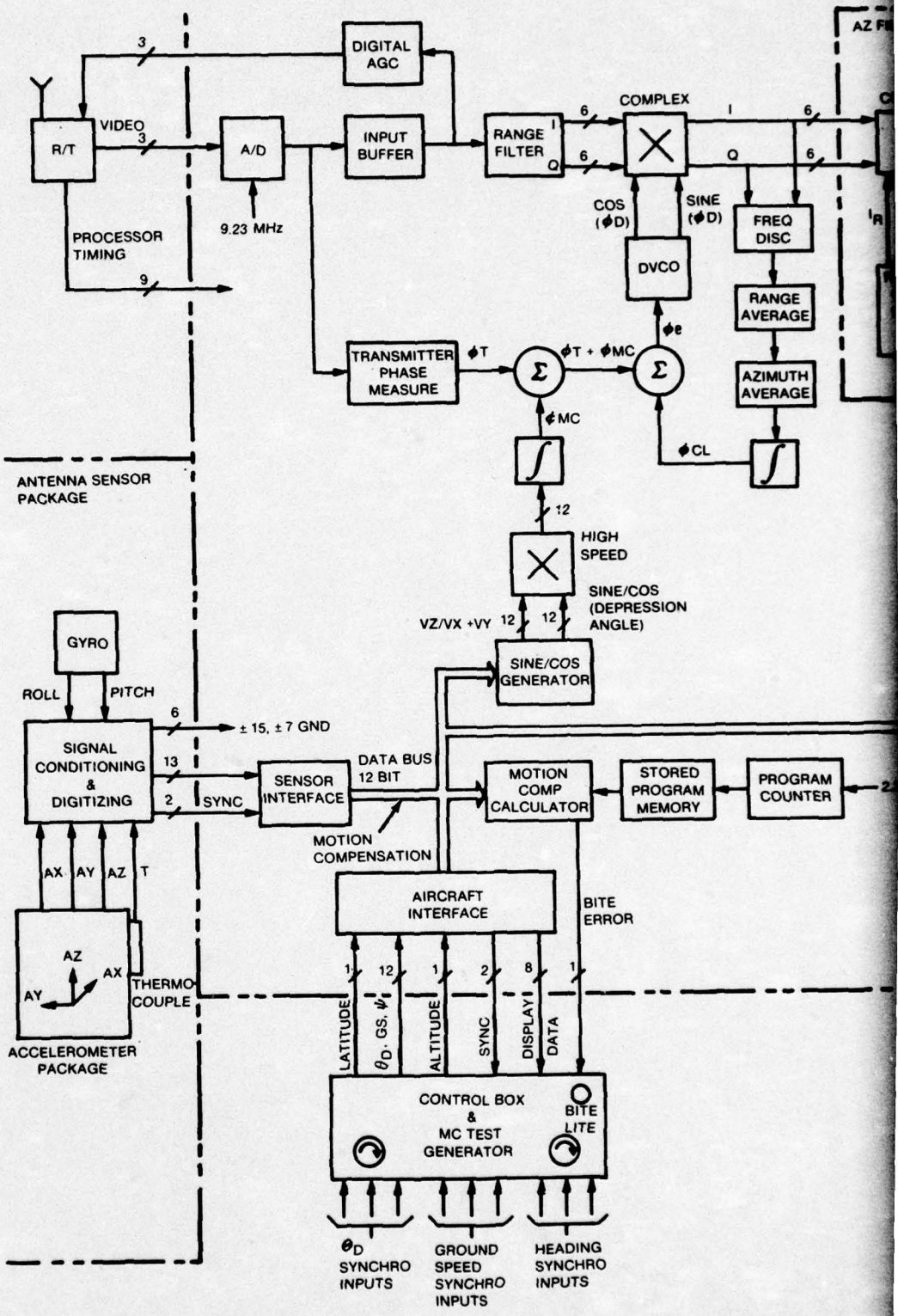
DIGITAL AGC
3
R/T
VIDEO
3
A/D
INPUT BUFFER
RANGE FILTER
I
Q
6
6
COMPLEX
I
Q
6
6
COS (ϕD)
SINE (ϕD)
FREQ DISC
DVCO
RANGE AVERAGE
AZIMUTH AVERAGE
9.23 MHz
PROCESSOR TIMING
9
TRANSMITTER PHASE MEASURE
ϕT
ϕT + ϕMC
ϕe
ϕMC
ϕCL
ANTENNA SENSOR PACKAGE
12
HIGH SPEED
SINE/COS (DEPRESSION ANGLE)
VZ/VX +VY 12
12
SINE/COS GENERATOR
GYRO
ROLL
PITCH
6
± 15, ± 7 GND
SIGNAL CONDITIONING & DIGITIZING
13
2
SYNC
SENSOR INTERFACE
DATA BUS 12 BIT
MOTION COMP CALCULATOR
STORED PROGRAM MEMORY
PROGRAM COUNTER
MOTION COMPENSATION
AX
AY
AZ
T
AIRCRAFT INTERFACE
BITE ERROR
AZ
AX
AY
THERMO COUPLE
ACCELEROMETER PACKAGE
1
12
1
2
8
1
LATITUDE
θD, GS, ψ
ALTITUDE
SYNC
DISPLAY
DATA
CONTROL BOX & MC TEST GENERATOR
BITE LITE
θD SYNCHRO INPUTS
GROUND SPEED SYNCHRO INPUTS
HEADING SYNCHRO INPUTS

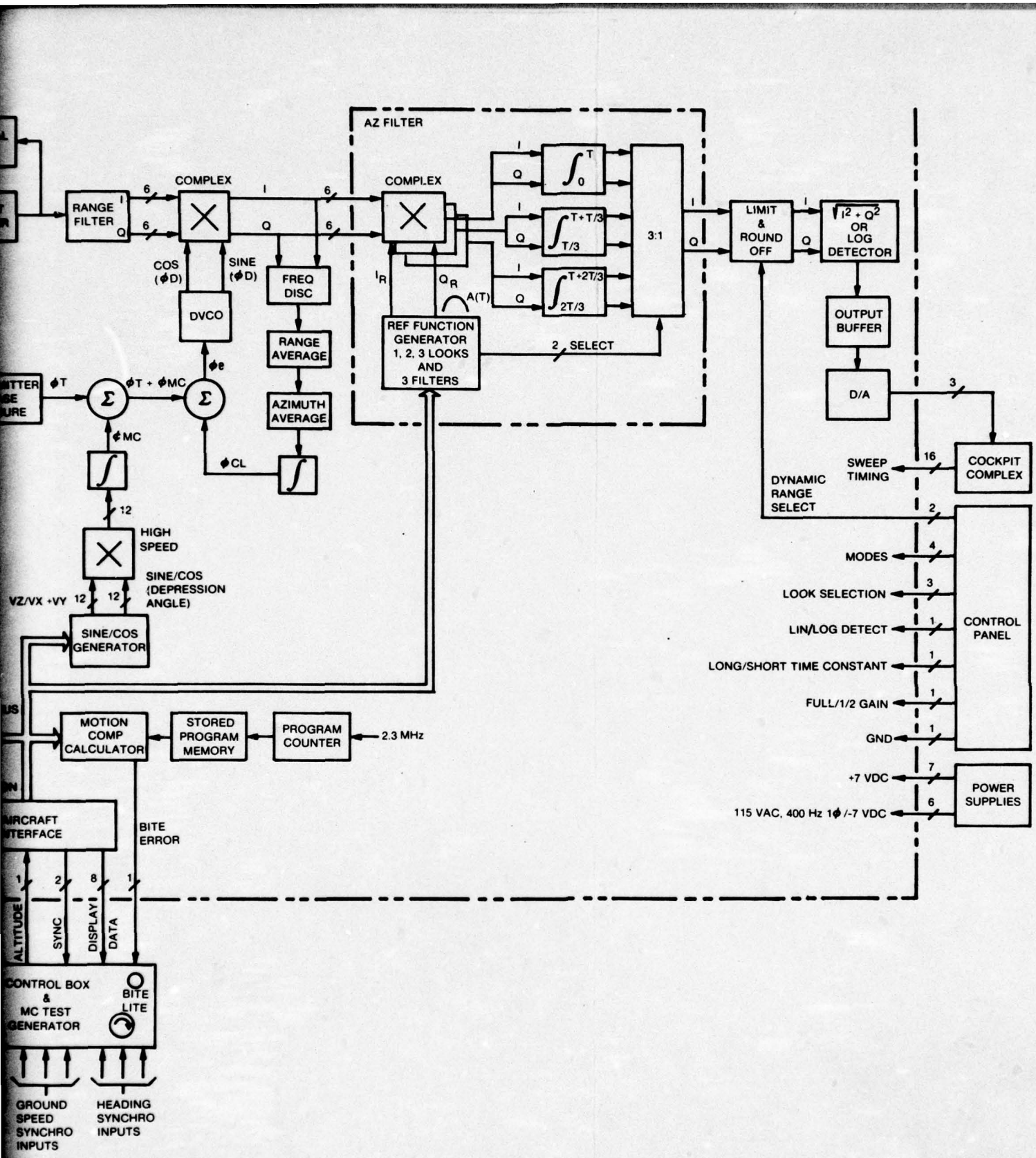

System Detailed Block Diagram

3.2.3.4 Complex Multiplier/DVCO

The signal data out of the range filter is then corrected in phase by the complex multiplier shown in figure 3-19. The total phase correction is then sum of ϕ_T (the transmitter phase correction discussed in paragraph 3.1.2), ϕ_{CL} (the clutter lock or doppler spectrum translation described in paragraph 3.1.1.3) and ϕ_{MC} (the motion compensation correction discussed in paragraph 3.1.1.3).

3.2.3.5 Transmitter Phase Correction

The transmitter phase correction is generated each pulse period from the sample of transmitter RF that is injected into the receive path. The receiver/transmitter stable local oscillator provides a phase reference for this sample. The difference phase thus generated represents the random phase of the transmitter, which is then subtracted from the subsequent echo phase to produce a signal coherent with the stable local oscillator. The phase measure circuit is completely digital and derives the phase information from the two amplitude samples from each pulse.

3.2.3.6 Clutter Lock

A clutter lock subsystem depicted in figure 3-19 corrects the data prior to the azimuth filters to account for any offset frequency of the clutter spectrum caused by the antenna beam not pointing in the zero doppler direction. For each of many range blocks, a digital frequency discriminator develops an error signal which is averaged in range and azimuth. The clutter-lock subsystem comprises anywhere from 1 to 64 independent loops, depending on the radar operating mode. Short range loops (closely spaced in range) are used at near range because of the rapidly changing depression angles; the blocks progressively get larger at longer ranges. The azimuth and range averaging is required to prevent the loops from being pulled off frequency by large discrete targets. An AGC circuit is incorporated within the clutter-lock loop to maintain a constant loop gain. However, this function is not shown on the block diagram. The averaged error signals are integrated and converted to a frequency to close the loop.

The clutter-lock subsystem was designed to function against return from terrain. The system was not expected to function with the lower return levels obtained from the ocean.

3.2.3.7 Motion Compensation

Synthetic aperture radar processing involves the synthesis of a long antenna by properly processing and combining the return signals from many successive pulses. The azimuth resolution and sidelobe structure of targets thus processed depends strongly on the linearity of the synthetic antenna. Since aircraft generally do not fly in straight lines, some form of electrical signal compensation for motion irregularities is required. This is the function of the motion compensation circuitry. The motion compensation system was designed to keep

the motion-induced degradation in resolution to 50% and loss in signal-to-noise ratio less than 1.5 dB for the expected aircraft pertubations.

Briefly, the system as shown in figure 3-19 consists of a sensor package (three orthogonal accelerometers, gyro, and signal conditioning circuits) located on the antenna to sense the aircraft (antenna) motions. The gyro is used to supply roll and pitch inputs so that the gravity component may be corrected for in the accelerometers. The corrected accelerometer outputs, along with other aircraft and manual inputs, are supplied to a calculator whose output is a frequency correction for each range block of the clutter lock subsystem. This output is applied to the radar return signals prior to the azimuth filter processing. The aircraft inputs consist of ground speed, drift angle, and heading. Altitude, latitude, and longitude are supplied to the calculator via the operators control panel.

3.2.3.8 Azimuth Filters

The corrected data is then processed by the azimuth filters, the heart of a synthetic aperture radar. The azimuth filters are convolution types similar to the range filter. Whereas the range filter operates on consecutive range bins, the azimuth filter operates in azimuth and, therefore, requires much more memory. The reference function chosen is the Fourier Transform of a -35 dB sidelobe Taylor weighted function. This function was chosen to match the azimuth sidelobes to the display dynamic range while minimizing azimuth resolution degradation. The number of sample points in the reference function is governed by the bandwidth of the filter required, which determines the azimuth resolution. The filter bandwidth is directly proportional to aircraft velocity and was typically 4.5 Hz for the C-47 aircraft. The reference functions were stored in Read-Only-Memories (ROM's). The reference function and filter output select varies, depending on operating modes; i.e., range swath width, range delay, aircraft velocity, number of looks, and whether over land or over water.

The azimuth filter function is comprised of 3072 filters, each of which has three parallel sections. The individual filters are of the non-recursive type which integrate a number of pulses and then dump. If the target doppler sweeps into the filter passband during the integration cycle, some pulses would be missed. By providing three sections which start the integration at different times, then a complete integration cycle will be achieved on one of the filters.

The 3072 azimuth filters are used to provide the multiple-look capability described in paragraph 3.1.1.4 as a function of the operator selection as shown in table 3-3. For example, in the 100 km range selection, one azimuth filter is assigned to each of 3072 range cells. But in 25 km, 3-look selection, 3 filters are assigned to each of 1024 range cells.

The center frequency of an azimuth filter is determined by its reference function. The reference function changes as a function of range and aircraft velocity to maintain a constant ground spacing between the filters.

Table 3-3. Multiple Look Selections

Range Switch (km)	No. Range Cells	Range Delay (km)	Multiple Look Selections
100	3072	0	1
50	1536	0	1
50	1536	20	1 or 2
50	1536	40	1 or 2
25	1024	0	1
25	1024	20	1, 2 or 3
25	1024	40	1, 2 or 3
25	1024	60	1, 2 or 3

3.2.3.9 Display Interface

The limit and round-off function, shown in figure 3-19, performs three functions to each channel, I and Q, separately:

a. Limits salient targets to a full scale value.

b. Rounds-off the output of the azimuth filter.

c. Provides a means of dynamic range selection.

Two detection modes are provided by the detector circuit:

a. A linear operation which is the magnitude of the vector combination of the real component I and the quadrature component Q.

b. A log-like operation where the low level signals are accentuated and the high level signals are compressed.

The output buffer formats the video data such that output is compatible with the AN/APS-94D film recorder. The output sampling rate is directly proportional to the aircraft velocity. An output is generated every 15 meters of aircraft travel. At an aircraft velocity of 178 knots, the output sampling rate is 6.25 Hz. The buffered video output is then converted to an analog signal which drives the grid of the display cathode-ray tube to intensity modulate it.

3.3 PREDICTED PERFORMANCE

3.3.1 Resolution

The best azimuth resolution theoretically possible using unfocussed synthetic array processing is given by[1]:

$$\Delta_t = \sqrt{\frac{\lambda R}{2}}$$

where

R = range to target

λ = transmitter wavelength = 3.2 cm

The Motorola design goal is:

$$\Delta a = \sqrt{\lambda R}$$

The difference between the two values represents the total value of the error budget which is apportioned to the various hardware elements. The two most important parameters are:

a. The phase stability of the corrected coherent-on-receive video.

b. The error in compensating for the motion of the aircraft.

The error budget for phase stability is 15° rms error as averaged over the array time of 0.25 seconds. The relationship of the errors in the motion compensation vertical gyro and accelerometers to system performance is not so easily stated. A complete characterization necessitates a dynamic, three-dimensional, six-degree-of-freedom statistical analysis. The Motorola analysis of the motion compensation function is contained as Appendix A.

Figure 3-20 shows the design goal resolution. The resolution of the 8-foot real aperture Oil Slick Detection Radar is also shown for reference.

3.3.2 Detection

The ranges at which the sea surface should produce sufficient signal-to-noise to be detected on the film display were calculated for both the synthetic aperture radar and the standard AN/APS-94D. These calculations are contained in Appendix B. The capability to detect surface oil on imagery cannot be fully described by this conventional radar range equation approach since the size and shape provide contextual cues to the image interpreter which are not readily analyzed. However, these calculations provide a useful frame of reference for comparing systems and evaluating test results.

[1] Radar Handbook, Merrit I. Skolnik, McGraw Hill, 1970, page 23-4

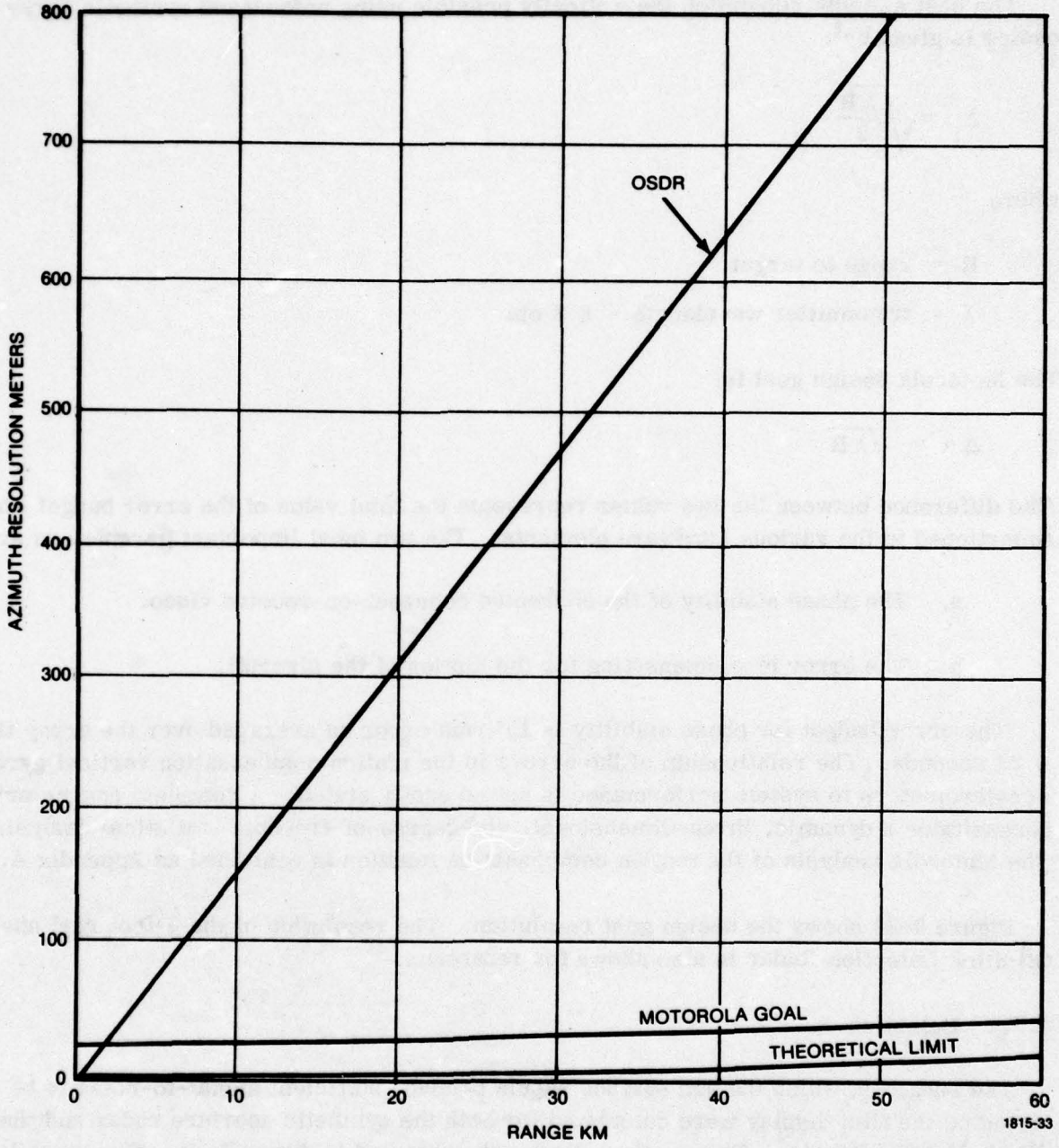

Figure 3-20. Predicted Azimuth Resolution

Calculations are also included in Appendix B for the performance of the two systems against point targets. The maximum range values appear both in Appendix B and in the tables of Section 5, which compare the test results with predictions.

3.4 BENCH TEST RESULTS

3.4.1 Processor

3.4.1.1 Test Setup

A digital chirp generator, followed by a D/A converter and low pass filter, was used to generate a test signal for the processor. This test signal included the following components:

a. Antenna beam pattern weighted chirp signal return from a point target.

b. 2.3 MHz offset.

c. Drift angle offset.

d. Constant clutter background.

Running this simulated target into the processor front end (A/D converter), and viewing the output on the modified APS-94 film recorder, we were able to measure resolution improvement and clutter lock operation.

Direct resolution comparisons were made possible by removing the azimuth filter and running jumper wires from the clutter lock multiplier to the detector card. This is a close approximation to the standard APS-94 radar.

Note that the test signal used was a fully coherent signal. Thus, no phase correction for transmitter non-coherence was required or used.

3.4.1.2 Resolution Comparison

Film runs indicated a spot size (AZIMUTH x RANGE) at 50 KM range of 1300' x 150' for APS-94 vs. 130 x 150' for COR. The clutter lock was disabled for this experiment.

3.4.1.2.1 Multiple Looks. Using a 50 KM target for an input signal, the display was adjusted such that all three looks converged at 50 KM. Resolution of multiple looks seemed to be slightly degraded from one look, approximately by a factor of 1.2. The enlarged imagery of figure 3-21 shows the relative image size.

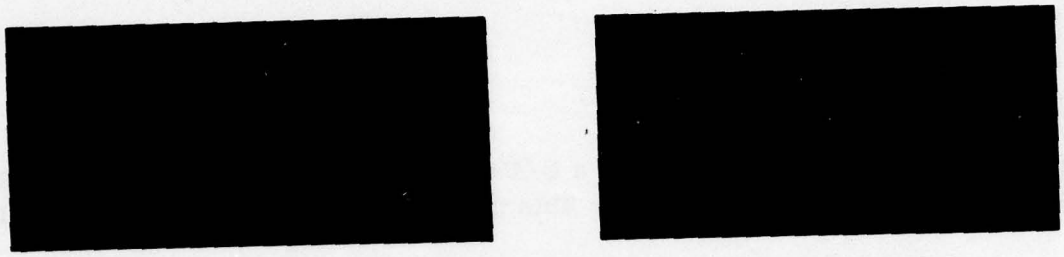

SIMULATED
APS-94D
POINT TARGETS
(50 KM)

SYNTHETIC APERATURE
POINT TARGETS
(3 LOOKS)
(50 KM)

Figure 3-21. Simulated Point Targets at 50 km

3.4.1.3 Clutter Lock

Operation of the clutter lock was unsatisfactory in that the loops would not lock within the required ±1/4 Hz accuracy to a small offset (< 10 Hz). The close-in (2 bin) loops locked within specification, but the further out loops seemed to be increasingly deviant as a function of range. At maximum range, the error was ±2 Hz.

For offsets greater than 10 Hz, lockup error seemed to be increasingly deviant as a function of frequency offset. An offset of 50 Hz produced ≃10 Hz error in the long range loops. However, sometimes the close-in loops would lock within specification to a large offset.

3.4.2 R/T Unit - Coherency Tests

3.4.2.1 Preliminary

A rooftop test was conducted in which a digital phase measurement circuit was used in conjunction with a D/A. The circuit measured the transmit phase and corrected the receive phase. Finally, the video (with corrected phase) was plotted as a function of time. Results show a 7.5° rms phase error. However, some of this may have been due to the unstable klystron source used in the experiment (the system stalo was not available at the time).

3.4.2.2 System Coherency

Another rooftop test was conducted in which the coherency was measured at two points in the processor:

a. Output of range filter using a D/A on either channel (I or Q).

b. Output of azimuth filter (after detection).

3.4.2.2.1 Coherency at Range Filter. Peak amplitude variations for a given point target measured on the order of 30% full scale. With this amplitude measured (on I or Q channel) as a deviation from zero, then

$$\sin \theta = 0.3$$

where θ is the peak phase deviation. Thus, $\theta = 17.5°$, yielding an rms error of 12.5°. This test included the amplitude variations inherent in the range filter. The range filter output is strongly dependent upon the phase of the incident target.

3.4.2.2.2 Coherency at Output Azimuth Filter. After detection, the output of the azimuth filter exhibits a much higher return for coherent video than non-coherent. For rooftop tests, only the filters centered at DC are examined, since there is no doppler spread to targets. Average video level output was about five times higher for phase corrected video than for non-corrected video.

4. AIRCRAFT INSTALLATION

4.1 ANTENNA INSTALLATION

The 8-foot vertically-polarized OSDR Antenna was used for the flight test program. The antenna was mounted under the wing of a C-47 as shown in figure 4-1. It was located several feet to the right of the aircraft center line, since the antenna looked only to the right and this made for an easier installation. The mount was designed and fabricated by the U.S. Army at Ft. Huachuca. The only modification to the antenna was to incorporate the motion sensor package shown in figure 4-2.

The installation was satisfactory for the test program. However, elevation pattern "banding" was noticeable out to a range of about 5 kilometers at normal operating altitudes. This was caused by reflections off the wing and engine nacelle of the aircraft which cause alternate reinforcement and cancellation of the radar return signal. The antenna location must be carefully chosen in an operational system.

4.2 INTERIOR INSTALLATION

Figure 4-3 shows the installation of all the radar components except for the antenna. The major criteria used for the cabin installation was to minimize the length of the waveguide run to the antenna, locating the signal processor close to the test equipment rack, and complying with the aircraft center-of-gravity restrictions. Figure 4-4 shows the signal processor with covers removed. No attempt was made to optimize the installation for an operational system, as this aircraft was to be used only as a test bed for the radar.

4.3 AIRCRAFT INTERFACES

The electrical interfaces with the aircraft consisted of those for prime power and an inertial navigator system (INS). All power inputs to the radar system were routed through a power distribution panel located at the top of the equipment rack as shown in figure 4-2. This was done to protect aircraft wiring, to be able to monitor power inputs, and to provide circuit breakers in one central location in case the system needed to be shut down quickly due to an emergency. The following prime power was required by the system:

28 VDC	Basic OSDR System
115 VAC, 400 Hz, 3-phase	Basic OSDR System
115 VAC, 400 Hz, 1-phase	COR Signal Processor
115 VAC, 60 Hz, 1-phase	Test Equipment

The INS was installed by the Army to provide aircraft inputs to the radar. The signals required by the radar were aircraft heading, drift angle, and ground speed. These interfaces were accommodated by Motorola with synchro servo loops and synchro-to-digital converters. Other aircraft flight parameters such as altitude and latitude were inserted into the system manually since they changed slowly during the radar missions.

Figure 4-1. Antenna Installation

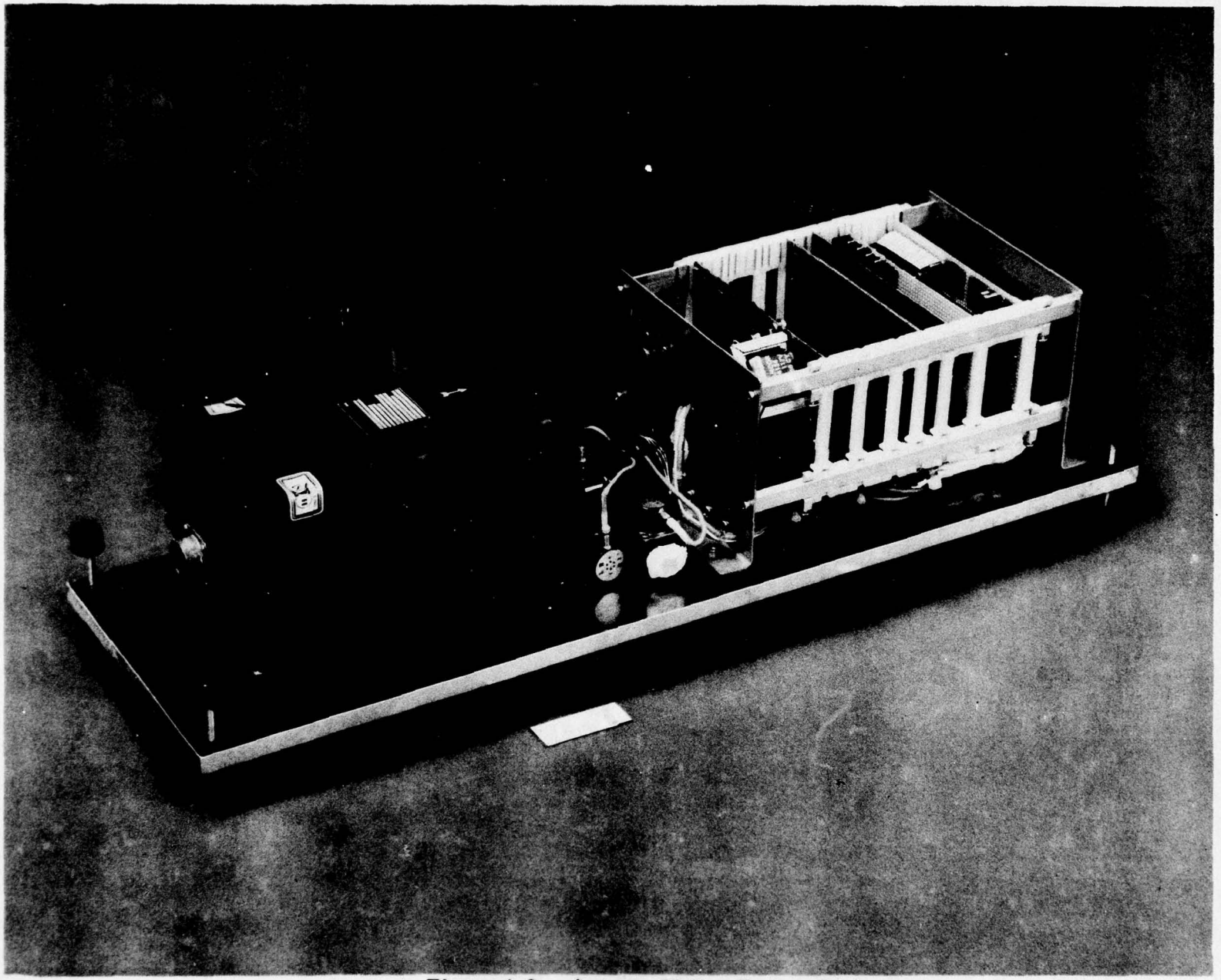

Figure 4-2. Antenna Motion Sensor Package

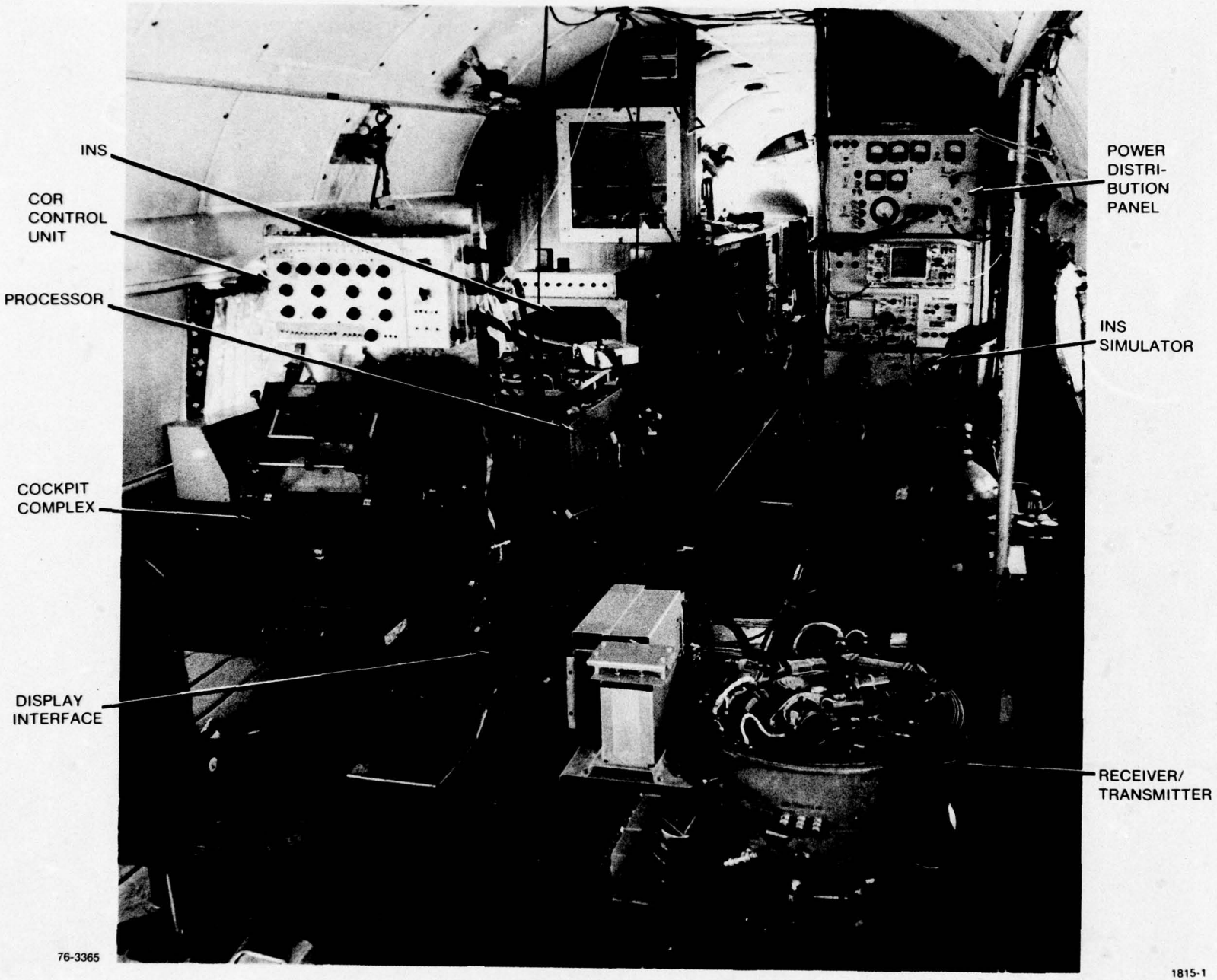

Figure 4-3. Interior Installation

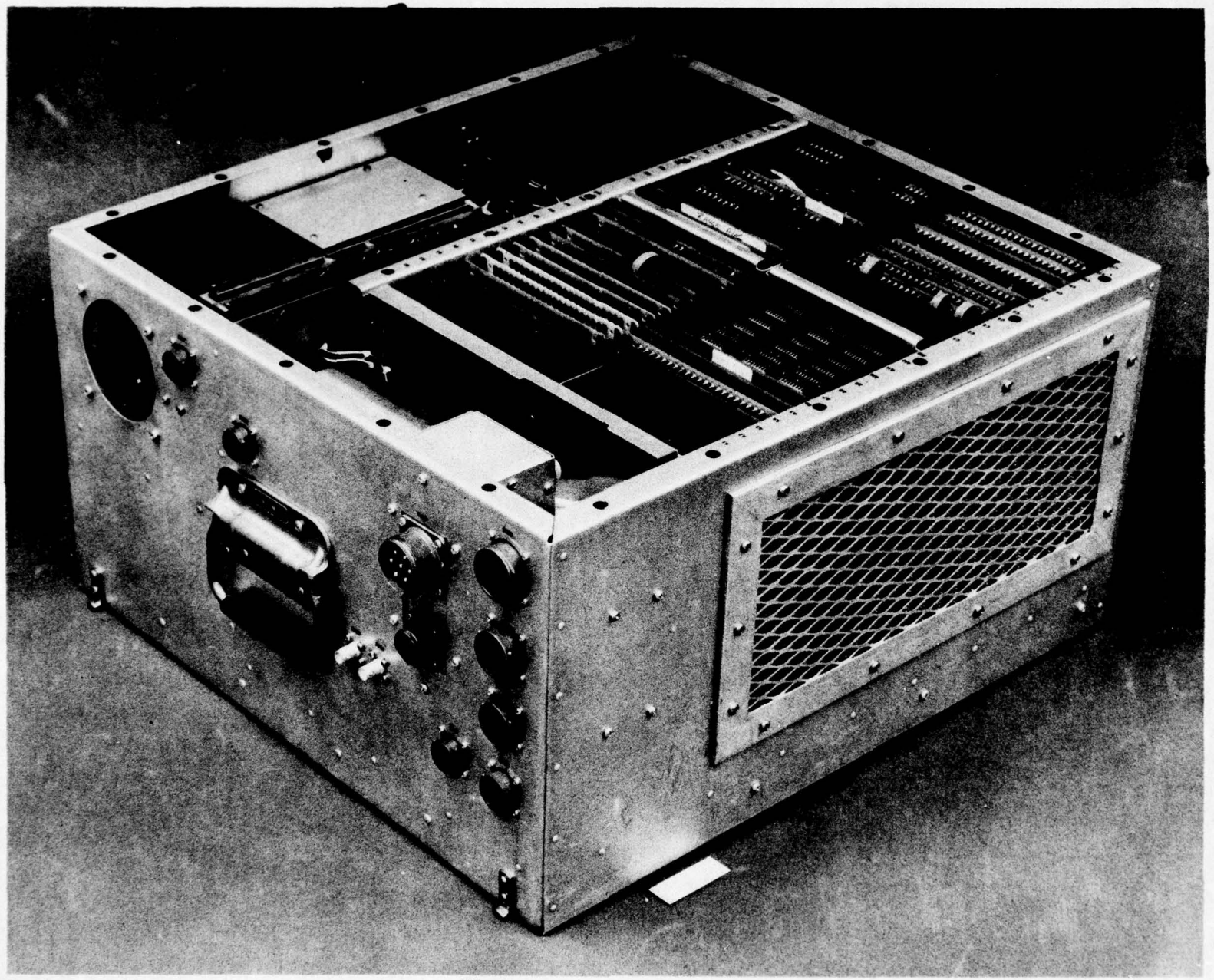

Figure 4-4. Signal Processor

5. FLIGHT TEST PROGRAM

The Army C-47 arrived at Phoenix on 15 March 1976 and the preliminary installation work was started. The antenna was installed on the aircraft and measurements made to allow fabrication of the waveguide run between the antenna and receiver/transmitter. The radar black boxes were fitted into the Army-fabricated racks to determine the rack modifications required. A flight was made on 18 March 1976 to demonstrate airworthiness of the antenna installation. From 18 March through 24 March 1976, flight safety certification and the radar installation were completed. The period of 25 March through 17 May 1976 was devoted to shake-down and equipment check-out.

Included in this period was one 3-day trip to Pt. Mugu to provide preliminary information on the radar's ability to detect sea state and ocean surface targets, both moving and fixed. Formal ocean mapping missions were conducted the week ending 21 May 1976. Table 5-1 tabulates all missions flown during the flight test program. Appendix C contains the Flight Test Plan, Appendix D contains the Flight Data Sheets, and Appendix E contains sample imagery and photographs.

5.1 LAND MAPPING RESULTS

The land mapping phase of the flight test program consisted of shake-down flights for check-out of the various functions and modes of the system. Proper superposition of multiple-look synthetic array maps and resolution improvement by a factor of ten relative to the OSDR were demonstrated. Numerous aircraft INS and radar/INS interface problems described in detail below prevented collection of valid quantitative aircraft motion data. However, the effect upon the imagery of aircraft motions described qualitatively (e.g., "calm", "moderate turbulence") is presented.

5.1.1 Multiple-Look Imagery

The multiple-look feature of the COR System performed as expected in over-land operation. The imagery shows the independent looks could be successfully overlayed on the film to form a single sharp radar map. The expected reduction in salt-and-pepper appearance of the SAR imagery was also very apparent when compared to the single-look imagery. Figure E-2 (Appendix E) shows this effect on a single photo. The left hand inch was made with a single look while the remainder is three look. The range is 20 km at the bottom and 45 km at the top. In addition to the overall smoother texture of the multiple look imagery, note the additional terrain features visible with the multiple looks. The road that crosses the portion of the map where the mode was switched cannot be detected in the single look mode. Figure E-3 (Appendix E) shows an example of some longer range three look imagery (40 to 65 km).

5.1.2 Resolution

One of the program objectives was to measure the system's resolution on the Ft. Huachuca resolution spoke. The spoke is an array of wooden platforms at varying spacing

Table 5-1. Flight Schedule

Date	Sortie No.	Mission	Flight Hours
18 March 1976	1	Airworthiness check-out flight.	2.3
25 March 1976	2	To Ft. Huachuca to install INS.	2.3
30 March 1976	3	Local check-out flight.	2.5
1 April 1976	4	Local check-out flight.	2.5
10 April 1976	5	Local check-out flight.	2.2
21 April 1976	6	Local check-out flight.	2.0
22 April 1976	7	Local check-out flight.	2.0
26 April 1976	8	Ferry to Pt. Mugu.	3.3
27 April 1976	9	Ocean mapping shake-down flight.	2.8
28 April 1976	10	Ferry to Phoenix	2.8
12 May 1976	11	Local check-out flight.	2.0
13 May 1976	12	To Ft. Huachuca to repair INS.	2.0
14 May 1976	13	Ferry to Phoenix.	2.0
17 May 1976	14	Local check-out flight.	2.0
18 May 1976	15	Ferry to Pt. Mugu.	4.0
19 May 1976	16	Ocean mapping.	2.7
21 May 1976	17	Ocean mapping and ferry to Phoenix	7.2
26 May 1976	18	Local mapping flight.	2.9
27 May 1976	19	Ground mapping at Ft. Huachuca.	3.8

upon which corner reflectors are set up to check resolution and detectability. A series of radar passes were flown against the range on 27 May 1976. No results were obtained. Several problems were encountered on the mission that contributed to the lack of results. The INS had failed and the pilot was having trouble flying the specified course. A major failure was experienced in the motion compensation circuitry causing this function to be non-operative. Furthermore, at the ranges that the flights were required to be flown, the flight course was over mountains which resulted in extremely turbulent flight conditions. Considering the short time left in the program, the INS and system problems, and the fact that the resolution could be easily measured using point targets from other flights, it was decided to abandon any further attempts to map the resolution range.

The films were examined for point targets, such as power poles, at long range and the 6 dB azimuth dimension was measured using a magnifying glass with a calibrated scale. Sufficient targets were measured to give a representative measure of the synthetic aperture beamwidth. Figure 5-1 shows a graph of measured azimuth beamwidth of the SAR. The real aperture beamwidth and the Motorola design goal, $\sqrt{\lambda R}$, are also included for comparison purposes.

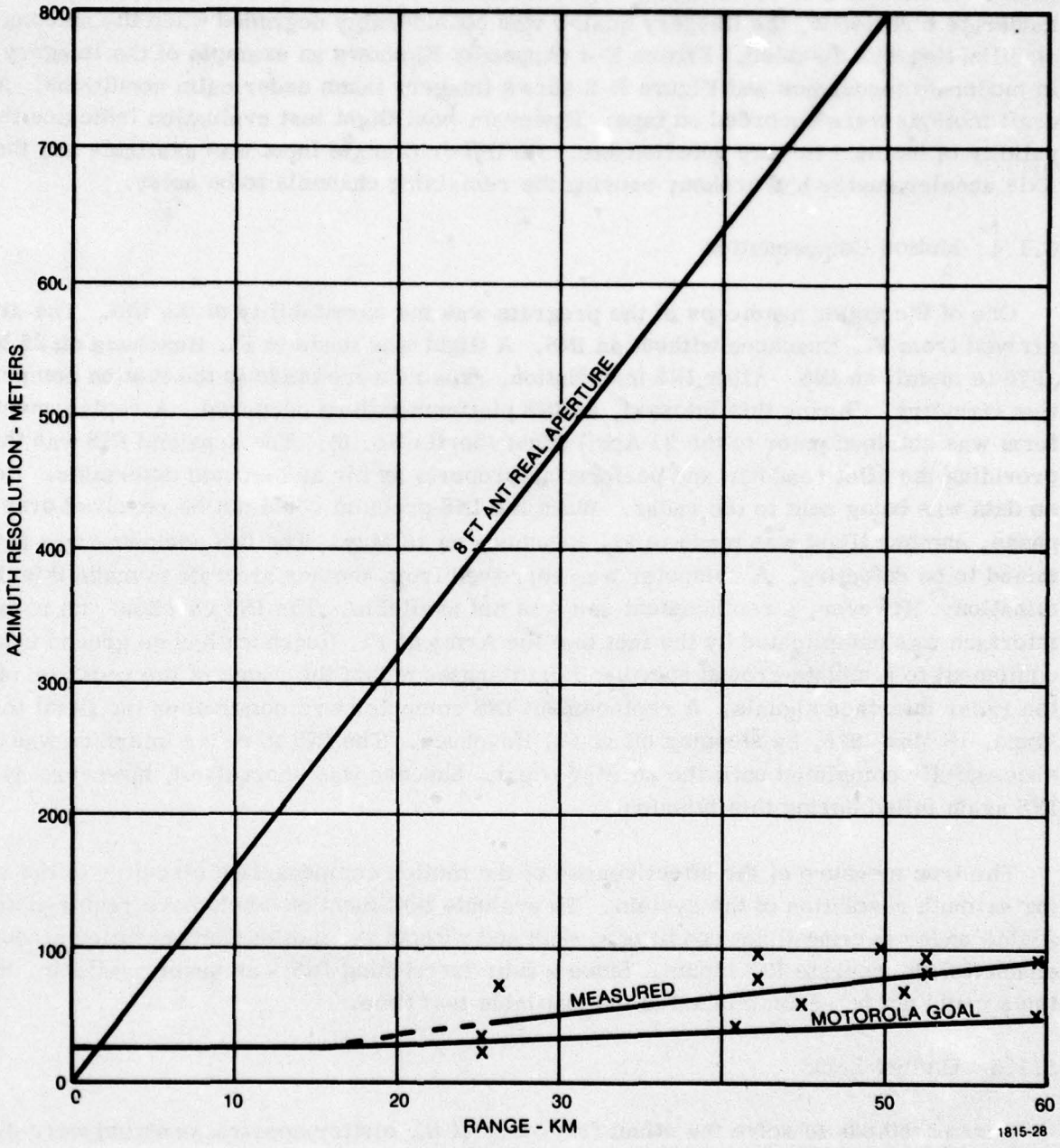

Figure 5-1. Azimuth Resolution

5.1.3 Antenna Yaw Compensation

To provide some insight into the need for a yaw stabilized antenna, several radar runs were made with the yaw servo disabled. The results were dependent on the amount of turbulence. In smooth air, the imagery degradation due to aircraft yaw was undetectable. With moderate turbulence, the imagery quality was considerably degraded when the antenna yaw stabilization was disabled. Figure E-4 (Appendix E) shows an example of the imagery taken in moderate turbulence and Figure E-2 shows imagery taken under calm conditions. Aircraft motions were recorded on tape. However, post flight test evaluation indicates that the validity of the data is very questionable. No INS drift angle input was available and the Z-Axis accelerometer had broken, causing the remaining channels to be noisy.

5.1.4 Motion Compensation

One of the major handicaps of the program was the unreliability of the INS. The aircraft arrived from Ft. Huachuca without an INS. A flight was made to Ft. Huachuca on 25 March 1976 to install an INS. After INS installation, repairs were made to the motion compensation circuitry. During this interval, an INS platform failure occurred. A replacement platform was obtained prior to the 21 April flight (Sortie No. 6). The repaired INS was then providing the pilot readouts and performing properly as far as he could determine. However, no data was being sent to the radar. When the INS problem could not be resolved over the phone, another flight was made to Ft. Huachuca on 13 May. The INS computer was determined to be defective. A computer was borrowed from another aircraft to make this determination. However, a replacement unit was not available. The INS checkout and radar interface was complicated by the fact that the Army at Ft. Huachuca has no ground support equipment to simulate ground speed and drift angles within the range of the radar or to test the radar interface signals. A replacement INS computer was obtained on the flight to Pt. Mugu, 18 May 1976, by stopping off at Ft. Huachuca. The INS to radar interface was not successfully completed until the 26 May flight. Success was short lived, however, as the INS again failed during this mission.

The true measure of the effectiveness of the motion compensation circuitry is the resulting azimuth resolution of the system. To evaluate this function would have required several flights under varying flight conditions, with and without the motion compensation circuitry enabled with accurate INS inputs. Since a fully functioning INS was never available, these tests could not be accomplished in the available test time.

5.1.5 Clutter Lock

Three methods to solve the offset frequency of the clutter spectral centroid were evaluated during the flight test program in the overland missions. The three methods used were: (1) actual measurement of the clutter spectrum return and compensating the azimuth filter center frequency through a feedback loop, (2) calculating the frequency from drift angle and ground speed inputs, and (3) manual tracking.

The automatic clutter lock circuits, intended to measure and correct the clutter spectral centroid, never functioned entirely correctly. A component failure in the discriminator prevented the clutter lock loops from achieving the required ±375 Hz pull-in range. Bench tests prior to flight testing had demonstrated the required pull-in range. Tests during the flight test program demonstrated only ±50 Hz with test signals. After spending considerable time trying to isolate the faulty component, it was decided that reasonable performance could be achieved with the limited pull-in range since the calculated clutter lock should correct the spectral centroid to within this range. Once acquired, the automatic system would maintain lock as shown in figure E-1 (Appendix E) until thrown out of lock by aircraft turbulence or when a large mountain shadow (loss of signal return) was encountered. Two causes of losing lock in turbulence are the lack of motion compensation or an inadequate antenna yaw servo. The automatic clutter lock was only intended to correct for the long term doppler correction. The motion compensation and antenna yaw servo were designed to compensate for the dynamic effects. Lack of drift angle and ground speed inputs from the INS prevented any further determination of this clutter lock problem.

The calculated clutter lock (using the INS information) could not be evaluated due to the INS problem described in paragraph 5.1.4. An attempt was made to evaluate this technique by supplying the drift angle and ground speed inputs to the radar manually. A simulator was built to supply these inputs to the radar. Drift angle and ground speed information was obtained from the pilot (as read from the INS readouts) and these values were set in manually. The doppler correction with these inputs would be typically within or near the physical beam. Operation with manual inputs was very touchy due to the high sensitivity to drift angle. The required doppler correction changes approximately 100 Hz per degree of drift angle at the nominal C-47 velocity. Since this is large compared to the 60 Hz doppler spread across the beam, it was very difficult to hold the synthetic azimuth filters within the real aperture.

The manual clutter lock operation was incorporated in case the other two approaches failed to function properly. This involved setting a fixed frequency offset into the clutter lock multiplier very similar to the calculated clutter lock. The INS simulator, when used to manually set the clutter lock, had a sensitivity of approximately 3000 Hz per turn of the drift angle and was too sensitive. The manual clutter lock sensitivity was 750 Hz per 10 turns. With this vernier control, and by monitoring the clutter lock discriminator output on an oscilloscope, the operator could perform this function.

5.2 OCEAN MAPPING

The ocean mapping of the flight test program was conducted during the week ending 21 May 1976. All flights were conducted out of Pt. Mugu, California. Three flights were planned to hopefully obtain various sea states. Two were conducted in the local area and one further up the coast at Morro Bay. An Army Mohawk from Ft. Huachuca, equipped with a standard AN/APS-94D, was included in the tests to obtain comparative imagery between the two systems. Participants in the tests were the U.S. Coast Guard, U.S. Army, Naval Research Laboratory (NRL), and the Geography Department of the University of California

at Santa Barbara. The U.S. Coast Guard provided all of the required coordination between the various participants and surface vessels. NRL was charged with the task of generating the synthetic oil slicks using oleyl alcohol. The University of California was responsible for providing the "ground truth" data for the tests.

The controlled vessels used for the flight test program were the U.S. Coast Guard cutters Pt. Judith, Cape Hedge, and a 41-foot utility boat from Channel Islands Coast Guard Station. A radar reflector with a radar cross section of five square meters was employed on two missions with each system. Four synthetic oil slicks were created for the tests. All other targets imaged were targets of opportunity.

The two radar-equipped aircraft flew in a box pattern around the target area. The AN/APS-94D was tuned to 9100 MHz and the COR to 9315 MHz to avoid interference and were to be over the target area as close to the same time as possible. All C-47 missions were flown at 5,500 feet and the Mohawk at 6,500 feet. During this time, the University of California personnel were flying over the target area in a small civilian aircraft while continuously identifying and photographing as many targets in the area as possible. Communications were maintained between the three aircraft and the main surface vessel.

Only on the first day, 19 May 1976, could all the participants carry out their scheduled missions. The C-47 developed engine problems the second day and the COR system tests had to be cancelled for that day. These tests were conducted on the third day. However, ground truth was not available for this day as the team was at Morro Bay preparing the that day's tests. The Army Mohawk missed the third day's tests as it had to return to Ft. Huachuca to satisfy other commitments.

5.2.1 Oil Slick Detection

Thin layers of oil on the surface of the ocean have the effect of damping the small waves caused by the wind. The radar can detect the presence of the oil due to this wave damping effect, which reduces the radar backscattering return from the ocean. The advantage of a SLAR system comes from the fact that it produces a permanent radar map in which even small differences in signal return can be recognized as oil by its distinctive pattern. Detection requires sufficient radar sensitivity and surface winds such that the ocean surface clutter can be seen on the radar map and also that the oil slick size must be large compared to the radar's resolution.

To evaluate the capability of the SAR to detect oil slicks, four synthetic slicks were created during the flight test program. The synthetic slicks are created by dumping small amounts of Oleyl alcohol into the ocean. Oleyl alcohol has the same effect on the ocean surface wave structure as does oil. Two small synthetic slicks were simultaneously created off Santa Barbara on 19 May 1976. Each slick contained 300 grams of Oleyl alcohol. The slicks were between 25 to 100 feet apart when created and were left to spread. Unfortunately, due to the calm seas, the alcohol did not spread as much as was hoped for. After 40 minutes, the two slicks had merged and the size was estimated to be 80 by 120 feet,

and did not significantly spread further. A photograph of these slicks is shown in Figure E-16 (Appendix E). Since this is about the size of the radar resolution cell, they were not detected by either system.

A third synthetic slick was generated on the same day by dispensing the material into the wake of a Coast Guard cutter. A total of 8.1 liters of Oleyl alcohol was dispensed at a linear concentration of 1.94 ml/meter, thus, creating a strip 2 1/4 mile long by 300 feet wide. A photograph of this slick is shown in Figures E-18 and E-19. This slick was detected by the COR to a range of about 25 km and by the AN/APS-94D to a range of 18 km. The sea state consisted of swells to 3 feet, choppy sea with occasional white caps, and surface winds of 6 to 10 Kts.

A fourth slick was created at Morro Bay on 21 May 1976. A total of 4.8 liters of Oleyl alcohol was dispensed at a linear concentration of 1.18 ml/meter. The slick was again 2 1/4 miles long. The sea was smooth but had about 50 percent coverage by capillary ripples. Swells were one foot high from the West, and the surface winds were from the Southwest at 4 knots. Due to the lower wind velocity and sea state, the COR could detect the slick only at a range of approximately 9 km. In addition to the synthetic slicks detected during the two missions, several natural seeps from the oil towers off Santa Barbara were detected.

The sea states for the flight tests were estimated by ground truth to be representative of low sea state two (S.S.2) for the 19 May tests and sea state zero (S.S.0) for 21 May. For the S.S.2 condition, the backscattering coefficient is between -42 and -36 dB[1] for the vertically polarized COR system and -51 to -43 dB for the horizontally polarized AN/APS-94D system. The 7 to 9 dB increase in backscattering coefficient for vertical polarization could not be demonstrated by the tests due to the different processing techniques and antenna sizes of the two systems. One result that could be observed by the tests was the greater dependence of look direction relative to the wind direction for the AN/APS-94D. Table 5-2 contains a summary of the nine runs of the 19 May mission. The columns headed "Radar Sea Return" list the relative magnitude of sea clutter return for each system. Runs 2, 3, 6, and 7 show the highest sea return with the AN/APS-94D while looking upwind. The other runs were made while looking downwind and show much lower sea clutter return. The vertically polarized COR did not show this effect. Figures E-9 and E-10 of Appendix E show upwind imagery and Figures E-11 and E-12 show downwind imagery.

Table 5-3 contains a summary of the synthetic oil slick detections by the COR and AN/APS-94D. Theoretical range calculations are shown in Appendix B. Table 5-4 shows a summary of all oil slick detections. The small synthetic slicks are not included in this table since they were too small to be detected by either system.

---

[1] Fred E. Nathanson, Radar Design Principles, 1969.

5.2.2 Boat Detection

A very limited amount of detection data is available to determine the maximum ranges for various size boats and ships. No detection data is available under high sea states. The mission to detect boats at longer ranges was only flown by the AN/APS-94D, as the C-47 developed mechanical problems that day. The mission was flown the next day with the COR. However, ground truth was not available as the crew that provided this data was deployed at the Morro Bay test area for that day's tests.

Table 5-2 provides a summary of the controlled target results for the 19 May mission (Sortie No. 16) where the COR and AN/APS-94D were flown under identical conditions. The Coast Guard cutter was detected in most runs due to its relatively large size and the short range. The $5m^2$ radar deflector was generally detected for the three runs that it was deployed. The oil slick was started prior to run five but was not detected on that run. A probable explanation for not detecting it even though the cutter had been dispensing the Oleyl alcohol for a mile is that the alcohol had not had sufficient time to surface and spread.

Longer range detection data against known size targets were obtained on the 20 May 1976 AN/APS-94D flight and the 21 May 1976 COR flight. A 41-foot utility boat and the $5m^2$ radar reflector were imaged at different ranges. Table 5-5 provides a summary of the results of these two missions. Calculations of maximum ranges are shown in Appendix B. All of the radar runs for this mission were made in the COR's overwater mode.

Table 5-2. Controlled Target Detections, 19 May 1976

	COR					AN/APS-94D			
	Radar Mode	CG Cutter	$5M^2$ Target	Long Oil Slick	Radar Sea Return	CG Cutter	$5m^2$ Target	Oil Slick	Radar Sea Return
Run #1 351° Heading	Water	Yes	Yes (16 km)	N/A	Good	Yes	Yes (17 km)	N/A	Very Low
Run #2 093° Heading	Water	Yes	Yes (16 km)	N/A	Fair	Yes	Yes (17 km)	N/A	Good
Run #3 185° Heading	Land 1 Look	No	No	N/A	Good	Yes	Yes (20 km)	N/A	Good
Run #4 269° Heading	Land 1 Look	Yes	N/A	N/A	Good	Yes	N/A	N/A	Very Low
Run #5 351° Heading	Water	Yes	N/A	N/A	Good	Yes	N/A	No	Very Low
Run #6 093° Heading	Water	Yes	N/A	Yes	Fair	Yes	N/A	No	Good
Run #7 178° Heading	Land 1 Look	Yes	N/A	Yes	Good	Yes	N/A	Yes	Good
Run #8 270° Heading	Land 1 Look	N/A	N/A	Yes	Good	Yes	N/A	Yes (Weak)	Low
Run #9 351° Heading	Land 3 Look	N/A	N/A	Yes	Good	N/A	N/A	No	Low

Notes: 1. Surface conditions were 3 ft swells from 270° and 10 kt winds from 220°.

2. N/A signifies target was not in the area when the run was flown.

3. Sea State classifications indicate relative magnitude of sea clutter return.

Table 5-3. Synthetic Oil Slick Detection Summary

Location Date	Size	Sea State	Radar Look Direction	Radar Mode	COR Results	Cal. Max. Range to Det Sea	APS-94D Results	Cal. Max. Range to Det Sea
Santa Barbara 5/19 (SORTIE #16)	80X120'	3' swells from 270° 10 kt wind from 220° (552)	220°	Land & over water	Not detected (not large enough)	18	Not detected (not large enough)	30
Santa Barbara 5/19 (SORTIE #16)	2 1/4 mi x 300 ft.	3' swells from 270° 10 kt wind from 220° (552)	81°	Over water	Run #5 Not detected (Slick not developed)	18	Run #5 Not detected (Slick not developed)	30
			183°	Over water	Run #6 Barely detected at 15 Km.	18	Run #6 Not detected at 15 Km.	30
			268°	Land 1 look	Run #7 Detected at≈18 Km.	25	Run #7 detected at≈18 Km.	30
			0°	Land 1 look	Run #8 Detected at≈15 Km.	25	Run #8 det. at≈15 Km.	30
			81°	Land 3 look	Run #9 Detected at≈25 Km.	29	Run #9 Not detected at 25 Km.	30
Morro Bay 5/21 (SORTIE #17)	2 1/4 mi X 500 ft.	Smooth with 1 ft. swells 4 kt. winds (SSO)	265°	Over water	Run #17 Detected at≈9 Km.	14	Not flown.	21

Table 5-4. Surface Slick (Natural & Synthetic) Detection Summary

DATE	SYSTEM	TOTAL POSSIBLE[A]	NUMBER DETECTED	%
5/19	AN/APS-94D	31	11	35
5/19	COR	31	29	94
5/21	COR	2	1	50

A. Natural Seeps: 1) 3.9 square miles, 2) 4.4 square miles, 3) 6 square miles, 4) long elongated slick

Synthetic Slicks: 2.25 miles by 300 feet

Table 5-5. Controlled Target Detections, 20-21 May 1976

	COR		AN/APS-94D	
	41' Utility Boat	$5m^2$	41' Utility Boat	$5m^2$
Calculated Maximum	56 Km	33 Km	94 Km	56 Km
Run #1	10 Km	10 Km	3 Km	3 Km
Run #3	19 Km	19 Km	26 Km	26 Km
Run #5	30 Km	Not detected at 30 Km	Not detected at 50 Km	Not detected at 50 Km
Run #7	50 Km (very weak)	Not detected at 50 Km	57 Km	Not detected at 50 Km

Tables 5-6 through 5-8 summarize some of the detection data against man made targets of opportunity. This data was taken from the report "Summary Evaluation of the Offshore Target Detection Capabilities of APS-94D and COR Radar Systems" prepared by the University of California, Santa Barbara. Very little data was taken at ranges greater than 25 km.

Table 5-6. Buoy, Mooring, and Float Detections

RANGE	AN/APS-94D	COR
0 to 5 Km		6 of 6
5 to 10 Km	8 of 8	39 of 40
10 to 15 Km	12 of 12	39 of 48
15 to 20 Km	15 of 15	37 of 41
20 to 25 Km	15 of 15	14 of 14
25 to 30 Km	2 of 4	1 of 1
30 to 35 Km	6 of 6	
35 to 40 Km	5 of 5	
40 to 45 Km	6 of 6	
45 to 50 Km	6 of 6	
50 to 55 Km	3 of 3	
55 to 60 Km	0 of 1	
60 to 65 Km	1 of 1	

NOTE: Total detections between the two systems does not agree due to different missions flown.

Table 5-7. Vessel Detections, COR

RANGE	FISHING BOATS	BARGES	SAIL BOATS	CREW BOATS	TUGS	CUTTERS	CABIN CRUISER	MISC.
0 to 5 Km			1 of 1	1 of 1	1 of 1			
5 to 10 Km	3 of 3			1 of 1	1 of 1		1 of 2	
10 to 15 Km	4 of 4	2 of 2	4 of 6	5 of 5	2 of 3	5 of 5	6 of 7	
15 to 20 Km	4 of 4	5 of 5		7 of 9	6 of 7	6 of 7	4 of 5	
20 to 25 Km			0 of 1	1 of 1	1 of 1	1 of 1	2 of 3	
25 to 30 Km								
30 to 35 Km						1 of 1		
35 to 40 Km								
40 to 45 Km								2 of 2

Table 5-8. Vessel Detections, AN/APS-94D

RANGE	FISHING BOATS	BARGES	SAIL BOATS	CREW BOATS[1]	TUGS	CUTTERS	CABIN CRUISER	MISC.
0 to 5 Km								
5 to 10 Km			1 of 1	3 of 4	2 of 2			
10 to 15 Km				3 of 3	2 of 2	3 of 3	5 of 5	1 of 1
15 to 20 Km	1 of 1	2 of 2	7 of 7	6 of 6	5 of 5	4 of 4	2 of 2	1 of 1
20 to 25 Km	1 of 1		5 of 5	6 of 6	5 of 5	2 of 2	3 of 3	1 of 1
25 to 30 Km	1 of 1					1 of 1		1 of 1
30 to 35 Km	1 of 1			1 of 2				
35 to 40 Km				1 of 2		1 of 1		1 of 1
40 to 45 Km		2 of 2		1 of 2				1 of 1
45 to 50 Km								
50 to 55 Km				1 of 1				
55 to 60 Km	3 of 3			2 of 3				1 of 1
60 to 65 Km								
65 to 70 Km				1 of 1				1 of 1

(1) The non-detection of Crew Boats was caused by two boats anchored together and therefore unresolvable by the radar.

6. CONCLUSIONS

In this section, the flight test program results discussed in Section 5 will be compared with the program objectives listed in Section 2.

The primary objective was to examine the concept of synthetic aperture radar processing as applied to the problem of detecting and mapping Coast Guard targets on the surface of the ocean at various sea states and aircraft velocities. During the test period, only sea states zero, one and two were available, and the C-47 test bed aircraft is capable of only a limited range of velocities. With these qualifications, the test program demonstrated that a synthetic aperture radar can be designed which is usable for Coast Guard over-water missions.

Two radar characteristics were demonstrated individually:

a. Detection of moving surface objects in "over-water" mode.

b. Proper superimposition of multiple-look synthetic maps, resulting in imagery with sharp definition and a resolution 10 times better than OSDR in "over land" mode.

The method of combining these two characteristics into a single mode is understood and is described in Paragraphs 3.1.1.4, 3.1.1.5 and 3.1.1.6.

6.1 RESOLUTION IMPROVEMENT

As discussed in detail in Section 5.1, the tests against the resolution range at Ft. Huachuca yielded no data. However, the spot size of 15 power pole images in the Phoenix area at ranges of 25 to 60 km were measured. The resolution measured by this method was 10 times better than OSDR but poorer than the Motorola design goal by a factor of two. The 30 dB sidelobes of the azimuth filter were not sufficient to keep large vessels from "blooming" on the display. Azimuth filter sidelobes of 40-50 dB are feasible and would provide rejection equivalent to the OSDR real aperture round trip antenna pattern.

6.2 DETERMINE BEST APPROACH TO MOTION COMPENSATION AND CLUTTER LOCK

Due to a combination of INS and radar failures described in detail in Paragraph 5.1.4, a demonstration of positioning the received spectrum automatically based on INS inputs was not accomplished. Through the addition of a vernier control, the operator was able to position the spectrum manually, thereby permitting synthetic aperture imagery to be generated and other test objectives to be fulfilled.

6.3 MAXIMUM DETECTION RANGES FOR BOATS AND SHIPS

These measurements were performed and are tabulated in Paragraph 5.1. The 5-square meter target was detected at approximately 20 km. The 41-foot utility boat was detected between 30 and 50 km. It should be remembered that the over-water mode tested had a 6 dB loss, as explained in Paragraph 3.1.1.5, which would not be present in an operational system. Elimination of this loss should increase the detection range by 40 percent.

6.4 MAXIMUM DETECTION RANGE OF OIL SLICKS

Maximum detection range of the 2.25 miles by 300-foot Oleyl alcohol slick by the COR was 25 km and by the AN/APS-94D it was 15 km, under 10 knot wind conditions. The COR also detected a 2.25 mile by 500-foot slick at 9 km with a 4 knot wind. The detailed test results are presented in Paragraph 5.2.

6.5 EVALUATE THE EFFECTS OF AN UNSTABILIZED ANTENNA

Tests were conducted using the COR system with and without yaw stabilization. The imagery is shown in Figure E-4 of Appendix E. It is concluded that yaw stabilization must be provided for an 8-foot antenna.

6.6 OBTAIN COMPARISON IMAGERY BETWEEN AN/APS-94D AND THE SYNTHETIC APERTURE RADAR

Comparative imagery was obtained and detection performance is compared in detail in Paragraph 5.2. As shown in Table 5-3, the COR radar detected synthetic oil slicks at longer ranges than the AN/APS-94D. This must be credited to the higher sea return provided by vertical polarization although the unfamiliarity of the Army AN/APS-94D operator with this type of mission was a factor. The AN/APS-94D detected the 5-square meter test target and vessels at longer ranges. The overall appearance of the AN/APS-94D imagery was better, due largely to multiple printing which occurs in the COR feasibility test over-water mode as explained in Paragraph 3.1.1.5. Multiple-look over-land mode imagery shown in Figure E-2 and E-3 of Appendix E approaches the quality of the AN/APS-94D and is representative of the operational over-water mode described in Paragraph 3.1.1.6.

6.7 EXPLAIN ANY IMAGE DEGRADATION

Any major degradation in the imagery, such as the multiple printing in the over-water mode, has been completely explained and changes to eliminate this characteristic in any future radar are well understood. The detailed explanations and samples of imagery are presented in Section 5 and Appendix E, respectively.

6.8 FEASIBILITY OF USING AN UNSTABILIZED 4-FOOT ANTENNA

The tradeoffs were investigated and are presented in Paragraph 3.1.1.7. The most significant performance tradeoff is that either transmitter power must be increased by four, or approximately 30 percent less detection range must be accepted with the smaller aperture. The conclusion is that yaw stabilization should be included as a part of the radar until test data can be taken on the specific aircraft type which will carry the radar, although the Motorola analysis offers some hope that unstabilized operation might be possible.

7. RECOMMENDATIONS

Any recommendations for future radar actions must necessarily include issues outside the tasks addressed by this test program. The key consideration is the selection of the aircraft which will carry the radar. The primary alternatives appear to be, in descending order of preference:

a. Make a serious effort to install a 16-foot vertically-polarized antenna on the selected aircraft. This would permit a real aperture approach which retains the simplicity and reliability of the OSDR, but provides increased detection range and improves resolution by a factor of two.

b. Install an 8-foot vertically polarized antenna. The radar could be modular with an optional synthetic array processor. Use of a 200KW transmitter, such as the one currently being developed as a part of the APS-94 product improvement program, provides a real aperture mode similar to the OSDR, but with increased detection range. The synthetic aperture mode could be installed on those selected missions requiring higher resolution. (For example, the various ice mapping programs are currently using the 16-foot antennas and might not feel that they could use lesser resolution.)

APPENDIX A

MOTION COMPENSATION FOR COR

Technical Memorandum #M-152

12 May 1975

Prepared by:

E. J. Carlson
Systems Analysis Group

TABLE OF CONTENTS

A-1. INTRODUCTION

Motorola has initiated the COR (Coherent on Receive) program as a spin-off of the APS-94 product line. The objective of the program is to reduce the aximuth resolution of the APS-94 by a factor of 10; at 50 km (system objective), this implies a reduction from about 1300 ft. to 130 ft. The reduction in resolution will be obtained by creating a synthetic aperture.

The synthetic aperture is created by limiting system errors during the approximately 1/2 second integration time that each target is in the synthetic aperture, and by limiting the time response of each target to 1/2 second or less by passing the doppler-shifted return through a narrow, low-pass filter. If an aircraft has a velocity of 300 [illegible]s, a target at 50 km range is illuminated by the physical beam for approximately 4-1/3 seconds; however, by limiting the doppler-shifted response to the zero doppler region, the 10 to one time reduction is achieved which is necessary to produce the 10 to one reduction in resolution.

Another program objective is to obtain the required performance at a modest cost. Therefore, the hardware implementation needed to create the synthetic aperture must be carefully analyzed in order to eliminate or soften as many specifications as possible.

The various errors in the system manifest themselves as three classes of errors on the imagery: (1) position errors, (2) resolution errors, and (3) sidelobe and S/N errors. The first two types of errors will be discussed in this report.

The first type of error appears on the imagery as a shift in the apparent position of a given target from one resolution element to another during the time that it is being illuminated. Note the following diagram which plots the doppler frequency of a given target as a function of time in the vicinity of cross-over (i.e. when the target is perpendicular to the line of flight):

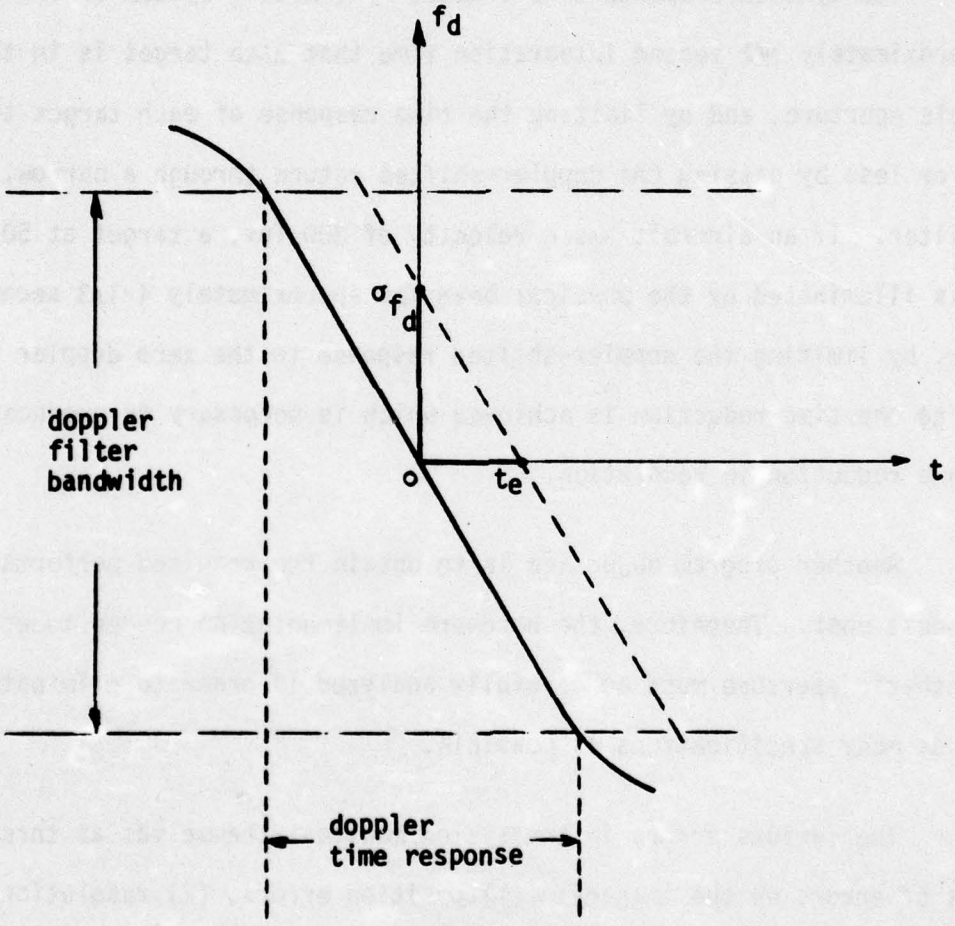

Figure A-1. Shift in the doppler trajectory causing apparent position errors.

In the above diagram, the solid line represents the doppler trajectory without error. The centroid of the time response is centered at t = 0. Now if some doppler error, σ_{f_d}, appears during the integration time such that the response is shifted by some time error, t_e, then although the duration of the doppler time response is the same, its centroid (the centroid of the target imagery on the film) is shifted in position by a distance $P_e = v_a t_e$ where v_a is the aircraft velocity. During the next integration period the frequency error, σ_{f_d}, may shift in a different direction causing the centroid to shift also. This wandering of the apparent position results in a degradation in imagery resolution by smearing one resolution cell into another. The system errors causing this affect are seen to be primarily short term and must occur in times that approximate the time that the doppler trajectory is contained within the limits of the doppler filter.

The second type of error manifests itself in a different manner than the position errors described above. Whereas the latter errors merely shifted the centroid of the doppler trajectory, the errors considered next actually change the slope of the trajectory resulting in a longer dwell time in the doppler filter. Note the following diagram:

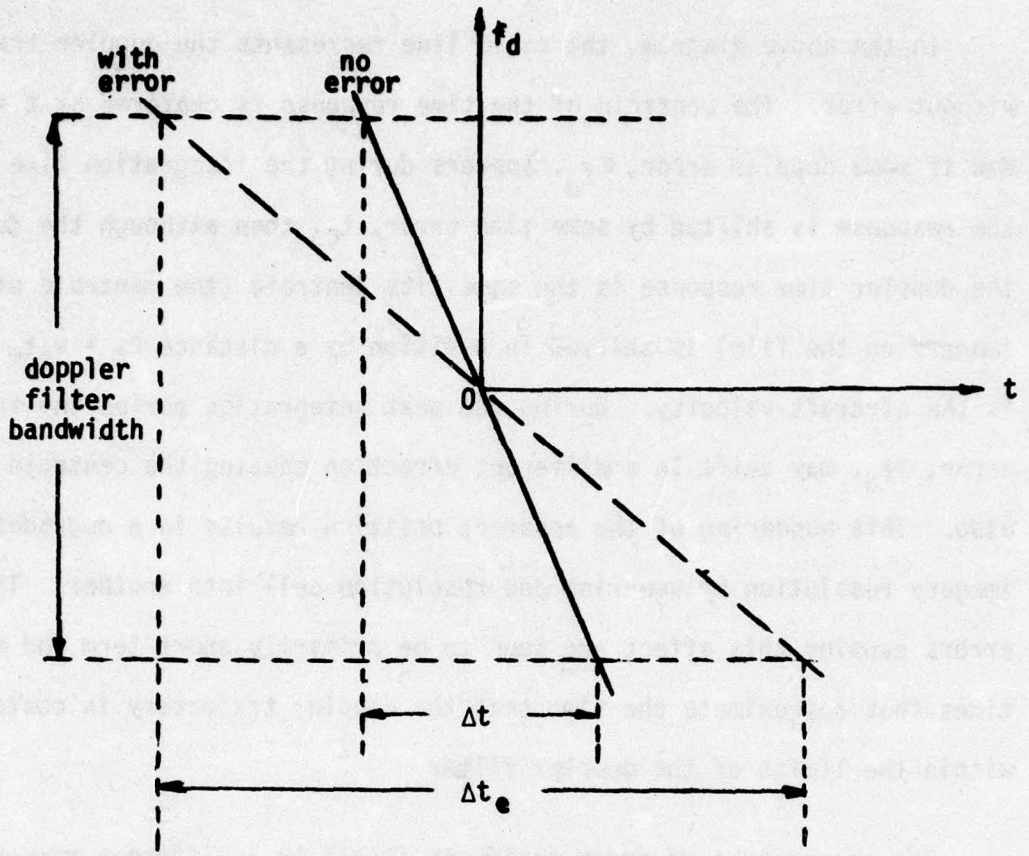

Figure A-2. Change in slope of doppler trajectory causing degradation of resolution.

In the above diagram, the duration of the target imagery increases from Δt seconds to Δt_ϵ seconds; the azimuth resolution correspondingly increases from $v_a \Delta t$ feet to $v_a \Delta t_\epsilon$ feet. The effect considered here has its origin in system acceleration errors.

Therefore, the system errors can be classified as either velocity or acceleration errors. The following paragraphs try to identify the source of each type of error then establish bounds on the errors. The performance guideline is to limit position errors to 25% of a resolution element, and resolution errors to 50% of a resolution element.

A possible sensor package on the aircraft might consist of three-axis accelerometers, a vertical gyro, and the aircraft doppler navigation equipment. The vertical gyro will be used to establish an earth-fixed reference frame.

The accelerometer outputs will be resolved into the earth-fixed reference frame and integrated to give velocity components of aircraft motion. The sensor package cannot be located at the phase center of the antenna; the effect of this offset, aircraft perturbations, and sensor errors will thus be examined.

A final introductory comment is required. Part of the signal processing will be accomplished in the "clutter lock" circuitry. The function of this portion of the receiver is to establish, with a relatively long time constant (five seconds), the average doppler shift at the center of the physical beam. This is done by averaging the doppler shift near the leading edge of the beam with that at the trailing edge. The average doppler is used to produce a zero doppler condition in the beam by tracking out this bias in a clutter tracking loop.

Although the creation of the zero doppler line is done with error, the time constants associated with the wandering of the line about the perpendicular to the flight path are much longer (by 10 to 1) than the 1/2 second that a given doppler trajectory remains in the doppler filter.

The analysis that follows considers the short term variations in motion between the antenna and a given point defined by the zero doppler line.

A-2. SUMMARY

The results of the following paragraphs show that the COR system will probably meet its design objective of 25% degradation in a resolution cell due to position error (velocity dependent errors) and a 50% reduction in resolution due to acceleration errors. However, both of these limits have been reached, with the assumptions that have been made, and no further cushion is available. The data used to obtain the results could easily vary by a factor of two, so an emphatic declaration cannot be justified. For instance, motion induced gyro errors† were not specifically considered. The analysis shows that about 1/4°, perhaps 1/3° of rms gyro error is tolerable. If motion induced errors exceed this, some means of limiting the gyro must be implemented.

The results show that the cross-track velocity and acceleration errors dominate. Because a significant coupling of along-track acceleration errors into the cross-track direction exists, it is necessary to implement accelerometer measurements in all three axes; otherwise, the along-track measurement would not be needed. In addition, some form of yaw angle measurement must be made for the same reason. This angle measurement can be made in a narrow band (with smoothing) and does not need to be instantaneous. The doppler navigation system could provide this information; the angular measurement could have as much as 10% error (see eqn 31 and discussion).

Several major sources of error have been identified: the offset between the location of the sensor package and the antenna phase center gives rise to purely rotational velocities and accelerations. These effects are of the same order of magnitude as the sensor measurement errors. In fact, appendix 3 shows that this error dominates the acceleration errors. The primary cause of this error is the aircraft roll dynamics coupled with the vertical (z-axis)

†i.e., errors caused by aircraft maneuvers.

distance between sensor and antenna. Therefore, real gains can be made by minimizing the offset and reducing aircraft roll motion, especially by dampening the roll motion of the autopilot. If flight experience shows that it is necessary, one might incorporate rate gyros to estimate and eliminate errors due to angular rates or differentiate the angle data.

Another major source of error is the vertical gyro. Errors in verticality cause gravity induced components of error to be coupled into the cross-track accelerometer. If there were no other error sources in the system than that due to cross-track accelerometer error, then a mere 5.9 mg of acceleration error results in a 50% degradation in resolution. When all other sources are included, then the vertical gyro can be allowed to couple only one or two milli-g into the cross-track direction. Realizing that 1 mg in the cross-track direction amounts to only 0.06° of verticality error (see eqn (31)), the demands placed on the gyro become apparent. For similar reasons, corrections must be made to the local value of gravity. Allowing 25% of the allowable 5.9 mg (1.5 mg) to be due to error in the value of "g", then the local value of gravity must be known to within $\pm$ 0.05 fps^2. Therefore, corrections due to latitude, etc. need to be made.

A final note: it is interesting to appreciate that no error in the system with a correlation time that is long compared with 1/2 second causes a serious problem on the imagery. As long as the integrity of each resolution cell is maintained, then slowly varying errors stretch or shrink slightly the entire map. The following paragraphs form a "worst case" analysis in this respect because some of the error may be attributed to energy with spectral components below, say 1 Hz. Even so, the results show that system objectives can probably be met.

A-3. ANALYSIS

The following figure depicts the geometry of the problem:

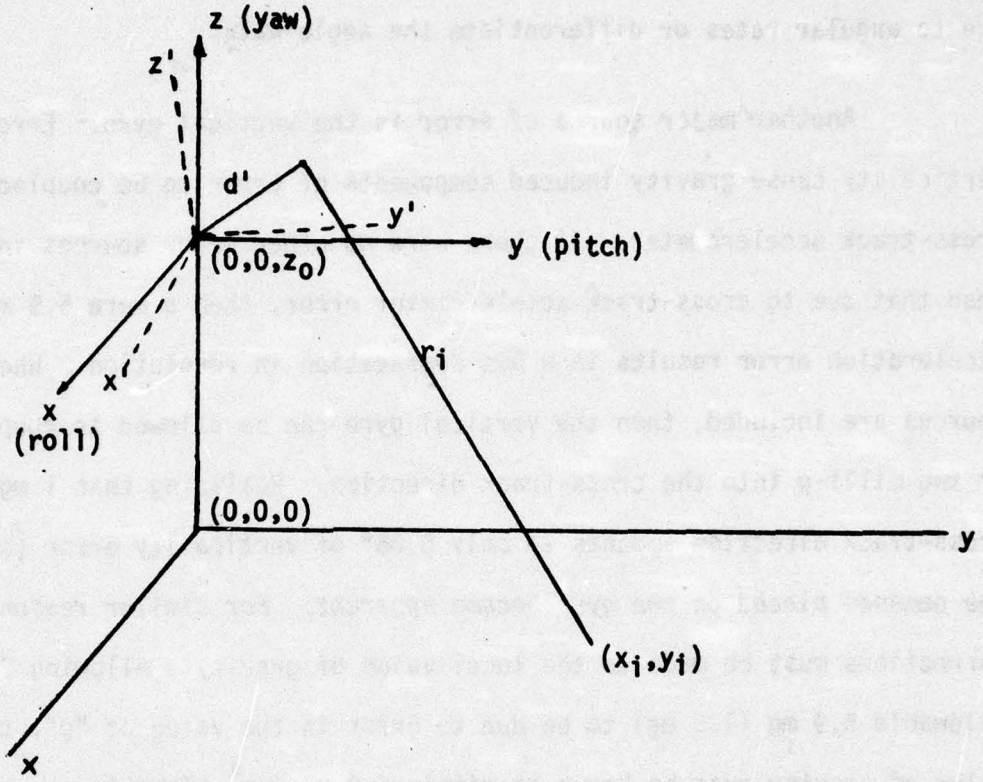

Figure A-3. Geometry of the mapping problem.

In the above figure, the sensor package is located on board the aircraft at coordinates $(0,0,z_0)$. It is assumed that the aircraft is flying along the x-axis. Therefore, the x-axis becomes the roll axis, the y-axis becomes the pitch axis and the z-axis becomes the yaw axis. The phase center of the antenna is located at some vector distance $\underline{d}'$ from the sensor origin. At any instant the orientation of the aircraft-centered coordinate system is shown as the primed axis. The range between the antenna and some particular

point on the ground deduced from the clutter-lock circuit is devoted by r_j; the coordinates of the ground point is x_j and y_j. The range rate and range acceleration of r_j is of interest in the motion compensation problem.

A-4. IMAGE POSITION ERROR

As a first step in the solution of the problem, the vector $\underline{d}'$ must be transformed from the primed to the unprimed coordinate system. It can be shown (ref 1) that the successive rotation of yaw, roll, and pitch define a transformation matrix that is orthogonal; that is $M^T = M^{-1}$ and the measured angles, yaw, roll, and pitch define an Euler set of coordinates. Furthermore, the gimbles of the vertical gyro are structured to produce the ordered set: roll-pitch. When pre-multiplied by the yaw transformation, an overall transformation matrix M is defined (ref 1, p. 16-18).† The effect of the transformation M on the motion compensation problem is discussed in the section entitled "Implementing the Doppler Correction." Any vector in the primed coordinate system is transformed to the inertial reference frame by

$$\underline{d} = M^{-1}\,\underline{d}' \tag{1}$$

and

$$M^{-1} = \begin{bmatrix} cy \cdot cp & -sy \cdot cr + cy \cdot sp \cdot sr & sy \cdot sr + cy \cdot sp \cdot cr \\ sy \cdot cp & cy \cdot cr + sy \cdot sp \cdot sr & -cy \cdot sr + sy \cdot sp \cdot cr \\ -sp & cp \cdot sr & cp \cdot cr \end{bmatrix} \tag{2}$$

where sy and cy denote sin ϕ_y, Cos ϕ_y where ϕ_y is the yaw angle; symbols for roll and pitch follow similarly. Let

$$\underline{D} = \underline{d} + \underline{v}t \tag{3}$$

(for which it is assumed that the vector velocity is constant for the 1/2 second of interest), so that

---

†When the vertical gyro is obtained, care must be exercised that the positive sense of roll and pitch corresponds to the directions assumed here; if not, then appropriate sign changes in these equations must be introduced.

$$r_i^2 = (D_x - x_i)^2 + (D_y - y_i)^2 + (D_z + z_0 - 0)^2 \tag{4}$$

and $$\dot{r}_i = (D_x - x_i)\frac{\dot{D}_x}{r_i} + (D_y - y_i)\frac{\dot{D}_y}{r_i} + (D_z + z_0)\frac{\dot{D}_z}{r_i} \tag{5}$$

where, using (1) and (2), and making use of the fact that sin $\phi \sim \phi$ and Cos $\phi \sim 1$, one obtains:

$$\dot{r}_i = (d_x + \dot{x}t - x_i)\left(\frac{\dot{d}_x + \dot{x}}{r_i}\right)(d_y + \dot{y}t - y_i)\left(\frac{\dot{d}_y + \dot{y}}{r_i}\right) + (d_z + \dot{z}t + z_0)\left(\frac{\dot{d}_z + \dot{z}}{r_i}\right) \tag{6}$$

where

$$\begin{aligned} d_x &= \Delta x' - \phi_y \Delta y' + \phi_p \Delta z' \\ d_y &= \phi_y \Delta x' + \Delta y' - \phi_r \Delta z' \\ d_z &= -\phi_p \nabla x' + \phi_r \Delta y' + \Delta z' \end{aligned} \tag{7}$$

and

$$\begin{aligned} \dot{d}_x &= (-\phi_p\dot{\phi}_p - \phi_y\dot{\phi}_y)\Delta x' + (-\dot{\phi}_y + \phi_r\dot{\phi}_p + \phi_p\dot{\phi}_r) + (\phi_y\dot{\phi}_r + \phi_r\dot{\phi}_y + \dot{\phi}_p)\Delta z' \\ \dot{d}_y &= \dot{\phi}_y\,\Delta x' + (-\phi_r\dot{\phi}_r - \phi_y\dot{\phi}_y)\,\Delta y' + (-\dot{\phi}_r + \phi_y\dot{\phi}_p + \phi_p\dot{\phi}_y)\Delta z' \\ \dot{d}_z &= -\dot{\phi}_p\,\Delta x' + \dot{\phi}_r\,\Delta y' - (\phi_p\dot{\phi}_p + \phi_r\,\dot{\phi}_r)\Delta z' \end{aligned} \tag{8}$$

In equations (6) $\dot{x}$, $\dot{y}$, $\dot{z}$ are the components of the sensor package velocity as measured in inertial space. Therefore, the accelerometer measurements must first be transformed as in (7). Also $\Delta x'$, $\Delta y'$, $\Delta z'$ are the components of $\underline{d}'$ in the primed coordinate system; their values are about 1, 1/3, -1 ft.

Next, the expression for the measured value of range rate $\dot{r}_m$, will be derived; the difference between $\dot{r}_m$ and equation (6) is the error that must be examined. But first, a few comments are in order. It would be desirable to eliminate the measurement of short term, instantaneous yaw angle variations. The sensor package would then measure roll and pitch only. This elimination might be suggested because the clutter lock circuit, in effect, provides a long term, "average" yaw measurement. Also, the antenna has some yaw stabilization; the short term yaw variations will be much smaller than the aircraft yaw motion. In the above equations, then, yaw angle will be eliminated from $\dot{r}_m$ and the resulting error term will be evaluated. (It is shown later that the long term error between the velocity vector and the antenna axis must be measured.)

Another quantity that must be eliminated from $\dot{r}_m$ is $\underline{\dot{d}}$, where $\underline{\dot{D}} = \underline{\dot{d}} + \underline{\dot{v}}$ in equation (5), because no means will be provided to measure angular rates.

With the above restrictions, the error between the true value of range rate and its measured value, $\delta\dot{r} = \dot{r}_i - \dot{r}_m$, becomes:

$$r_i\delta\dot{r} = (d_x + \dot{x}t - x_i)\dot{d}_x - (\phi_y\Delta_y'\dot{x} + d_{xm}\dot{\varepsilon_x}) - (2x\dot{\varepsilon_x} + \dot{\varepsilon_x}^2)t + x_i\dot{\varepsilon_x}$$

$$+ (d_y + \dot{y}t - y_i)\dot{d}_y + (\phi_y\Delta x'\dot{y} - dy_m\dot{\varepsilon y}) - (2\dot{y}\dot{\varepsilon_y} + \dot{\varepsilon_y}^2)t + y_i\dot{\varepsilon_y} \qquad (9)$$

$$+ (d_z + \dot{z}t + z_0)\dot{d}_z - d_{zm}\dot{\varepsilon_z} - (2\dot{z}\,\dot{\varepsilon_z} + \dot{\varepsilon_z}^2)t - (\varepsilon_z\dot{z} + z_0\dot{\varepsilon}_z + \varepsilon_z\dot{\varepsilon_z})$$

where all parameters with subscripted "m" refer to measured values, and "ε" denotes the error between the true value and measured value. The errors in (9)

can be interpreted in several ways: first of all, they may be considered as instrument errors only in which case long term and short term errors must be considered separately.

On the other hand, if the instruments are considered to be perfect, then the errors can be thought of as differences between the clutter lock values (long term) and the short term variations due to aircraft dynamics.

Consider the first case above. Then $\varepsilon_{\dot{x}}$, $\varepsilon_{\dot{y}}$, $\varepsilon_{\dot{z}}$ are the integrated accelerometer errors, and ε_z is the error in the altimeter. The accelerometer errors have zero mean whereas the altimeter generally has a bias. It can be shown that the long term mean of (9) is almost zero, the terms $(\varepsilon_{\dot{x}}^2 + \varepsilon_{\dot{y}}^2 + \varepsilon_{\dot{z}}^2)t$ being the exception; but, for reasonable accelerometer errors, these terms are small compared to the true range rate, $v_a^2 t/r_i$ where v_a is the average along-track aircraft velocity.

The evaluation of the rms range rate error, of interest here, uncovers terms that are not insignificant. But first, estimates of typical aircraft dynamics must be made.

Aircraft angular rates and accelerations can be determined from existing data (ref 2) as shown in Figures 4, 5, 6. These figures show the spectral densities of the yaw, roll, and pitch angles for a B-66. Assuming that this data is typical for the aircraft that may be used in this application, then the curves there may be integrated numerically to give σ_{ϕ_y}, σ_{ϕ_r}, σ_{ϕ_p}. Because $s_{\dot{\phi}} = \omega^2 s_\phi$, and $s_{\ddot{\phi}} = \omega^4 s_\phi$ where s denotes the spectral density, the rms values for angular rates and angular accelerations can also be derived; they are shown in Table 1. The correlation times are longer than 1/2 second, so the rms values could possibly be reduced; however, lacking detailed information

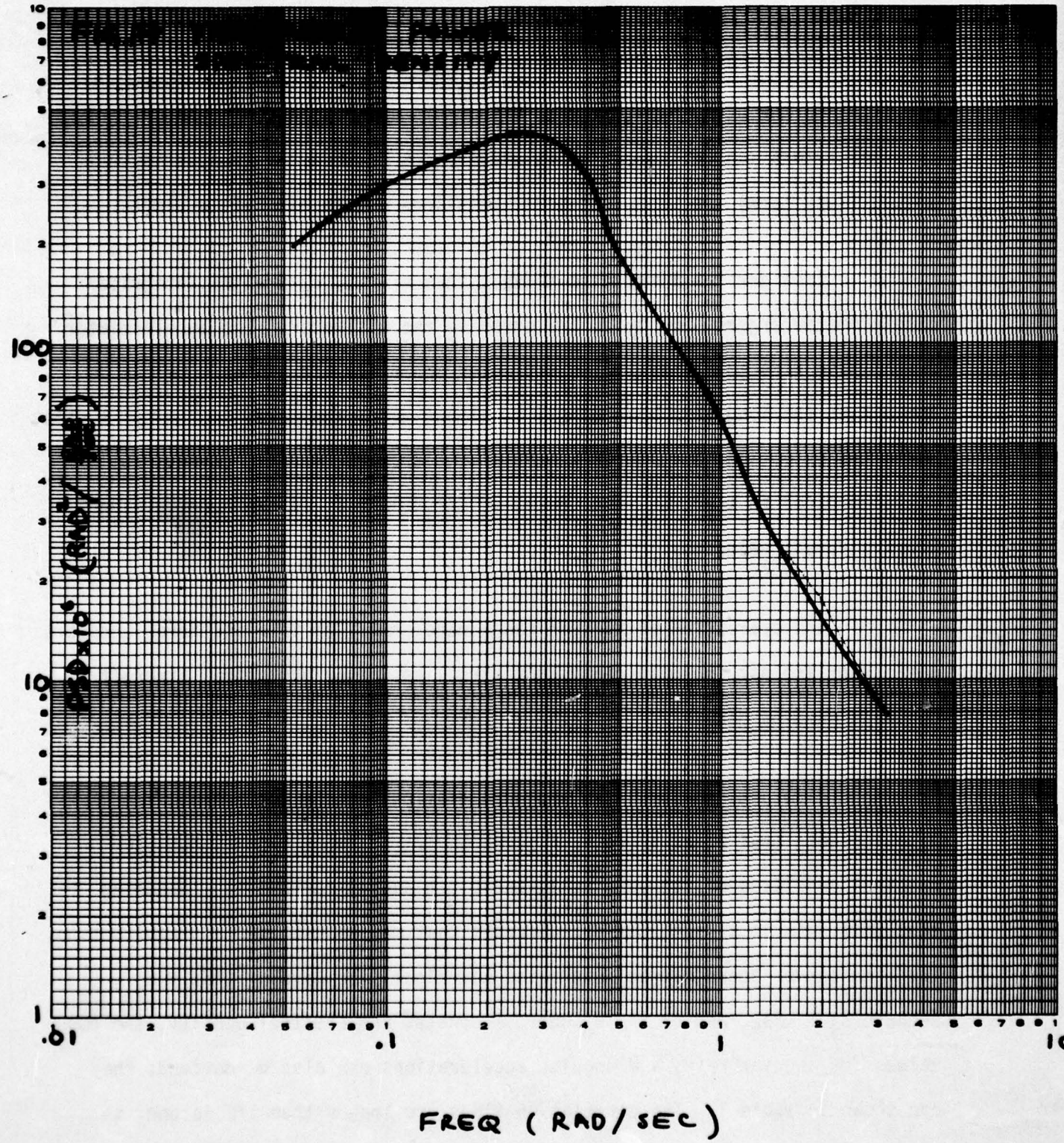
100
10
1
.01
.1
1
10
FREQ (RAD/SEC)

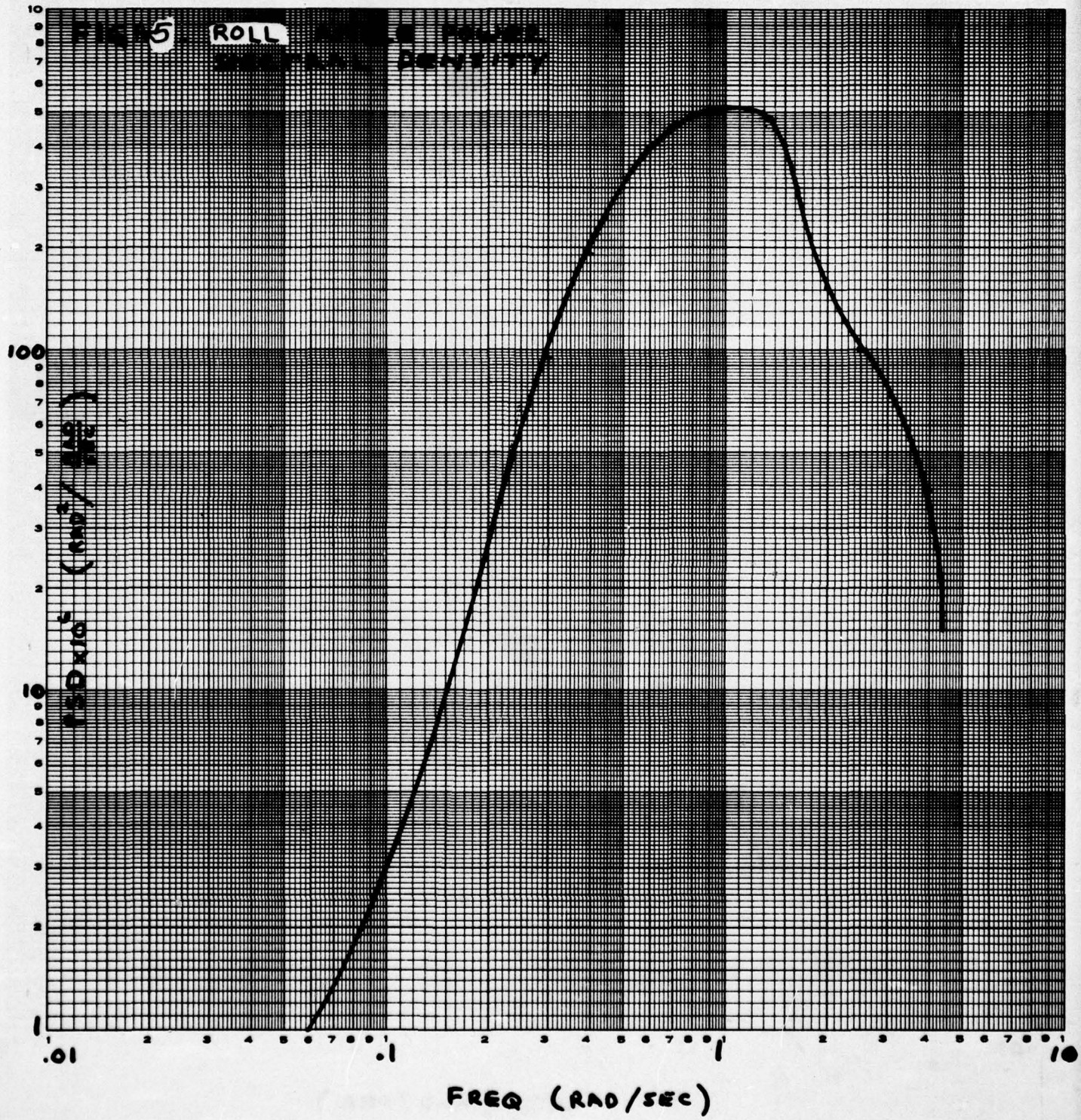
ROLL
FREQ (RAD/SEC)

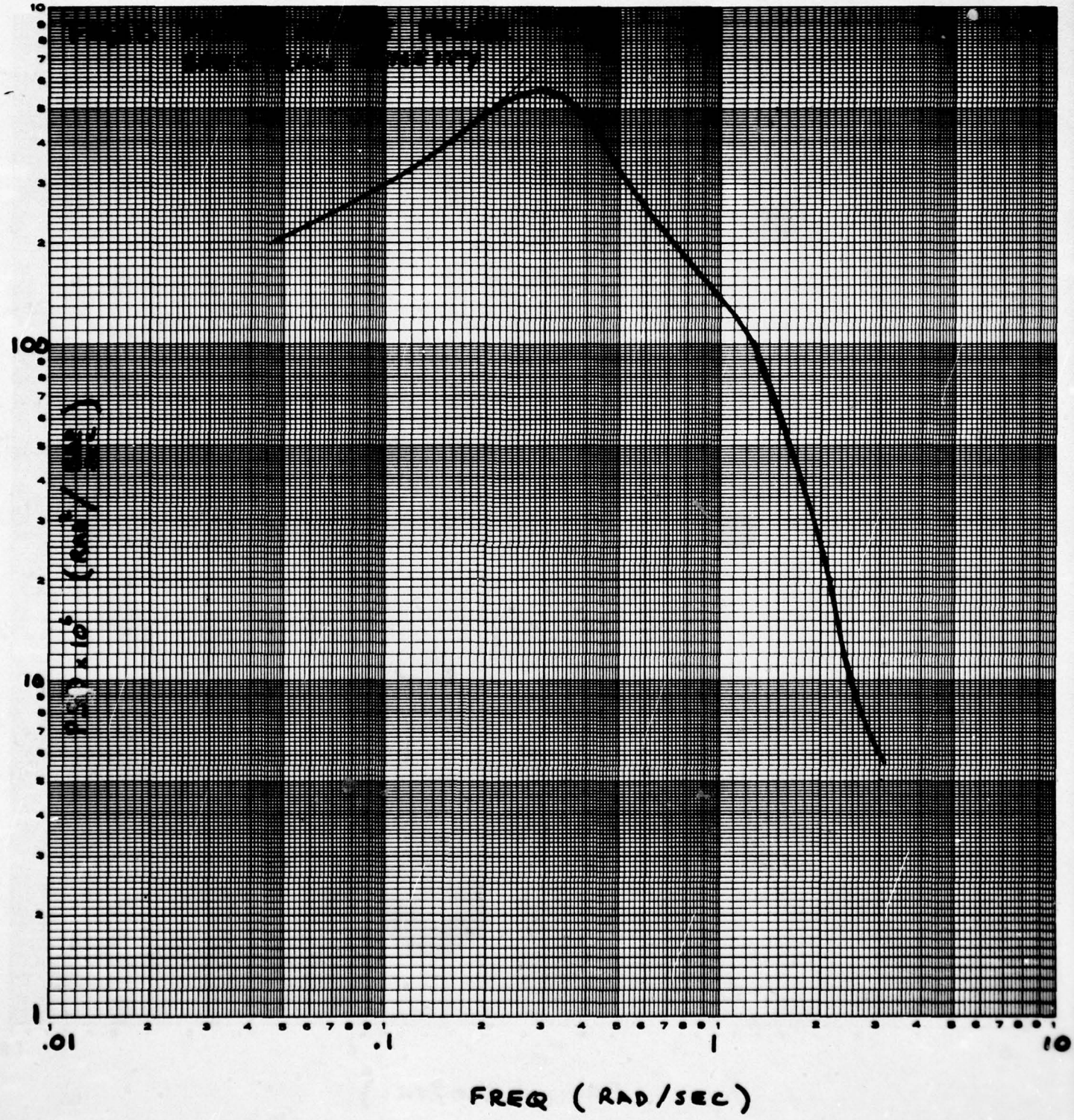
100
10
1
.01
.1
1
10
FREQ (RAD/SEC)

AD-A035 032 MOTOROLA INC SCOTTSDALE ARIZ GOVERNMENT ELECTRONICS DIV F/G 17/9
PERFORMANCE OF COHERENT-ON-RECEIVE SYNTHETIC APERTURE SIDE LOOK--ETC(U)
OCT 76 D E FRASER, G V MORRIS F42600-75-A-1861

UNCLASSIFIED GED-2213 USCG-D-109-76 NL

2 OF 2
AD A035032

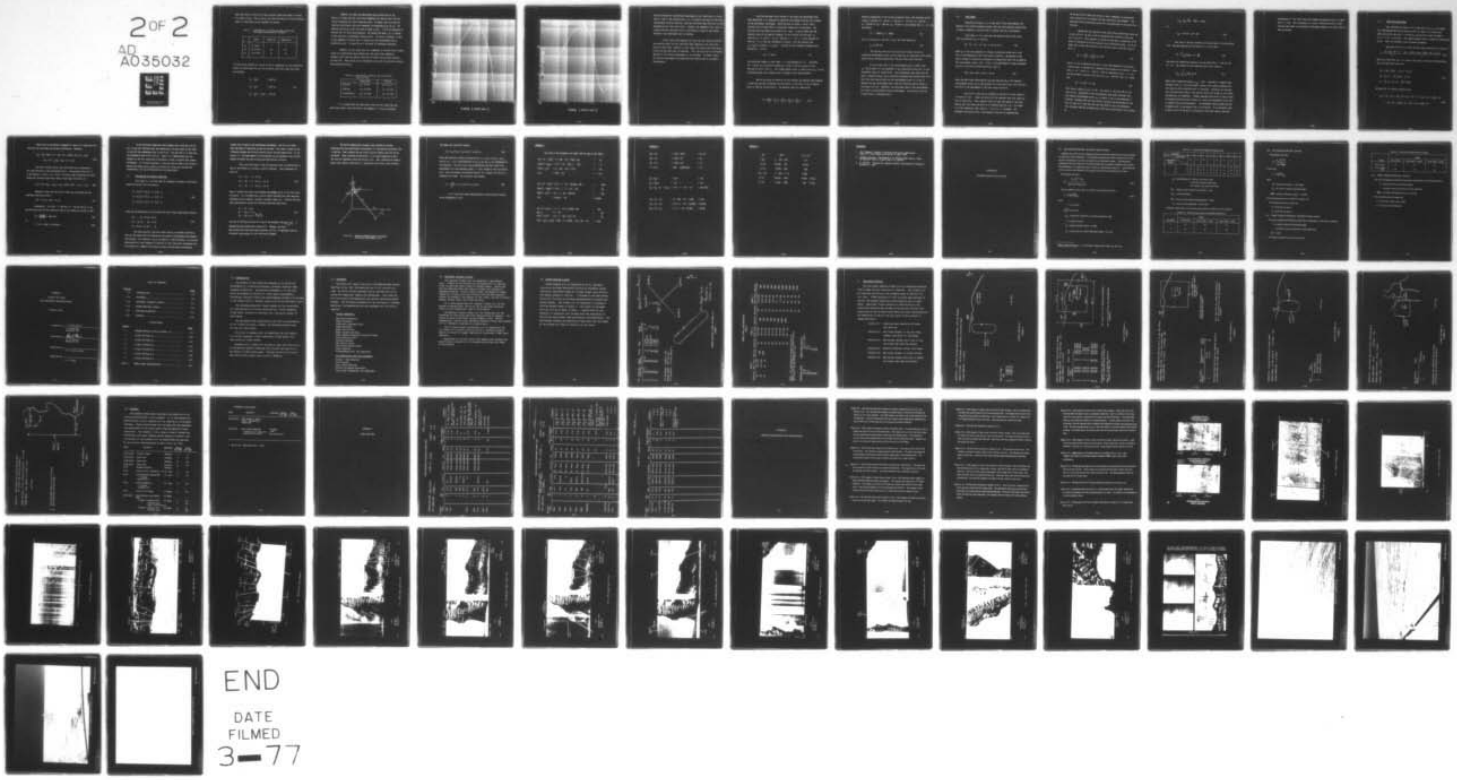

END

DATE FILMED
3-77

about the actual aircraft to be used, possible reductions might be limited to a factor of two. Also $s_{\dot{\phi}}$ and $s_{\ddot{\phi}}$ are wider band than s_ϕ so the correlation times of $\dot{\phi}$ and $\ddot{\phi}$ may actually approach 1/2 second.

Table A-1. Experimental, rms values of angle, angle rate and angle acceleration for the B-66.

	$\sigma\phi$(mr)	$\sigma\dot{\phi}$(mr/sec)	$\sigma\ddot{\phi}$(mr/sec^2)
ϕ_y	15 (.86°)	7	7
ϕ_r	32 (1.83°)	52	151
ϕ_p	19 (1.09°)	16	31

If these values (reduced by a factor of two to compensate for the correlation times) are substituted into (8) the following significant terms and values are obtained:

$$\dot{d}_x \sim \dot{\phi}_p \Delta z' = .008 \text{ fps}$$

$$\dot{d}_y \sim \phi_r \Delta z' = .026 \text{ fps} \qquad (10)$$

$$\dot{d}_z \sim \phi_p \Delta x' + \phi_r \Delta y' = .012 \text{ fps}$$

Appendix one shows the approximate value of each term in (9). There it is shown that the cross-track components of velocity error (row two of eqn 9) dominate the total range-rate error. Of these, the first and last terms are significant; the error components are dominated by $\dot{d}_y$ and $\varepsilon\dot{y}$. The dominant term in $\dot{d}_y$ is the roll-rate as shown in (10). It will be important to minimize the roll-rate during mapping. The second term above, $\varepsilon\dot{y}$, is related to the cross-axis accelerometer velocity error. Its error is related, in turn, to the component of gravity that is coupled into the accelerometer due to verticality error. The gyro error is discussed in subsequent paragraphs.

Appendix one also shows that the x-component of velocity errors (along track) are insignificant when compared with the cross-track components. Figures 7 and 8 show the spectral densities of lateral and vertical position for the B-66. These curves can be integrated to give the rms position, velocity, and acceleration errors.

Table A-2. Rms position, velocity, and acceleration error for B-66.

	Cross-Track	Vertical
position	σ_y = 6.9 ft	σ_z = 6.2 ft
velocity	$\sigma_{\dot{y}}$ = 4.6 fps	$\sigma_{\dot{z}}$ = 3.5 fps
acceleration	$\sigma_{\ddot{y}}$ = 4.3 fps^2	$\sigma_{\ddot{z}}$ = 3.3 fps^2

If it assumed that the along-track errors are not larger than the cross-track errors, then from Table 2 and appendix 1, it can be concluded

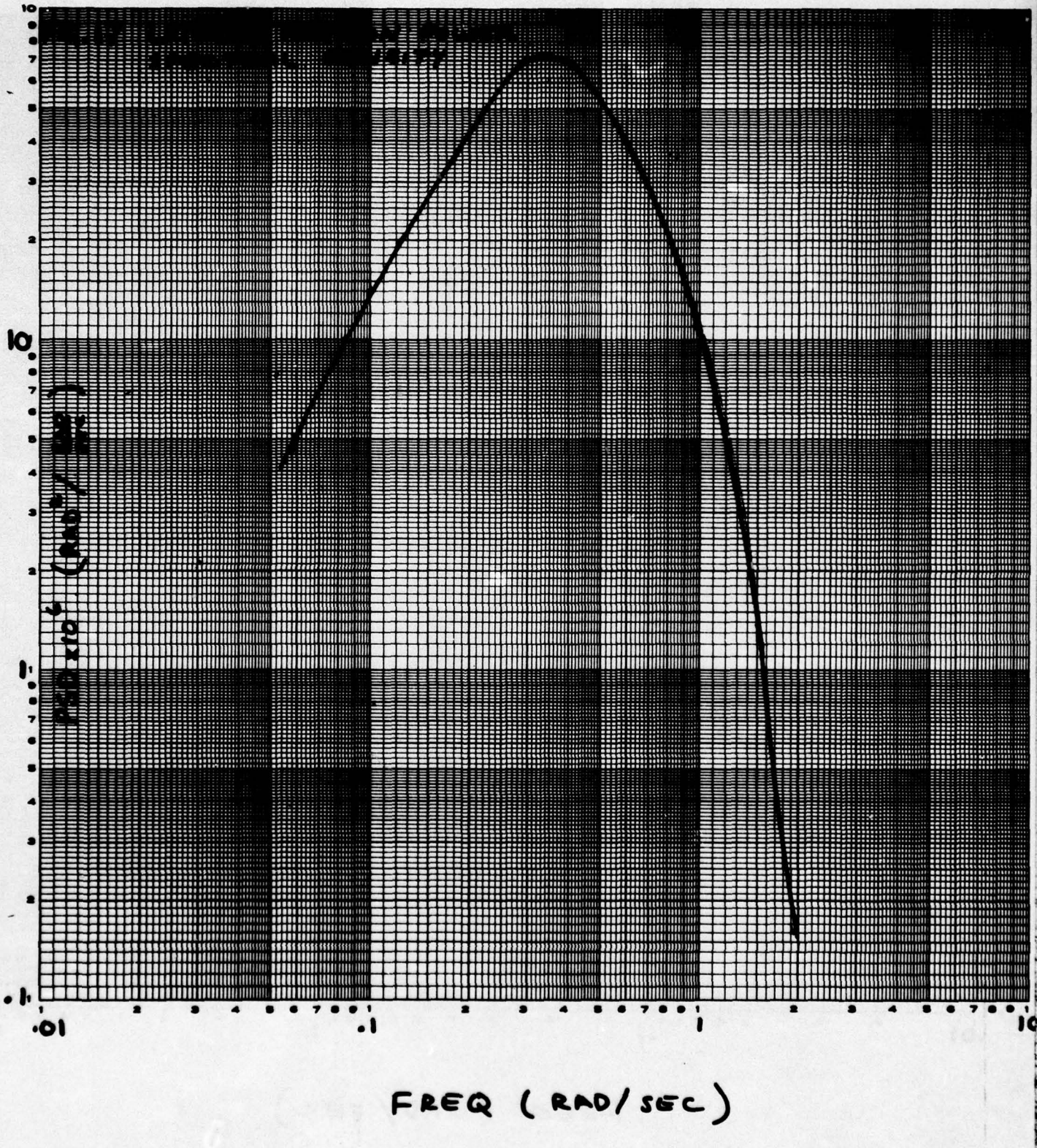
10
1
.1
.01
1
.1
FREQ (RAD/SEC)

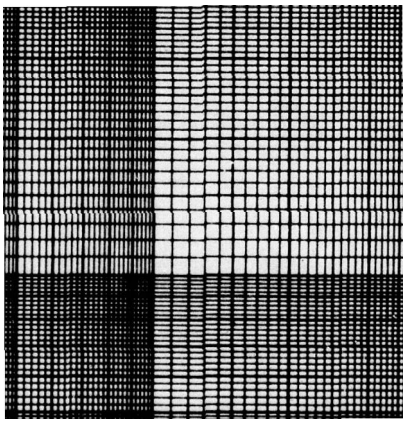

that the along-track accelerometer measurement is not significant in itself. That is, even if the velocity error, $\dot{\varepsilon}_x$, is allowed to be equal to the total instantaneous velocity deviation, then the resulting range rate error is still dominated by the cross-track errors. However, the component of a_x' that is coupled into the cross-track axis is significant as shown in (31) below; therefore, this measurement must be retained.

A final result from appendix one shows that the vertical position and velocity errors are not significant when compared to the cross-track errors at long range. However, at near range, the vertical and cross-track errors have the same order of magnitude. Also, the last term in (9) becomes dominant if the vertical measurement is not included. For these reasons, the vertical measurement of acceleration and velocity must be included in the processor.

Now that the major error sources in the range rate measurement have been identified, it is necessary to determine the maximum velocity error allowed by the performance requirement. Referring back to Figure 1, recall that a position error of about 25% of a resolution element will be tolerated. The position error was shown to be given by $P_e = v_a t_e$. It can be shown that the expected value of the doppler frequency, in the vicinity of cross-over, is given by $f_d = -2\, v_a^2 t/\lambda r$. For v_a = 300 fps, λ = .1 ft, r = 50 km (164,000 ft), then $f_d = -11\, t$; from the information in Figure 1, one thus obtains that $t_e = \sigma_{f_d}/11$ so that $P_e = v_a\, \sigma_{f_d}/11$. Solving for the allowable frequency error obtains at r = 50 km:

$$\sigma_{f_d} \leq 11\, P_e/v_a \qquad (11)$$

The resolution element at some range, r, is approximated by $\sqrt{\lambda r}$. Therefore, at r = 50 km, the resolution element has a value of 130 ft; P_e must be less than 25% of this or 32.5 ft. The allowed doppler error is found to be $\sigma_{f_d} \leq 1.19$ Hz at maximum range; the allowable error increases as the range decreases.

Now we can return to equation (9) and evaluate the dominant terms keeping in mind that the RSS of equation (9) must result in less than 1.2 Hz of doppler error or 0.06 fps velocity error. The dominant terms are shown below:

$$\dot{\delta r} = \frac{2\dot{x}\dot{\varepsilon_x}t}{r_i} + \frac{x_i}{r_i}\dot{\varepsilon_x} - \frac{y_i}{r_i}\dot{d}_y + \frac{y_i}{r_i}\dot{\varepsilon_y} + \frac{z_o}{r_i}\dot{\varepsilon_z} \qquad (12)$$

Assuming independence of the various parameters above, and inserting typical values of interest (r_i = 50 km, $\dot{x}$ = 300 fps, t = 1/2 sec, x_i = 1430 ft, y_i = 163,695 ft, $\dot{d}_y$ = .026 fps, z_o = 10,000 ft, and assuming that $\dot{\varepsilon}_x = \dot{\varepsilon y} = \dot{\varepsilon z}$), one obtains

$$\sigma_{\dot{r}}^2 = 1.00008\ \sigma_{\dot{y}}^2 + .00068 \qquad (13)$$

with $\sigma_{\dot{r}}$ restricted to 0.06 fps or less, the above reduces to

$$\sigma_{\dot{y}} \leq 0.054 \text{ fps} \qquad (14)$$

The velocity error will have two major sources, one due to integrated accelerometer noise, and the other due to random gyro drifts which couple gravity induced accelerations into the cross-track direction.

It can be shown that if the accelerometer noise is white, then $\sigma_{\dot{y}}^2 = \frac{T}{B}\sigma_{\ddot{y}}^2$ where B is the bandwidth of the acceleration noise and T is the integration time (1/2 second here). The accelerometer spec shows that the noise, although colored, has an equivalent bandwidth much greater than 10 Hz. With (14), and assuming that the rms accelerometer error is 1.2 mg, as deduced from the accelerometer spec, then the resulting velocity noise is only about 0.01 fps. Therefore, the broad-band noise of the accelerometer will lead to a satisfactory velocity measurement. The velocity noise due to gyro errors is considered next.

A-5. GYRO ERRORS

Returning to Figure 3, it is seen that if the accelerometers are mounted in the primed coordinate system, then the total measured acceleration includes a component of gravity that is coupled into the accelerometer.

From Figure 3, it is seen that the measured value of the cross-track acceleration, A'_y, is given by

$$A'_y = a'_y - g\,\underline{k}\cdot\underline{j}' = a'_y - g\cos\phi_p \sin\phi_r \qquad (15)$$

where a'_y is the true component of dynamic acceleration along the y'-axis and y is the magnitude of the local value of gravity. The purpose of the sensor package is to derive an estimate of $g\cdot\cos\phi_p\cdot\sin\phi_r$ which can be added to the accelerometer output, (15). Errors in the measurement of these parameters lead to a cross-track acceleration error, $\varepsilon A'_y$, of

$$\varepsilon A'_y = \varepsilon a_m + g\varepsilon\phi_r + \varepsilon g\cdot\phi_r + \varepsilon g\cdot\varepsilon\phi_r \qquad (16)$$

where the small angle approximation has been made and εa_m is the inherent accelerometer error, $\varepsilon\phi_r$ is the platform roll error due to gyro error and εg is the error in the measurement of the local value of gravity.

The errors in (16) must be examined on the basis of their change in 1/2 second or less. Slower variations will be examined later with regard to less in resolution. From a spectral point of view, the energy in the error spectra that lies above one Hertz is of interest here (If $2\,\beta_L = 1/t_i$ where t_i is the integration time, then $\beta_L = 1$ Hz if $t_i = .5$ seconds). The allowable verticality error, given equation (14), will be examined next.

As the gyro drifts about the vertical, then a component of acceleration due to gravity will be coupled into the cross-track accelerometer. The spectrum of this acceleration noise will be proportional to the gyro error spectrum.

Assume that the spectrum of the cross-track acceleration noise due to gyro drift is low pass, with an autocorrelation function of the form $R(\tau) = \sigma_{\ddot{y}}^2 e^{-\alpha\tau}$. This spectrum is similar to that due to random gyro drift which is considered to be the source of this acceleration noise. It can be shown (ref 3) that the variance of the velocity noise, given this type of $R(\tau)$, is

$$\sigma_{\dot{y}}^2 = 4 \frac{\sigma_{\ddot{y}}^2 T}{\alpha} - \frac{2 \sigma_{\ddot{y}}^2}{\alpha^2} (1-e^{-2\alpha T}) \qquad (17)$$

where T is the integration time and α is the 3-dB bandwidth of the process. A typical gyro is equiped with a pendulum time constant of 25 seconds. Therefore, $\alpha = 2\pi \cdot 1/50$ or $\alpha = .126$ rps. With an integration time, $T = .5$ sec, and the allowable velocity noise from (14), $\sigma_{\dot{y}} = .054$ fps, then it is found that

$$\sigma_{\ddot{y}} = .11 \text{ fps}^2 = 3.4 \text{ mg} \qquad (18)$$

This value is equal to $\sigma_{\varepsilon A'}$ in (16). The errors in (16) must RSS to less than 3.4 mg. Examination of the accelerometer data sheet indicates that the inherent accelerometer error $\sigma_{\varepsilon a}$, is about 1.2 mg in the bandwidth of interest. Assuming that the local value of gravity can be measured to less than 1%, then it is seen that the last two terms of (16) are negligible. This indicates that the allowable gyro drift due to noise above 1 Hz is given by

$$\sigma^2_{\varepsilon\phi} = \frac{1}{g^2}\left(\sigma^2_{\varepsilon A'} - \sigma^2_{\varepsilon a}\right) = 13 \text{ mr}^2$$

or

$$\sigma_{\varepsilon\phi} = 3.61 \text{ mr} = .21° \text{ rms} \qquad (19)$$

Now, what is the rms variation of the gyro due to its noise above 1 Hz? The gyro spectrum has the form $k/(\alpha^2 + \omega^2)$ so that

$$\sigma^2_{\phi} = \int_0^{\infty} \frac{k}{(\alpha^2 + \omega^2)}\, d\omega = \frac{\pi k}{2\alpha} \qquad (20)$$

from which the normalizing constant k can be found with $\alpha = 1.26$ rps and $\sigma\phi = .5°$. The integral of this spectrum from 1 Hz is given by

$$\sigma^2_{1\text{Hz}} = \int_{2\pi\cdot 1}^{\infty} \frac{k}{(\alpha^2 + \omega^2)}\, d\omega \qquad (21)$$

Numerically integrating obtains $\sigma_{1\text{Hz}} = .072°$. Therefore, it appears that the gyro (with $\sigma\phi = 1/2°$) has about a factor of two cushion compared with (19) above as far as position error is concerned. Therefore, we conclude that the objective of 25% or less position error will be met as far as gyro perturbations are concerned. Another important gyro error is that of bias. A constant verticality error results in a constant acceleration error that is coupled into the accelerometers. The subsequent section shows that the allowable error in the doppler rate is 3.67 Hz/sec. If an arbitrary limit of 25% of this (.92 Hz/sec) is allocated to this error source, then the

relationship $\dot{f} = 2a/\lambda$ shows that the allowable acceleration bias is 0.0459 fps^2 or 1.4 mg. This corresponds to a static verticality error of 0.08°. The gyro spec needs to be examined to determine whether or not this requirement can be met.

A-6. IMAGE RESOLUTION ERROR

Now, returning to Figure 2, it is seen that if $\Delta t_\epsilon \leq 1.5\ \Delta t$ (implying a 50% degradation) and $\dot{f}_d$ (with no error) is equal to -11 Hz/sec (as shown previously) then $\dot{f}_{d\epsilon} = -7.33$ Hz/sec, and the error slope can amount to -11 + 7.33 = 3.67 Hz/sec. The reduced doppler slope is caused by acceleration errors. These are examined in the following paragraphs.

Beginning with (5) it is seen that the range acceleration is given by

$$\ddot{r}_i = \frac{\dot{D}_x^2 + \dot{D}_y^2 + \dot{D}_z^2 - \dot{r}_i^2}{r_i} + \frac{(D_x - X_i)\ \ddot{D}_x + (D_y - Y_i)\ddot{D}_y + (D_z + Z_0)\ \ddot{D}_z}{r_i} \tag{22}$$

where $\underline{\dot{D}}$ is found from (3), $\dot{r}$ is found in (6) and $\underline{\ddot{D}}$ is found by differentiating (8); the significant terms are

$$\begin{aligned}
\ddot{d}_x &= -(\phi_p^2 + \dot{\phi}_y^2)\Delta x' - \ddot{\phi}_y\ \Delta y' + \ddot{\phi}_p\ \Delta z' \\
\ddot{d}_y &= \ddot{\phi}_y\ \Delta x' - (\dot{\phi}_r^2 + \dot{\phi}_y^2)\Delta y' - \ddot{\phi}_r\ \Delta z' \\
d_z &= -\ddot{\phi}_p\ \Delta x' + \ddot{\phi}_r\ \Delta y' - (\dot{\phi}_p^2 + \dot{\phi}_r^2)\Delta z'
\end{aligned} \tag{23}$$

Writing (22) in slightly different form,

$$\begin{aligned}
r_i\ddot{r}_i = {} & (\dot{d}_x + \dot{x})^2 + (\dot{d}_y + \dot{y})^2 + (\dot{d}_z + \dot{z})^2 - \dot{r}_i^{\,2} + (d_x + \dot{x}t - x_i)(\ddot{d}_x + \ddot{x}) \\
& + (d_y + \dot{y}t - y_i)(\ddot{d}_y + \ddot{y}) + (d_z + \dot{z}t + z_0)(\ddot{d}_z + \ddot{z})
\end{aligned} \tag{24}$$

These terms are evaluated in appendix 2; there it is shown that the first and last two terms are the most significant. Therefore,

$$r_i\ddot{r}_i \approx \dot{d}_x^2 + 2\dot{d}_x\dot{x} + \dot{x}^2 + (dy + \dot{y}t - y_i)\ddot{d}_y + (d_y + \dot{y}t - y_i)\ddot{y} + (d_z + \dot{z}t + z_0)\ddot{d}_z + (d_z + \dot{z}t + z_0)\ddot{z} \quad (25)$$

The first, second, fourth, and sixth terms are not measured at all; they form part of the acceleration error. The measured value of $\ddot{r}$ is of the form $\dot{x}_m^2 + (y)(\ddot{y} + \varepsilon\ddot{y}) + (z)(\ddot{z} + \varepsilon\ddot{z})$ which, when subtracted from (25), leaves the following significant terms in the range rate error, $\sigma\ddot{r}$:

$$r_i\delta\ddot{r} = \dot{d}_x^2 + 2\dot{d}_x\dot{x} - y_i\ddot{d}_y + z_0\ddot{d}_z - (2\dot{x}\varepsilon\dot{x}^2 + \varepsilon\dot{x}^2) - y_i\,\varepsilon\ddot{y} - z_0\varepsilon\ddot{z} \quad (26)$$

Appendix 3 shows that the third, fifth, and sixth terms are the remaining significant terms:

$$r_i\delta\ddot{r} = -y_i\,\ddot{d}_y - 2\dot{x}\varepsilon\dot{x} - y_i\,\varepsilon\ddot{y} \quad (27)$$

Assuming $\ddot{d}_y = .151$ fps^2, $\dot{x} = 300$ fps, $\varepsilon\dot{x} = .04$ fps and $\varepsilon\ddot{y} = 2$ mg, the RSS total error of the right-hand side of (27) amounts to 26,872 so that

$$\delta\ddot{r} = \frac{26,872}{164,000} = .1639 \text{ fps}^2 \quad (28)$$

or

$$\ddot{r} = 20 \times .1639 = 3.28 \text{ Hz/sec} \quad (29)$$

It was previously shown that the allowable error slope was 3.67 Hz/sec, so eqn (29) indicates that the system errors are just about at the limit. In eqn (27) the predominant error is due to $\ddot{d}y$. From eqn (23) it is seen that the predominant term in $\ddot{d}y$ is $\ddot{\phi}_r \Delta a'$. Again, it is demonstrated that the dynamics of the roll angle must be minimized in order to achieve best systems performance. If it proves necessary, a rate gyro may be added to the system to measure and reduce errors caused by aircraft roll rates and accelerations; alternatively, one may differentiate the indicated angles.

A-7. IMPLEMENTING THE DOPPLER CORRECTION

From Figure 3, it is seen that the components of dynamic acceleration along the inertial axis are given by

$$\begin{aligned} a_x &= a_{x'} \underline{i'} \cdot \underline{i} + a_{y'} \underline{j'} \cdot \underline{i} + a_{z'} \underline{k'} \cdot \underline{i} \\ a_y &= a_{x'} \underline{i'} \cdot \underline{j} + a_{y'} \underline{j'} \cdot \underline{j} + a_{z'} \underline{k'} \cdot \underline{j} \\ a_z &= a_{x'} \underline{i'} \cdot \underline{k} + a_{y'} \underline{j'} \cdot \underline{k} + a_{z'} \underline{k'} \cdot \underline{k} \end{aligned} \tag{30}$$

Using the transformation (2) and invoking the small angle approximation obtains:

$$\begin{aligned} a_x &= a_{x'} - \phi_y a_{y'} + \phi_p a_{z'} \\ a_y &= \phi_y a_{x'} + a_{y'} - \phi_r a_{z'} \\ a_z &= -\phi_p a_x + \phi_r a_{y'} + a_{z'} \end{aligned} \tag{31}$$

The terms $\phi_y a_{x'}$ and $-\phi_r a_{z'}$ that couple into a_y can become significant; they are the reason that the along-track and vertical accelerometer measurements must be made. For instance, if ϕ_y or ϕ_p equals 2°, then from Table 2 an aircraft acceleration of 4 fps^2 produces a 4 mg error in (31); this error introduced into (27) results in a doppler error slope of almost 5 Hz/sec which considerably

exceeds that allowed by the performance requirement. Eqn (31) also shows that some means of measuring ϕ_y must be provided. This angle is equal to the difference between the aircraft velocity vector and the antenna axis. It can reach $\pm$ 3°. The measurement of this parameter can be provided by the aircraft doppler navigator and the existing yaw stabilization circuitry.

Also, note from Figure 3 that the measured values of acceleration in each of the primed axis includes a gravity component. These components are given by

$$\begin{aligned} a_{x'} &= A_{x'} - g \cdot \sin \phi_p \\ a_{y'} &= A_{y'} + g \cdot \cos \phi_p \cdot \sin \phi_r \\ a_{z'} &= A_{z'} + g \cdot \cos \phi_p \cdot \cos \phi_r \end{aligned} \tag{32}$$

where A' denotes the actual accelerometer measurement and g is the local value of gravity. It is assumed that g can be readily obtained from other measured parameters such as heading, latitude, altitude, speed, etc. Invoking the small angle approximation allows the following simplified expressions:

$$\begin{aligned} a_{x'} &= A_{x'} - g\,\phi_p \\ a_{y'} &= A_{y'} + g \cdot \phi r \\ a_{z'} &= A_{z'} + g\left(1 - \frac{\phi_p^2 + \phi_r^2}{2}\right) \end{aligned} \tag{33}$$

The last of (33) has an error of 2.7 mg if the quadratic term $\frac{\phi_p^2 + \phi_r^2}{2}$ is dropped and both angles have a value of 3°. However, the error when coupled into the cross-track direction via (31), is negligible even for relatively large angles, so this term can be dropped.

The motion compensation procedure thus proceeds as follows: beginning with the accelerometer measurements, A', the gravity correction (33) is applied. Then, knowing the yaw, pitch, and roll angles, equ (31) can be evaluated. These corrected accelerations, a, are then integrated to give the velocity components along the inertial axis. Then, referring to Figure 9 below, with regard to some point P, indicated by the clutter lock circuitry,

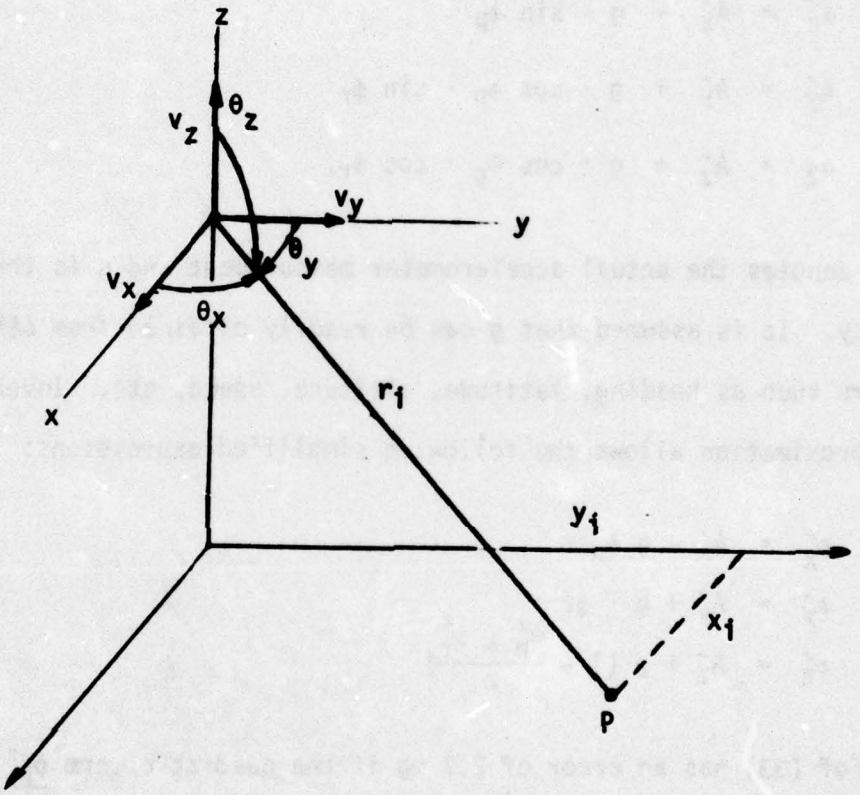

Figure A-9. Geometry between sensors and ground point with coordinates x_i, y_i.

the range rate correction becomes

$$\dot{r}_c = v_x \cos \theta_x + v_y \cos \theta_y + v_z \cos \theta_z \qquad (34)$$

where the direction cosines are given by $\cos \sigma_x = x_i/r_i$, $\cos \sigma_y = y_i/r_i$, and $\cos \sigma_z = -z_0/r_i$; approximations to $\cos \sigma_y$ and $\cos \sigma_z$ are implemented in the processor. The ratio x_i/r_i can be determined from the clutter lock measurement: for long smoothing times, $\dot{r} \approx x\dot{x}/r$, because $\dot{y}$ and $\dot{z}$ are nearly zero. Using the doppler relationship obtains $x/r = \lambda f_d/2\dot{x}$, for which all parameters are known. The correction thus becomes

$$\dot{r}_c = \left(\frac{\lambda f_d}{2x}\right) v_x + v_y \cos \theta y + v_z \cos \theta_z \qquad (35)$$

It is likely that other approximations to the direction cosines can be implemented as well.

APPENDIX 1

The value of the parameters are taken from the body of the report.

$(d_x + \dot{x}t - x_i)\overset{0}{d_x}$ = (1 + 300 · 1/2 - 1430) .016 = 23.

$(\phi_y \Delta_y' \dot{x} + d_{xm}\varepsilon_{\dot{x}}$ = (.017 · 1/3 · 300 + 1 · .08) = 2.

$(2\dot{x}\varepsilon_{\dot{x}} + \varepsilon_{\dot{x}}^2)t$ = (2 · 300 · .08 + -)1/2 = 24.

$x_i\varepsilon_{\dot{x}}$ = 1430 · .08 = 114.

$(d_y + \dot{y}t - y_i)\dot{dy}$ = (1/3 + 3 · 1/2 - 163,695) .052 = .8512

$(\phi_y \Delta x' \dot{y} - d_{ym}\varepsilon\dot{y})$ = (.017 · 1 · 3 - 1/3 · .08) = .02

$(2\dot{y}\varepsilon\dot{y}^2 + \varepsilon\dot{y}^2)t$ = (2 · 3 · .08 + .08²)1/2 = .097

$Y_i\varepsilon\dot{y}$ = 163,695 · .08 = 13,096.

$(d_z + \dot{z}t + z_0)d_z$ = (1 + 3 · 1/2 + 10,000) .024 = 240.

$d_{zm}\,\varepsilon\dot{z}$ = 1 · .08 = .08

$(2\dot{z}\varepsilon_{\dot{z}} + \varepsilon_{\dot{z}}^2)t$ = (2 · 3 · .08 + .08) 1/2 = .02

$(\sigma_z\dot{z} + z_0\varepsilon_{\dot{z}} + \varepsilon_z\varepsilon_{\dot{z}})$ = (100 · 3 + 10,000 · .08 + 100 · .08 = 1,108.

APPENDIX 2

$(\dot{d}_x + \dot{x})^2$	$= (.016 + 300)^2$	$= 9 \times 10^4$
$(\dot{d}y + \dot{y})^2$	$= (.052 + 3)^2$	$= 9.3$
$(\dot{d}_z + \dot{z})^2$	$= (.024 + 3)^2$	$= 9.1$
$\dot{r} = v^2 t/r$	$= 300^2 \cdot 1/2/164{,}000$	$= .27$

$\ddot{d}_x \approx \ddot{\phi}_p \Delta_z'$	$= .031 \cdot 1$	$= .031$
$\ddot{d}_y \approx -\ddot{\phi}_r \Delta_z'$	$= .151 \cdot 1$	$= .151$
$\ddot{d}_z \approx -\ddot{\phi}_p \Delta x' + \ddot{\phi}_r \Delta_y'$	$= .031 \cdot 1 + .151 \cdot 1/3$	$= .059$ (RSS)

$(d_x + \dot{x}t - x_i)$	$= (1 + 300 \cdot 1/2 - 1{,}430)$	$= 1{,}279$
$(d_y + \dot{y}t - y_i)$	$= (1/3 + 3 \cdot 1/2 - 163{,}695)$	$= 163{,}693$
$(d_z + \dot{z}t + z_o)$	$= (1 + 3 \cdot 1/2 + 10{,}000)$	$= 10{,}003$

APPENDIX 3

$\dot{d}_x^2$		$.016^2$	2.6×10^{-4}
$2\,\dot{d}_x\dot{x}$		$2 \cdot .016 \cdot 300$	9.6
(y) $\ddot{d}_y$		$163{,}693 \cdot .151$	24,718
(z) $\ddot{d}_z$		$10{,}003 \cdot .059$	590
$2x\dot{\varepsilon}_x + \dot{\varepsilon}_x^2$		$2 \cdot 300 \cdot 3 + 9$	1,809
(y) $\ddot{\varepsilon}_y$		$163{,}693 \cdot .0644$	10,542 (2 mg)
(z) $\ddot{\varepsilon}_z$	=	$10{,}003 \cdot .0644$	644 (2 mg)

REFERENCES

1. R.W. Sanneman, "Studies of Position-Acceleration Combinations - Phase III," Final Report, ESP 520-13, 17 July, 1974.

2. Goodyear Aerospace, "Development of an Advanced Radar Sensor," Radar Set AN/UPD-3, Part A, 2 April 1965, A.D. 358 543.

3. A. Papoulis, "Probability, Random Variables, and Stochastic Processes," McGraw-Hill, 1965.

APPENDIX B

MAXIMUM RANGE CALCULATIONS

B-1. SEA SURFACE RETURN, SYNTHETIC ARRAY RADAR

Sufficient sea return must be imaged on the film so that the reduction of sea return caused by surface oil will be detectable. The following calculations provide a useful frame of reference for comparing test results, but should be used with some caution. The backscatter coefficient of the sea surface was estimated using observed weather conditions and the tables from Nathanson,[1] the applicable parts of which are reproduced in table B-1. Actual detection of oil on the film also depends on the extent of the oil and the resolution of the radar.

The equation used was:

$$R^4 = \frac{P_P G_A^2 \lambda^2 \sigma G_P}{(S/N)(4\pi)^3 KT_0 B NFL} \qquad \text{(B-1)}$$

For the synthetic array radar, the clutter cross section is given by

$$\sigma = (\sqrt{\lambda R})\left(\frac{C\tau}{2}\right)\sigma_{0V} \qquad \text{(B-2)}$$

where

$\lambda = 0.03$ meter

$\left(\frac{C\tau}{2}\right) = 30$ meters

σ_{0V} = backscatter coefficient at 3 degree depression angle

R = range in meters

P_P = peak transmitter power = 47 dBw

G_A = antenna gain at 3 degree depression angle = 33.5 dB

---

[1] Radar Design Principles, F. E. Nathanson, McGraw Hill, 1969, pp. 235, 236.

Table B-1. Backscatter Coefficient (Negative dB)

Sea State	0		1		2		3	
Polarization / Depression Angles	H	V	H	V	H	V	H	V
1°	66	60	51	50	46	44	40	39
3°	58	56	48	45	42	41	39	38
10°	56	49	51	42	43	36	37	32

G_P = processing gain = 14 dB for over-water made

= 20 dB for overland 1 look mode

= 22.5 dB for over-land 3 look mode

S/N = signal to noise required for detection = 6 dB

KT_0 = -204 dB (watt/Hz)

NFL = receiver noise figure including losses = 13 dB

B = receiver noise bandwidth = 67 dB (1 Hz)

Using the values above, the maximum ranges shown in table B-2 were calculated.

Table B-2. SAR Sea Return Maximum Ranges (Kilometers)

Sea State	Mode		
	Over Water	Over Land - 1 Look	Over Land - 3 Look
1	14	20	23
2	18	25	29

B-2. SEA SURFACE RETURN, APS-94D

The equation used was:

$$R^4 = \frac{P_P G_A^2 \lambda^2 \sigma}{(4\pi)^3 \overline{MDS}}$$

In this case,

$$\sigma = \Delta\theta\left(\frac{C\tau}{2}\right)\sigma_{0H}$$

where

$\Delta\phi$ = antenna beamwidth = 0.008 radian

G_A = 36.5 dB at 3 degree depression angle

$\overline{MDS}$ = minimum detectable signal = -130 dBw

All other parameters are as defined for equation 6-2.

The calculated maximum ranges are:

R = 27 km for sea state 1

R = 38 km for sea state 2

B-3. POINT TARGET DETECTION, SYNTHETIC ARRAY RADAR

The same computational method as described in paragraph B-1 was used, except that:

σ = 5 square meters for calibrated target

= 40 square meters assumed for 41-foot utility boat

S/N = 15 dB

The ranges calculated are shown in table B-3.

Table B-3. SAR Point Target Maximum Ranges

Target	Mode		
	Over Water	Over Land - 1 Look	Over Land - 3 Look
5 sq. meter	33	47	54
41-ft. utility boat	55	78	90

B-4. POINT TARGET DETECTION, APS-94D

The same computational method as described in paragraph B-2 was used except that:

σ = 5 square meters for calibrated target

= 40 square meters assumed for 41-foot utility boat

$\overline{MDS}$ = -124 dBw (6 dB higher than for sea return)

The calculated maximum ranges are:

R = 42 km for 5 square meter target

R = 71 km for 41-ft utility boat

APPENDIX C

FLIGHT TEST PLAN

COR, SYNTHETIC APERTURE RADAR

20 March 1976

Prepared by: F Shacklock

F. Shacklock
Motorola Inc.

Approved by: Guy V Morris

G. V. Morris
Motorola Inc.

Approved by: _____

U. S. Coast Guard

Approved by: _____

U. S. Army

TABLE OF CONTENTS

ILLUSTRATIONS

1.0 INTRODUCTION

The purpose of the flight test program is to verify the performance of a coherent-on-receive, synthetic aperture radar designed by Motorola. The desired performance is in the over-water environment to satisfy U.S. Coast Guard requirements. Preliminary checkout flights and ground mapping flights will be made in the Phoenix and Ft. Huachuca areas prior to the over-water tests.

The designated Motorola Project Leader will be responsible for coordinating all aircraft accessibility, flight schedules, flight paths, duration of missions, etc., during all phases of the program.

The designated USCG representative will aid in coordination of all flight activities, targets, and providing ground truth for the over-water phase.

The pilot in command shall be responsible for all aspects of aircraft readiness, flight conditions, flight paths, etc., that relate to flight safety.

Requests for a flight will be made at least four hours prior to the desired take-off time when the aircraft and crew are in the Phoenix or West Coast areas. Two days notice will be given when the aircraft and/or crew is at Ft. Huachuca.

2.0 EQUIPMENT

The tests will require the use of the OSDR-94 Radar System modified to the COR configuration and a C-47 aircraft and crew. An OV-1D aircraft equipped with an APS-94D will be required for comparison imagery and photography. Also required will be aircraft instrumentation and certain controlled ground targets. The following equipment will be utilized as a minimum. Additional instrumentation and test equipment will be used as required:

System Components

Receiver/Transmitter
Video Processor
Electrical Equipment Rack
Sweep Generator
Radar Set Control
Radar Target Indicator
Radar Mapping Recorder-Processor-Viewer
Interconnecting Box
Antenna Assembly
COR Control Panel
Power Distribution Panel
Power Supplies
Film/Monobath Kits (as required)

Instrumentation and Test Equipment

Digital Tape Recorder
Oscilloscope
Logic State Analyzer
Digital-to-Analog Converters
Test Signal Generators (as required)

3.0 EQUIPMENT CHECKOUT FLIGHTS

The checkout flights will be conducted in the Phoenix area. Access to the aircraft on the ground will be required prior to and after each flight for ground checks. Access may also be required other days when no flights are planned for equipment testing. Prior to each flight, the Motorola Project Leader will discuss with the aircraft crew and USCG representative (if present), the purpose of the flight, desired altitudes, speeds, ground track, and flight duration.

It is anticipated that all checkout flights will be conducted in morning hours and be of one to two hours duration. Three to five flights per week is anticipated.

The Motorola Project Leader will be responsible for the recording of significant data and identification of imagery. The status of each of the major system elements (COR, Motion Compensation, Clutter Lock, Synthetic Aperture Filters and Display) will be informally reported on a weekly basis.

The U.S.Army project coordinator will be responsible for all aspects of aircraft logistics and will informally report weekly on percent of budget remaining or equivalent flight hours remaining.

Recordings of aircraft motion and imagery with antenna yaw stabilization disabled will be accomplished during this phase of the program.

4.0 GROUND MAPPING FLIGHTS

Ground mapping will be conducted in the Ft. Huachuca area using the Radar Resolution Facility to determine system resolution, detectable range for a known target cross section, and imagery geometric fidelity. A minimum of one week advance notice will be given to the Army representative to prepare the ground targets. The flights will be conducted in accordance with the pattern shown in Figure 1. The layout of the Radar Facility will be as shown in Table 1. Modification to the patterns, if necessary, will be made with the concurrence of the on-site Coast Guard, Army and Motorola representatives. The anticipated schedule and equivalent flight hours for this phase of the program are shown in Section 6 of this plan.

Run	Distance From Trgt	Range Setting	Delay	Mode	Mover Velocity
1	10 km	25 km	0	1 look	4 M
2	10	25	0	over water	4
3	20	25	0	1 look	.5
4	20	25	0	over water	.5
5	40	25	20	1 look	1.5
6	40	25	20	2 look	1.5
7	40	25	20	3 look	1.5
8	80	50	40	2 look	N.A.

Flt Altitude - 9,000 ft. MSL

Ground Speed - 178 Kts min.

Flt Duration - 2.5 Hrs (Approx.)

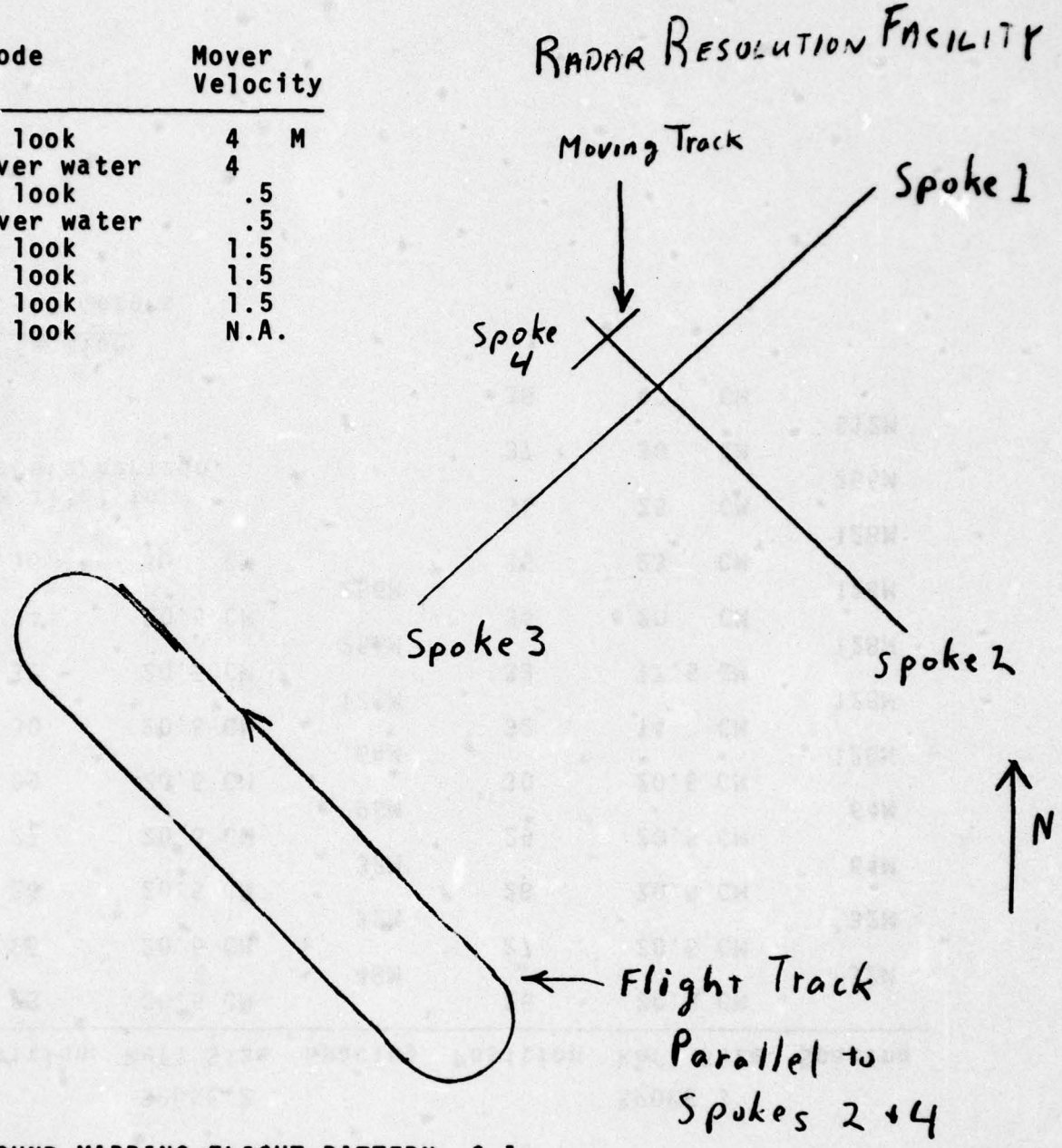

GROUND MAPPING FLIGHT PATTERN, G-1

FIGURE 1

RADAR SPOKE CONFIGURATION

TABLE 1

SPOKE 1			SPOKE 2			SPOKE 3		
Position	Refl Size	Spacing	Position	Refl Size	Spacing	Position	Refl Size	Spacing
23	20.5 CM	48M	23	20.5 CM	48M	26	20.5 CM	32M
25	20.5 CM	608M	25	20.5 CM	32M	27	20.5 CM	32M
34	40 CM		26	20.5 CM	32M	28	20.5 CM	64M
			27	20.5 CM	96M	29	20.5 CM	64M
			29	20.5 CM	64M	30	20.5 CM	128M
			30	20.5 CM	128M	32	14 CM	128M
			32	20.5 CM	256M	33	17.5 CM	128M
			34	20.5 CM	256M	34	20 CM	128M
			36	40 CM		35	23 CM	128M
						36	25 CM	256M
						37	30 CM	512M
						38	40 CM	

NOTE: All reflectors directed parallel to Spoke 3 toward Southwest and 5° above horizon.
MTI Track - 25 cm reflector size

Reflector Size	Radar Cross Section
14 cm	1.8 sq. meters
17.5	4.4
20	7.5
20.5	8.5
23	13
25	19
30	40
40	120

5. OVER-WATER MAPPING

The over-water mapping flights will be conducted operating from Pt Mugu and San Francisco air stations. The flights will be conducted according to the schedule shown in Section 6 of this plan. Flight patterns W-1 thru W-6 have been designed to satisfy the program objectives established by the U.S.Coast Guard. Additional flight patterns or modification of the established patterns may be made by the mission director with concurrence of the on-board Coast Guard and Army representatives. The objectives of each of the over-water flight patterns is summarized below:

Pattern W-1	Determine best operating altitude, map calm sea.
Pattern W-2	Map fixed targets in low sea state, compare over-water to land modes.
Pattern W-3	Map moving targets and slicks in low sea state, map land sea boundry.
Pattern W-4	Observe different clutter lock modes.
Pattern W-5	Map fixed targets in strong current.
Pattern W-6	Map moving target and slick in higher sea state, map land sea boundry.

OBJECTIVE - Determine Optimum Operating Altitude, Calm Sea Mapping

RADAR SETTINGS - 25 km Range, 20 km Delay Over-Water Mode

FLIGHT DURATION - 1.5 Hours

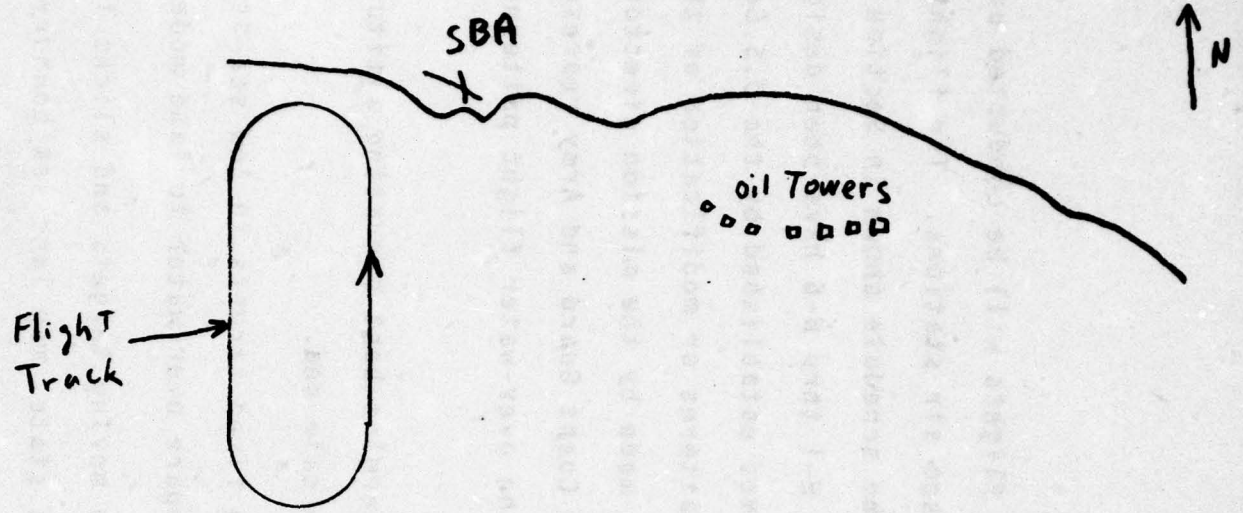

RUN	ALTITUDE MSL	
1	3,000 ft.	
2	5,000 ft.	
3	7,000 ft.	
4	9,000 ft.	C-47 Only

FLIGHT PATTERN W-1

FIGURE 2

OBJECTIVE - Mapping Fixed Targets In Water

RADAR RANGE SETTING - 25 km, Altitude - TBD

FLIGHT DURATION - 2.5 Hours

Run	Distance From Judith	Delay	Mode
1	20 km	0	Over water
2	20 km	0	Over water
3	20 km	0	Over water
4	20 km	0	Over water
5	20 km	0	1 look
6	20 km	0	1 look
7	20 km	0	1 look
8	20 km	0	1 look
9	30 km	20	Over water
10	30 km	20	Over water
11	40 km	20	Over water
12	40 km	20	Over water

Distance from Judith for Runs 9-12 may be adjusted based on Runs 1-8

Runs 11, 12 optional based on elapsed flight time.

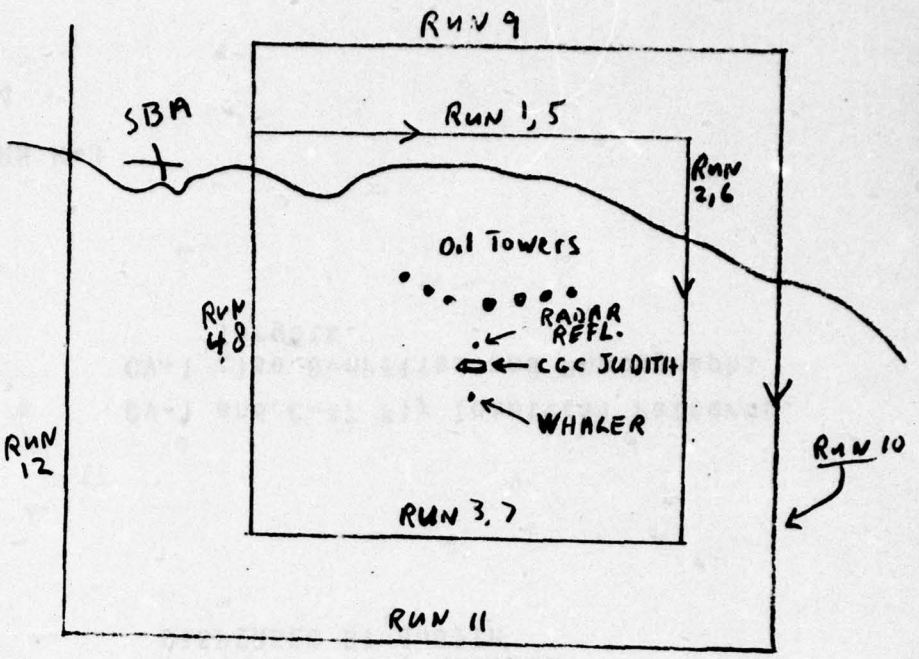

OV-1 and C-47 fly identical patterns.

OV-1 also overflies and photographs targets.

FLIGHT PATTERN W-2

FIGURE 3

OBJECTIVE - Map Moving Ship and Slick in Low Sea State

RADAR RANGE SETTING - 25 km, Over Water Mode

FLIGHT DURATION - 2.0 Hours Altitude - TBD

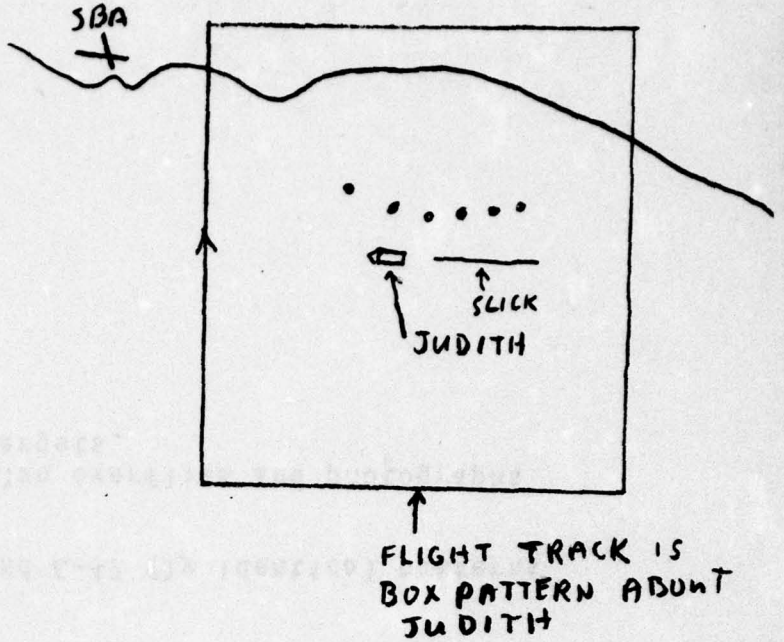

SLICK OF OLEYL ALCOHOL DISPERSED BY JUDITH

Box Pattern Number	Distance From Judith	Radar Delay
1	20 km	0
2	30 km	20

Distance from Judith may be adjusted based on sea conditions and radar return.

OV-1 and C-47 Fly Identical Patterns.

OV-1 also Overflies and Photographs Targets.

FLIGHT PATTERN W-3

FIGURE 4

OBJECTIVE - Observe Different Clutter Modes

RADAR RANGE - 25 km, Delay 0 Altitude - TBD

FLIGHT DURATION - 1.0 Hours

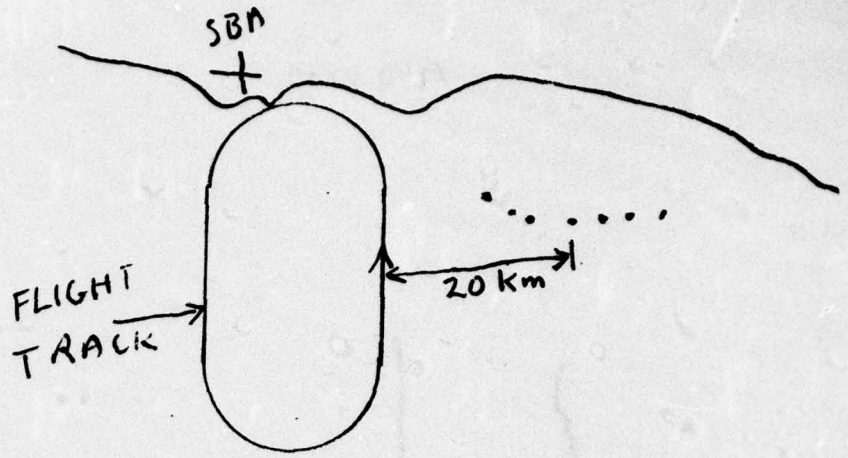

Run	Mode
1	Over Water
2	Ins/No Clutterlock
3	Normal Clutterlock

C-47 Only

FLIGHT PATTERN W-4

FIGURE 5

OBJECTIVE - Over Water Map with Strong Tide and Buoys

RANGE FROM BUOYS - 10 km Altitude - TBD

RADAR RANGE SETTING - 25 km, 0 Delay.

FLIGHT TIME - 1.0 Hour

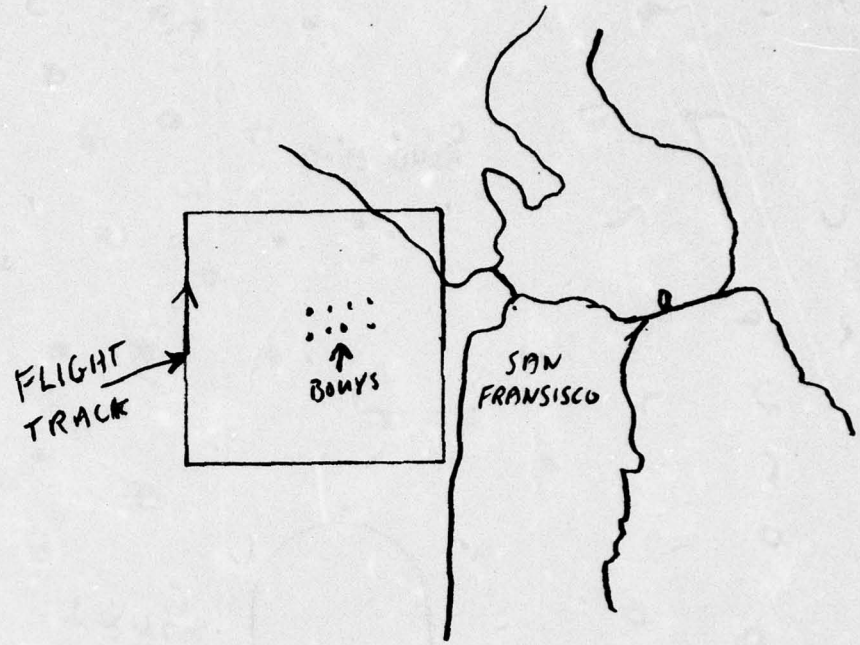

Box Pattern Number	Mode
1	Over Water
2	1 Look

Additional Box Patterns may be flown at discretion of Mission Director.

C-47 Only

FLIGHT PATTERN W-5

FIGURE 6

OBJECTIVE - Map Higher Sea States, Moving Ship,
Oil Slicks and Land Sea Boundry.

RADAR SETTING - 25 km Delay-As Required Alt.-TBD

RADAR MODES - Over Water, 1, 2 and 3 look

C-47 Only

The Over-Water Mode will be selected while passing the CGC Hedge.

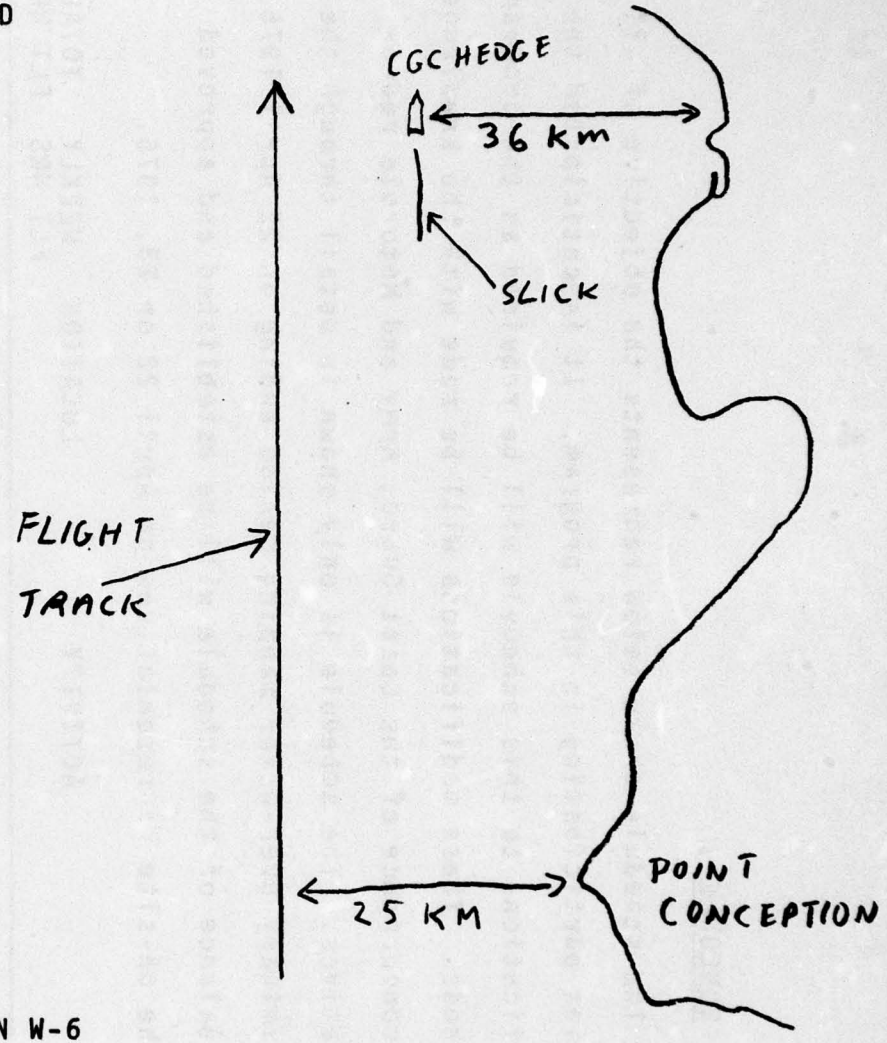

FLIGHT PATTERN W-6

FIGURE 7

6.0 SCHEDULE

The schedule shown below represents the objective of all parties participating in this program. It is anticipated the modifications to this schedule will be required as the program proceeds. These modifications will be made with the knowledge and concurrence of the Coast Guard, Army and Motorola representatives. The schedule is only shown in detail through the preliminary over-water mapping period ending on 22 April 1976. The balance of the schedule will be established and approved by the on-site representatives on April 22 or 23, 1976.

DATE	ACTIVITY	LOCATION	WEEKLY FLT HRS	TOTAL FLT HRS
3/15-3/22	Install Radar	Phoenix	5	5
3/23-3/26	Check Out	Phoenix	7	12
3/29-4/02	Check Out	Phoenix	8	20
4/05-4/09	Check Out	Phoenix	10	30
4/12	Program Review	Phoenix		
4/13	Ferry to Ft. Huachuca	to Ft. Hua.	2	32
4/14	Preliminary Ground Map 1 Flight Pattern G-1	Ft. Hua.	3	35
4/15	Ground Mapping 1 Flight Pattern G-1	Ft. Hua.	3	38
4/19	Ferry to Pt Mugu	Pt Mugu	4	42
4/20-4/22	Preliminary Over-Water Map*	Pt Mugu		
	Flight 1 Pattern W-1	Pt Mugu	2	44
	Pattern W-2 Runs 1,2,7,8 only		1	45
	Flight 2 Pattern W-3	Pt Mugu	2	47
	Pattern W-4		1	48

SCHEDULE (Continued)

DATE	ACTIVITY	LOCATION	WEEKLY FLT HRS.	TOTAL FLT HRS.
4/23-4/30	TBD based on equipment - operating condition			
5/3-5/30	Over-water Mapping Patterns W-1 thru W-6 with C-47 & OV-1D	Pt Mugu and San Francisco		

* OV-1D not required 4/20 - 4/22.

APPENDIX D

FLIGHT TEST DATA

DATE 5-19-76

COR SYNTHETIC APERTURE FLIGHT TEST

PREVAILING WIND 220, 10 kts FLIGHT NO. 2 O.W. TAKEOFF - 2:40

AIR TURBULENCE Light LAND - 5:15

Start Time	Run No.	Hdg	G.S./D.A.	Location	Alt	Range	Radar Parameters Delay	Looks	Comments
1455	0	273	2°L	Santa Barb	5500	25	0	O.W.	Pt. Mugu to station
1512	1	351	155/2°L	Santa Barb	5500	25	0	O.W.	00, Log (wrong ground speed - 240 kts).
	2	093	162/2°L	Santa Barb	5500	25	0	O.W.	00, Log
	3	185	1°L	Santa Barb	5500	25	0	1L	Land mode, Log, 01
	4	269	158/1°L	Santa Barb	5500	25	0	1L	Land mode, Log, 10
1555	5	351	3°L	Santa Barb	5500	25	0	O.W.	Preceded by long orbit Log, 00, Judith dropping oil.
1603	6	093		Santa Barb	5500	25	0	O.W.	Holly steaming - oil
1612	7	178	152/3°L	Santa Barb	5500	25	0	1L	Land 10 at start switch to 01
1621	8	270°							Land mode.
1630	9	360	152			25	20	3 Look	Land mode.

DATE 5-21-76

COR SYNTHETIC APERTURE FLIGHT TEST

PREVAILING WIND Calm to 5 Kts from N.W., 1 ft. swells FLIGHT NO. 3 O.W. TAKEOFF - 8:50

AIR TURBULENCE Light LAND -12:30

Start Time	Run No.	Hdg	G.S./D.A.	Location	Alt	Range	Radar Parameters Delay	Looks	Comments
0901	1	12°	/1°R	Pt. Mugu	5500	25	0	O.W.	Log, No AGC, 01 A to B
0909	2	214°	153°/0°	Pt. Mugu	5500	25	20	O.W.	Log, No AGC, 01 B to C
0916	3	33	0°	Pt. Mugu	5500	25	0	O.W.	Log, No AGC, 01 C to D
0924	4	216	153/0	Pt. Mugu	5500	25	20	O.W.	Log, No AGC, 01 D to E
0935	5	033	153/1°L	Pt. Mugu	5500	25	20	O.W.	Log, No AGC, 00 E to F
0940	6	235	153/0.5°R	Pt. Mugu	5500	25	0	O.W.	Log, No AGC, 00 F to G
0948/956	7	34	155/0°	Pt. Mugu	5500	25	40	O.W.	Log, No AGC, 00 G to H (20 delay at start)
	8					25	0	O.W.	Up coast to Morro Bay 01, Line Switched to AGC at 1002 switched to Log, 00
1100/1105	9	/3°R		Morro Bay	5500	25	0	O.W.	Cape Hedge A to B
1107/1111	10	095	150/1°R	Morro Bay	5500	25	0	O.W.	B to C
1112	11	180	153/3°	Morro Bay	5500	25	0	1L	C to D

DATE 5-21-76

FLIGHT NO. 3 O.W. (Cont.)

Start Time	Run No.	Hdg	G.S./D.A.	Location	Alt	Range	Radar Parameters Delay	Looks	Comments
1120/1128	12	271	163/2°	Morro Bay	5500	25	0	1L	D to X
1130	13	050	154/3°R	Morro Bay	5500	25	20	O.W.	X to G
11:48/1153	14	176	148/5°L	Morro Bay	5500	25	0	O.W.	Xmit off after run for X C to D
11:55/11:58	15	274	165/4°L	Morro Bay	5500	25	0	O.W.	D to E
12:00/1204	16	002	165/3°R	Morro Bay	5500	25	0	O.W.	E to F
1208/1213	17	175	148/5°L	Morro Bay	5500	25	0	O.W.	With oil slick (steaming 270° wind 4 kts.)

APPENDIX E

SAMPLE RADAR IMAGERY AND PHOTOGRAPHS

Figure E-1: AN/APS-94D and COR comparative imagery showing the same area in the Phoenix area. The AN/APS-94D imagery was taken during a system sell-off flight and flown in a U.S. Army Mohawk. The COR imagery was taken in the 40 km land mode with a single look. Careful examination of the two images at long range shows additional features visible on the COR image due to the improved azimuth resolution.

Figure E-2: COR imagery showing the effects of multiple looks. The left hand inch is with a single look while the rest is with three looks. The range scale is 25 km with 20 km delay. Note the additional terrain features visible with the multiple looks. The road that is clearly visible with multiple looks is not visible with the single look mode. Imagery was taken at an altitude of approximately 6000 feet mean sea level (MSL).

Figure E-3: Three-look COR imagery of the Phoenix area. The range scale is 25 km with 40 km delay. The altitude was approximately 6000 feet MSL. The power line shows the COR resolution improvement and the proper registration of the multiple looks. The azimuth spot width of these targets measures 65 meters at a range of 50 km.

Figure E-4: COR imagery showing the effects of antenna yaw stabilization. The right hand half of image was takn with the yaw stabilization disabled. The range scale is 25 km and the altitude was 6000 feet MSL. The flight conditions were moderately turbulent.

Figure E-5: COR imagery of Santa Barbara taken 19 May 1976 showing the four natural oil seeps detected during the flight test program. The imagery also shows the 5 m^2 Radar Reflector. The imagery was taken in the COR over-water mode with the 25 km range scale. The aircraft heading was 273° and altitude was 5500 feet. The imagery is distorted by the fact the film speed was set 1.6 times too fast due to operator error.

Figure E-6: AN/APS-94D comparative imagery to E-5. The imagery was taken at about the same time as the COR image. The altitude was approximately 2500 feet.

Figure E-7: COR imagery of Runs 2 and 3 from the 19 May mission. Run 2 was taken with the COR over-water mode and run 3 with the land mode. The range scale was 25 km for both runs and the altitude was 5500 feet. Run 2 shows the U.S. Cutter "Pt. Judith" and 5 m^2 Radar Reflector used in the tests. Both runs show the natural oil seeps.

Figure E-8: AN/APS-94D comparative imagery to E-7.

Figure E-9: COR imagery of runs 6 and 7 from the 19 May mission. Run 6 was taken with the COR over-water mode and run 7 with the land mode. The range scale was 25 km for both runs and the altitude was 5500 feet. Both runs show the synthetic oil slick as well as the natural oil seeps.

Figure E-10: AN/APS-94D comparative imagery to E-9. The altitude was 6500 feet. The synthetic oil slick is clearly visible on run 7 but not on run 6. Note the good sea clutter return in both runs. Both runs were made with the radar looking upwind (wind from 220°).

Figure E-11: COR imagery of runs 8 and 9 from the 19 May mission. Run 8 was taken with the COR land mode, 25 km range scale, 0 delay, with one (1) look, and at an altitude of 5500 feet. Run 9 was taken with the land mode, 25 km range scale, 20 km delay, with three (3) looks, and at an altitude of 5500 feet. Both runs were made with the radar looking downwind. Note that the synthetic oil slick is clearly visible on both runs.

Figure E-12: AN/APS-94D comparative imagery to E-11. Run 8 was with a range scale of 25 km and run 9 with the 50 km range scale. The altitude for both runs was 6500 feet. Both runs were made with the radar looking downwind. Note the much weaker sea clutter return in these two runs compared to the imagery shown in Figure E-10 when looking upwind.

Figure E-13: COR imagery of runs 3 and 4 of the 21 May mission. Both runs were made with the COR overwater mode at an altitude of 5500 feet. Run 3 is with the 25 km range scale at 0 delay and run 4 with the 25 km range scale and 20 km delay. The breakwater shown in run 3 shows the effects of azimuth sidelobes. A sharp image is formed of the breakwater with the adjacent fill-in caused by the sidelobes to the full real aperture beam-width. The point targets shown in run 4 show the effects of azimuth sidelobes and multiple printing. One target shows two distinct dots while the second target shows three distinct dots.

Figure E-14: COR imagery of runs 16 and 17 from the 21 May, Morro Bay mission. Both runs were taken with the COR over-water mode, 25 km range scale, and at an altitude of 5500 feet. Note the U.S. Coast Guard cutter "Cape Hedge" and the snythetic oil slick.

Figure E-15: OSDR imagery of the Santa Barbara area taken July 31, 1974. This imagery was made on a previous program using the OSDR, prior to the COR modification.

Figure E-16: Photograph showing the two small synthetic slicks generated off Santa Barbara for the 19 May mission. These slicks were not detected with either system since the slick size was about equal to the radars resolution cell. The photograph does show the sea state for the 19 May tests.

Figure E-17: Photograph of the $5m^2$ Radar Reflector deployed in the target area.

Figure E-18: Photograph taken from the U.S. Coast Guard cutter "Pt Judith" showing the sea state and synthetic oil slick being generated in its wake. The object in the background is the oil platform Holly.

Figure E-19: Photograph of the same synthetic slick shown in Figure C-18, except taken from the air.

STANDARD APS-94D
(50 KM RANGE, 0 DELAY)
16 FOOT ANTENNA

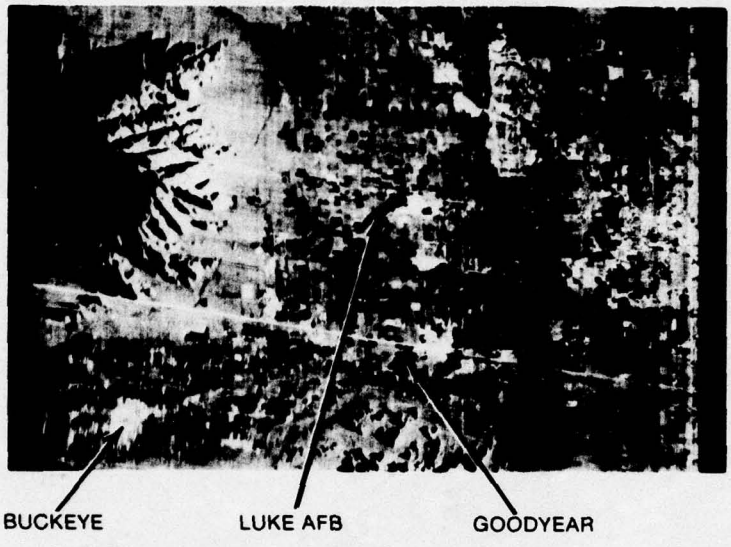

ROAD NOT VISIBLE ON APS94D

C-O-R SYNTHETIC APERTURE
(50 KM RANGE, 0 DELAY)
8 FOOT ANTENNA

76-3351

E-1.
COMPARATIVE IMAGERY
WEST PHOENIX

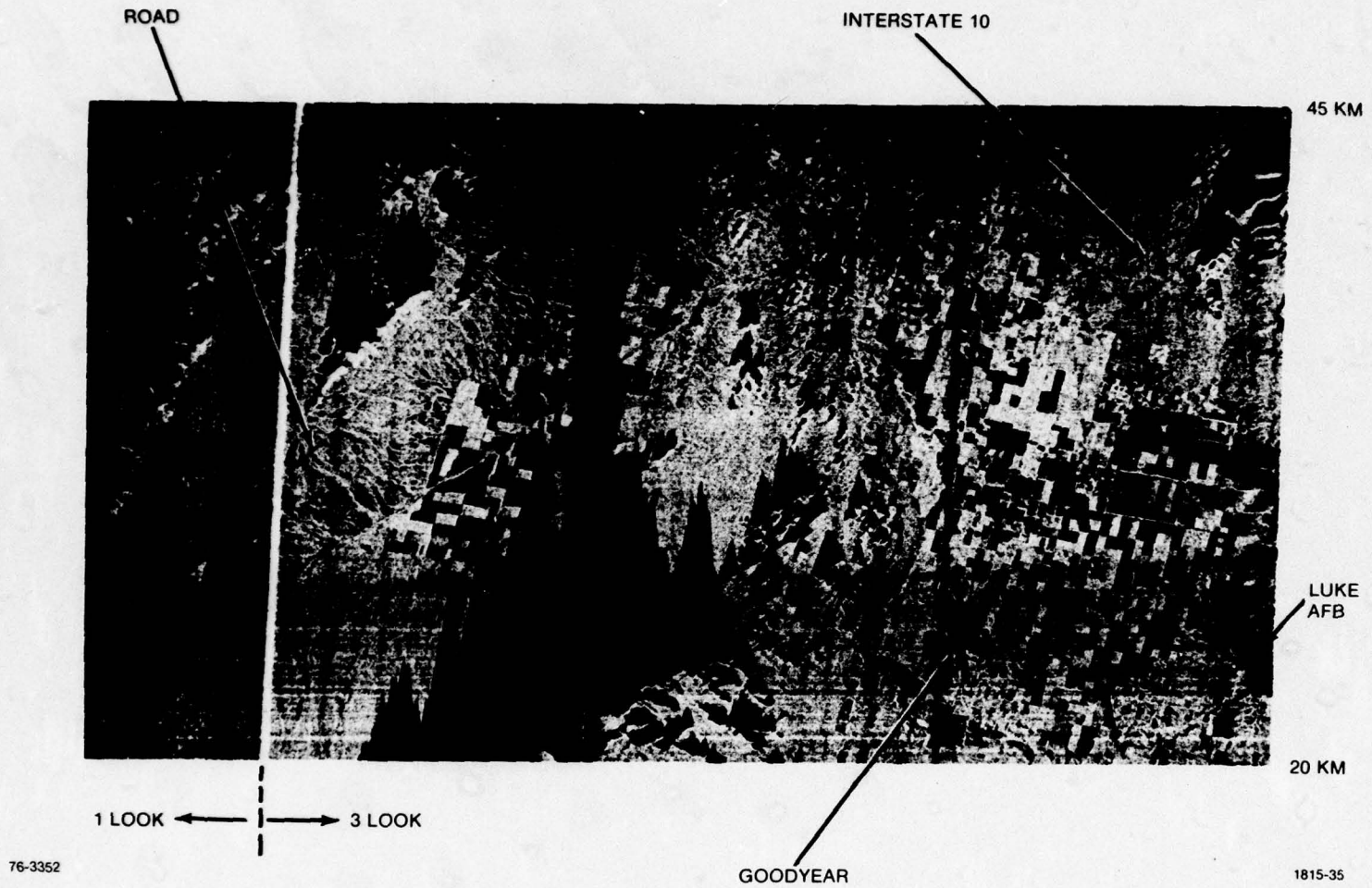

E-2. Effect of Multiple Looks

E-3. 40 to 65 Km Three Looks

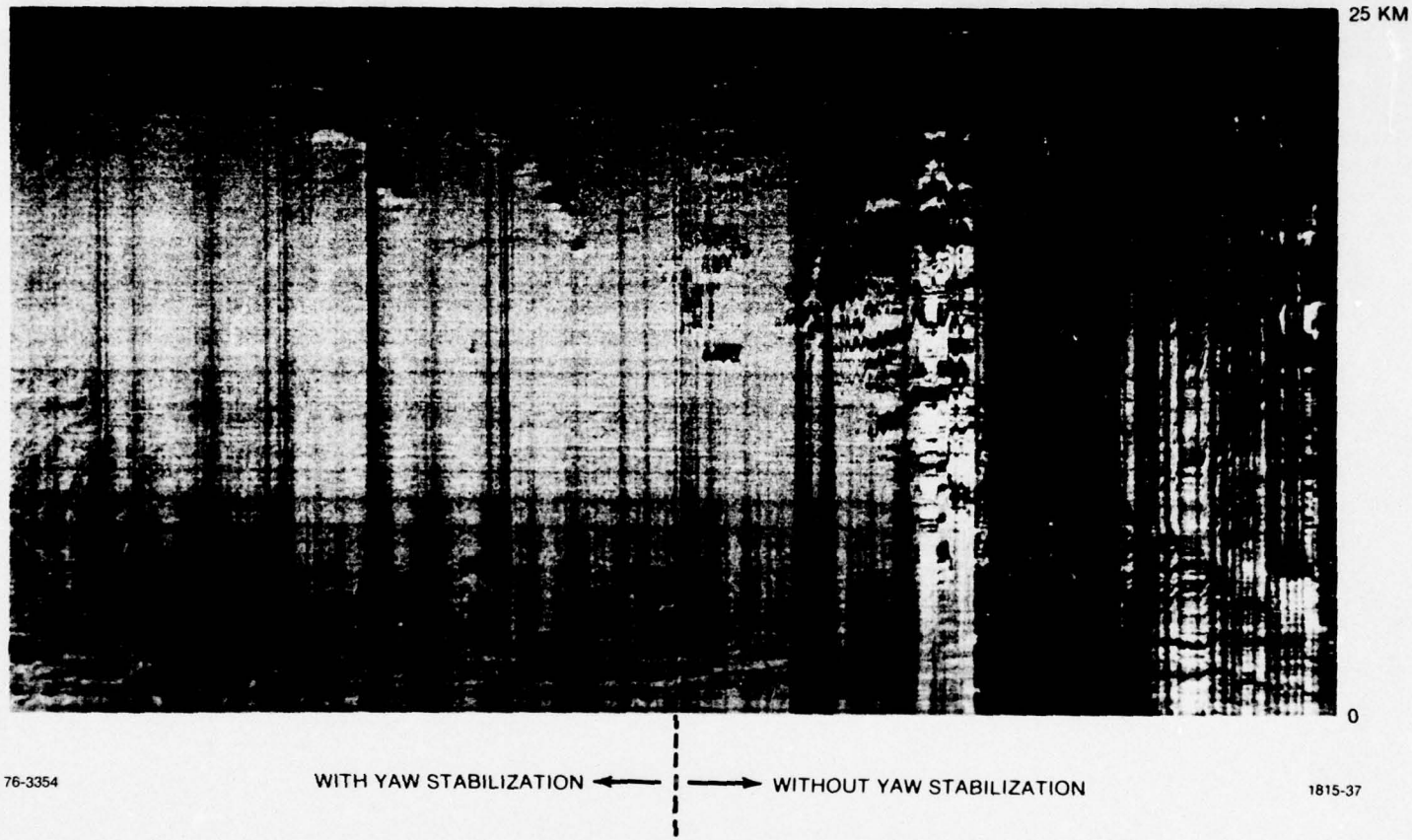

E-4. Effects of Yaw Stabilization

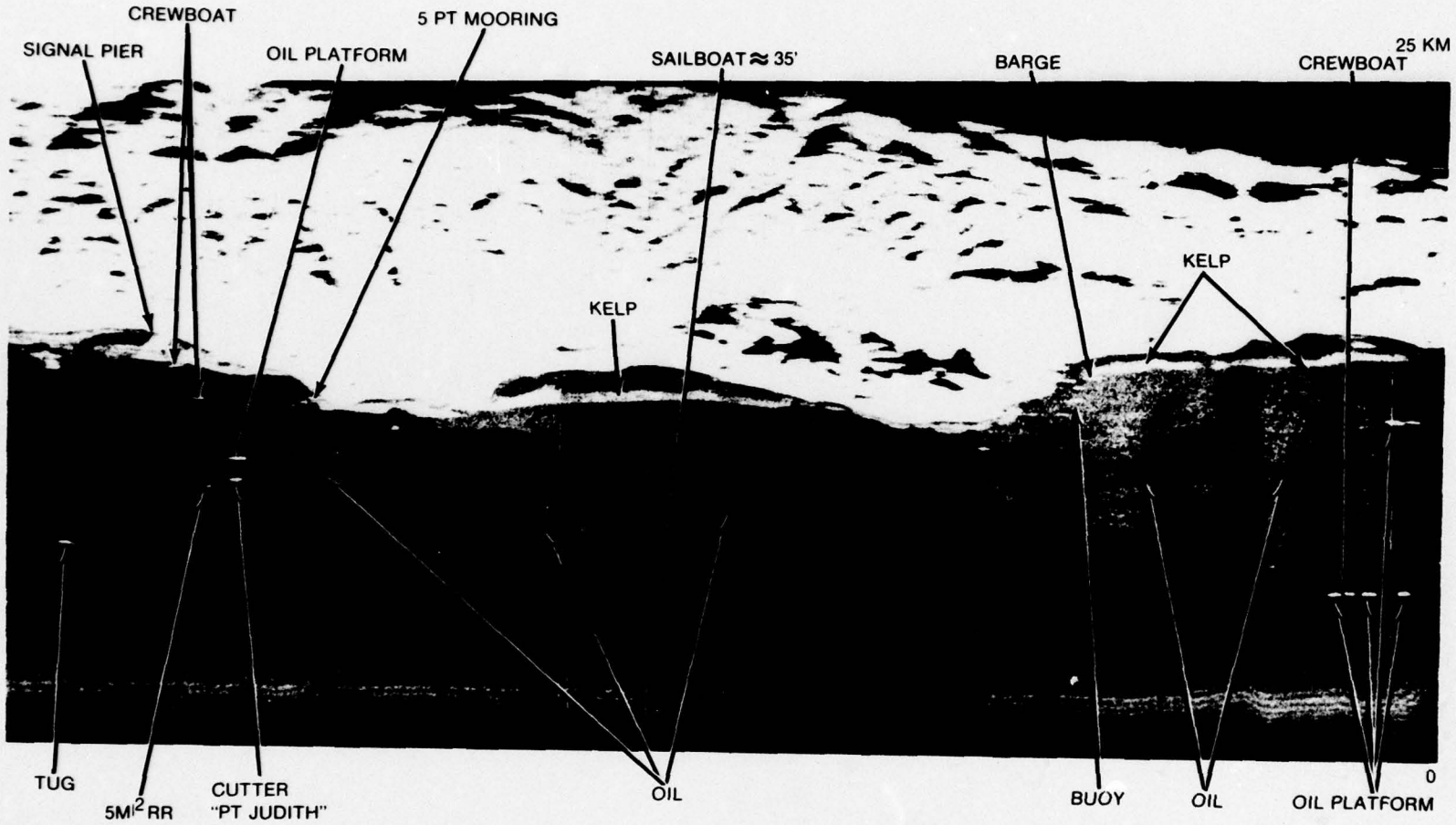

76-3355

OVERWATER MODE
ALT - 5500'
HEADING - 273°

1815-41

E-5. COR, Santa Barbara, 5/19

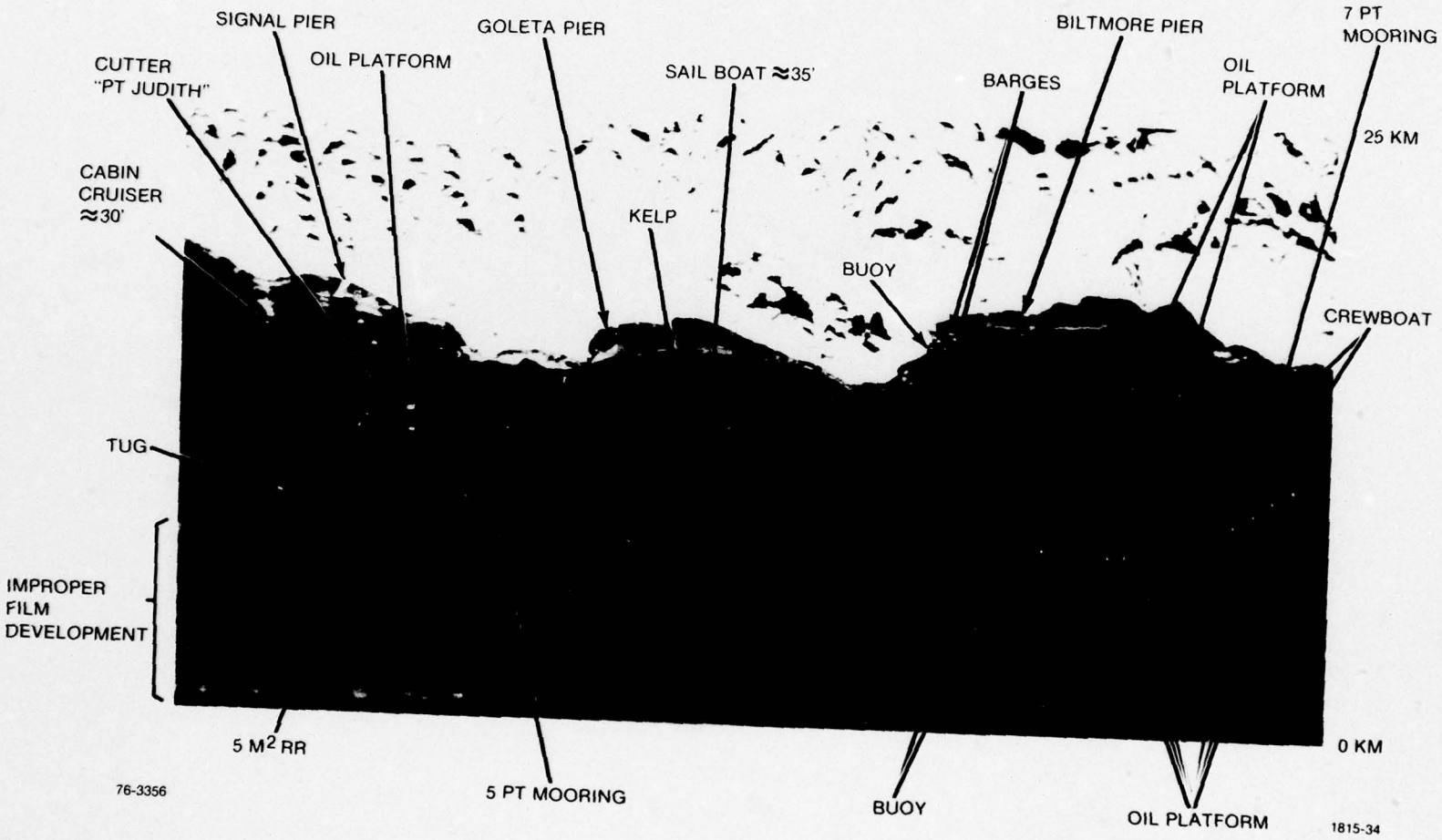

E-6. AN/APS-94D, Santa Barabara

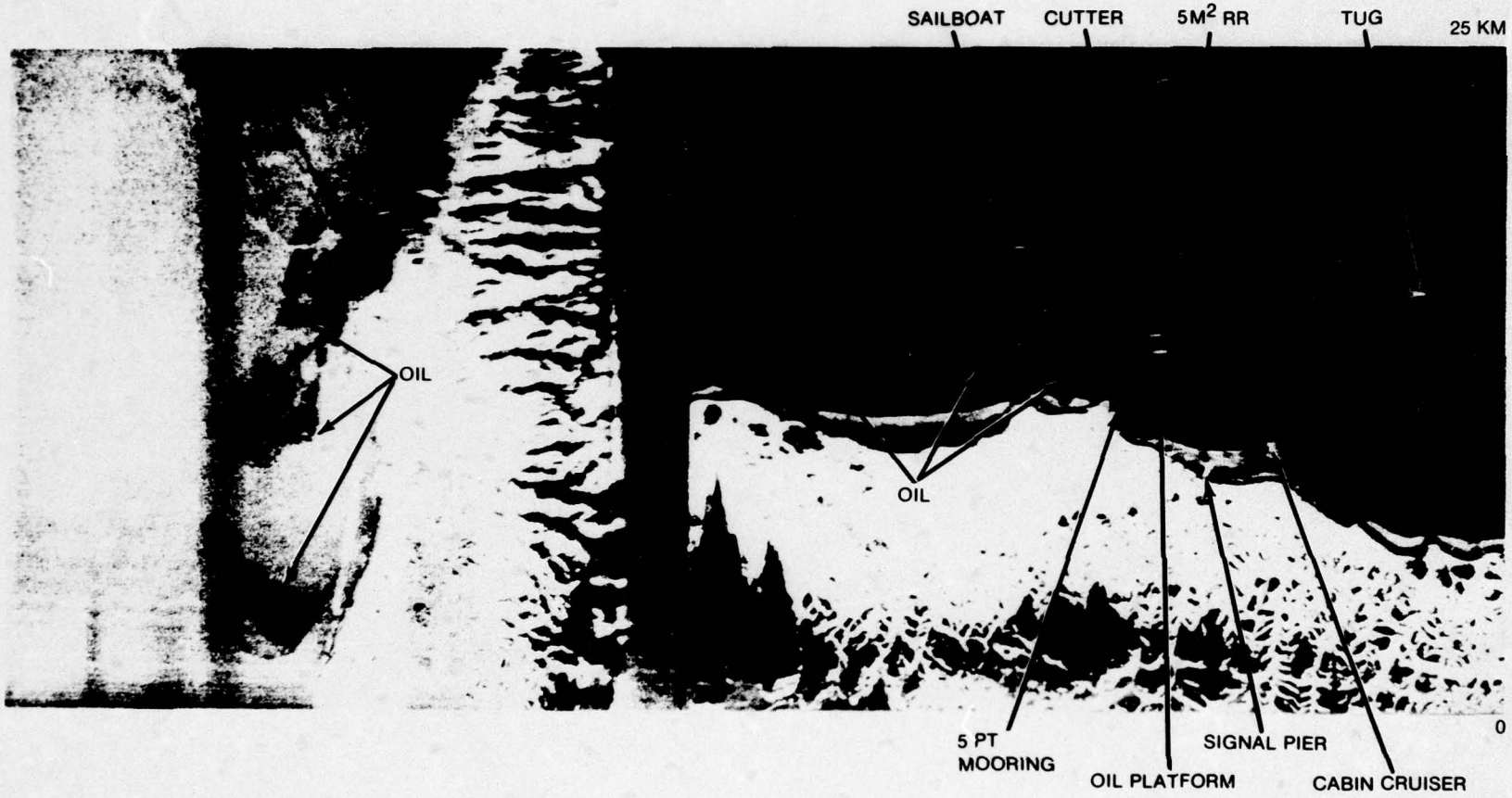

RUN 3

LAND MODE
ALT - 5500'
HEADING - 185°

RUN 2

OVERWATER MODE
ALT - 5500'
HEADING - 093°

76-3357

1815-42

E-7. COR, Runs 2 and 3, 5/19

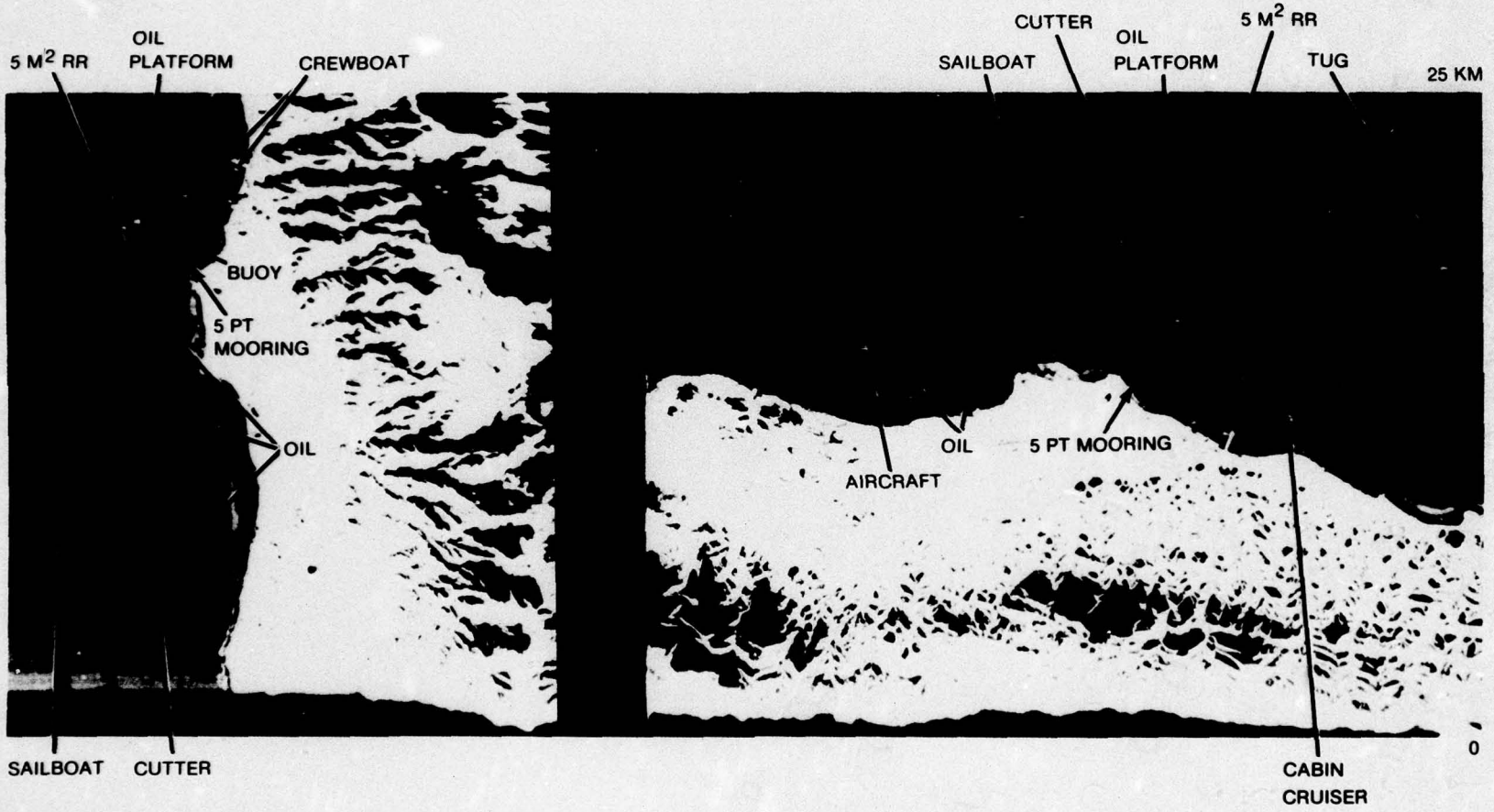

E-8. AN/APS-94D, Runs 2 and 3, 5/19

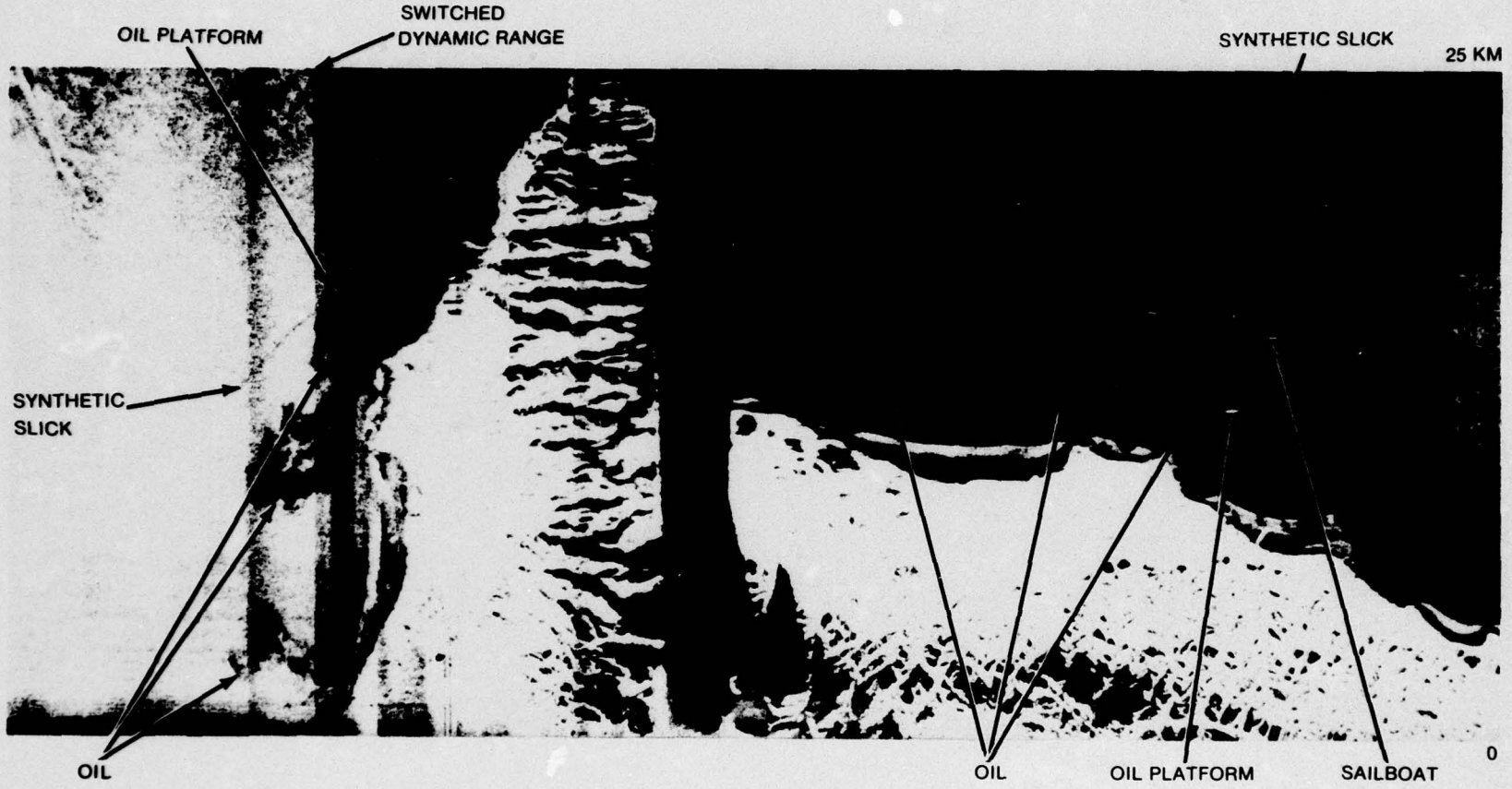

RUN 7

LAND MODE (1 LOOK)
ALT - 5500'
HEADING - 178°

76-3359

RUN 6

OVER WATER MODE
ALT - 5500'
HEADING - 093°

1815-33

E-9. COR, Runs 6 and 7, 5/19

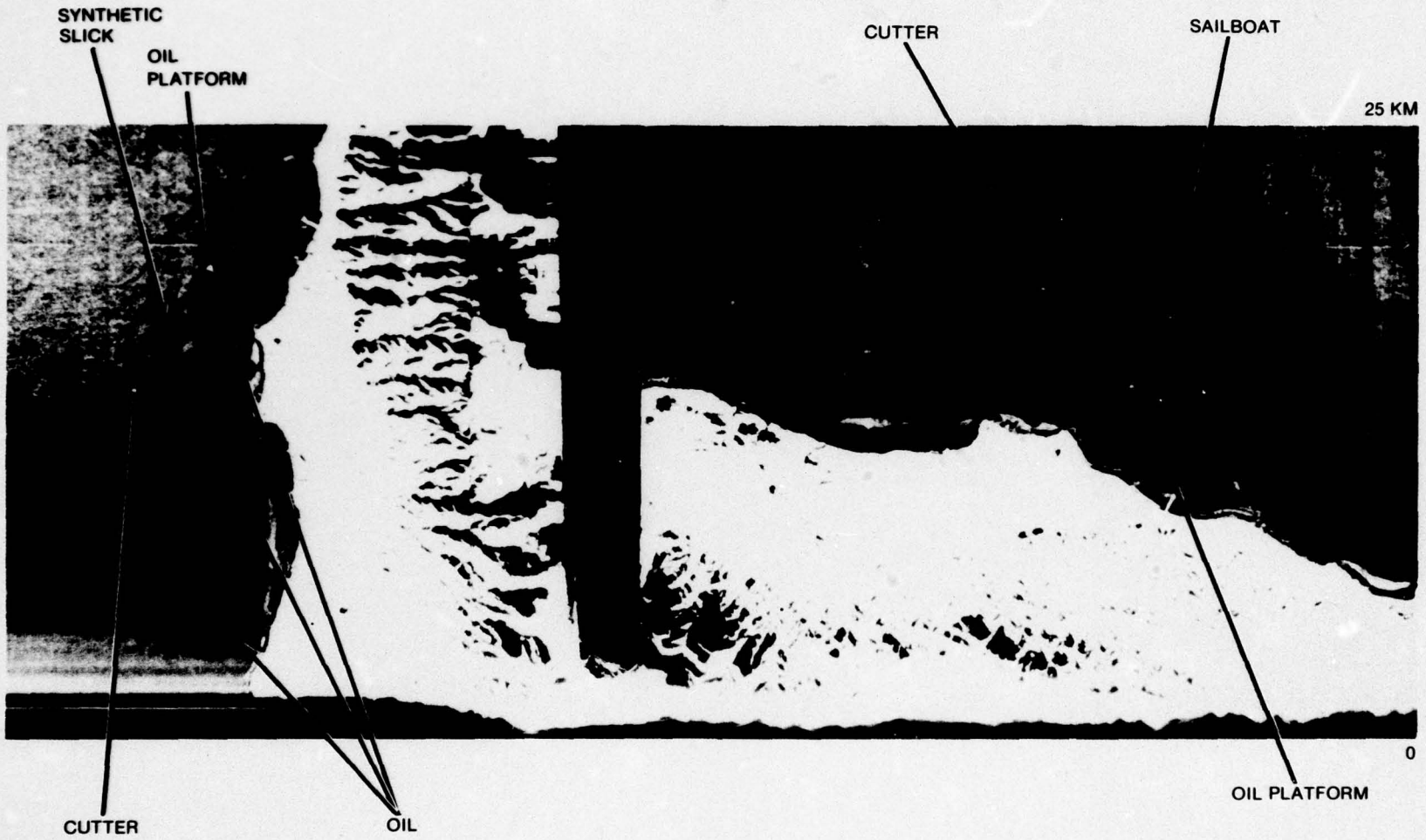

RUN 7

ALT - 6500'
HEADING - 178°

RUN 6

ALT - 6500'
HEADING - 090°

76-3360

1815-39

E-10. AN/APS-94D, Runs 6 and 7, 5/19

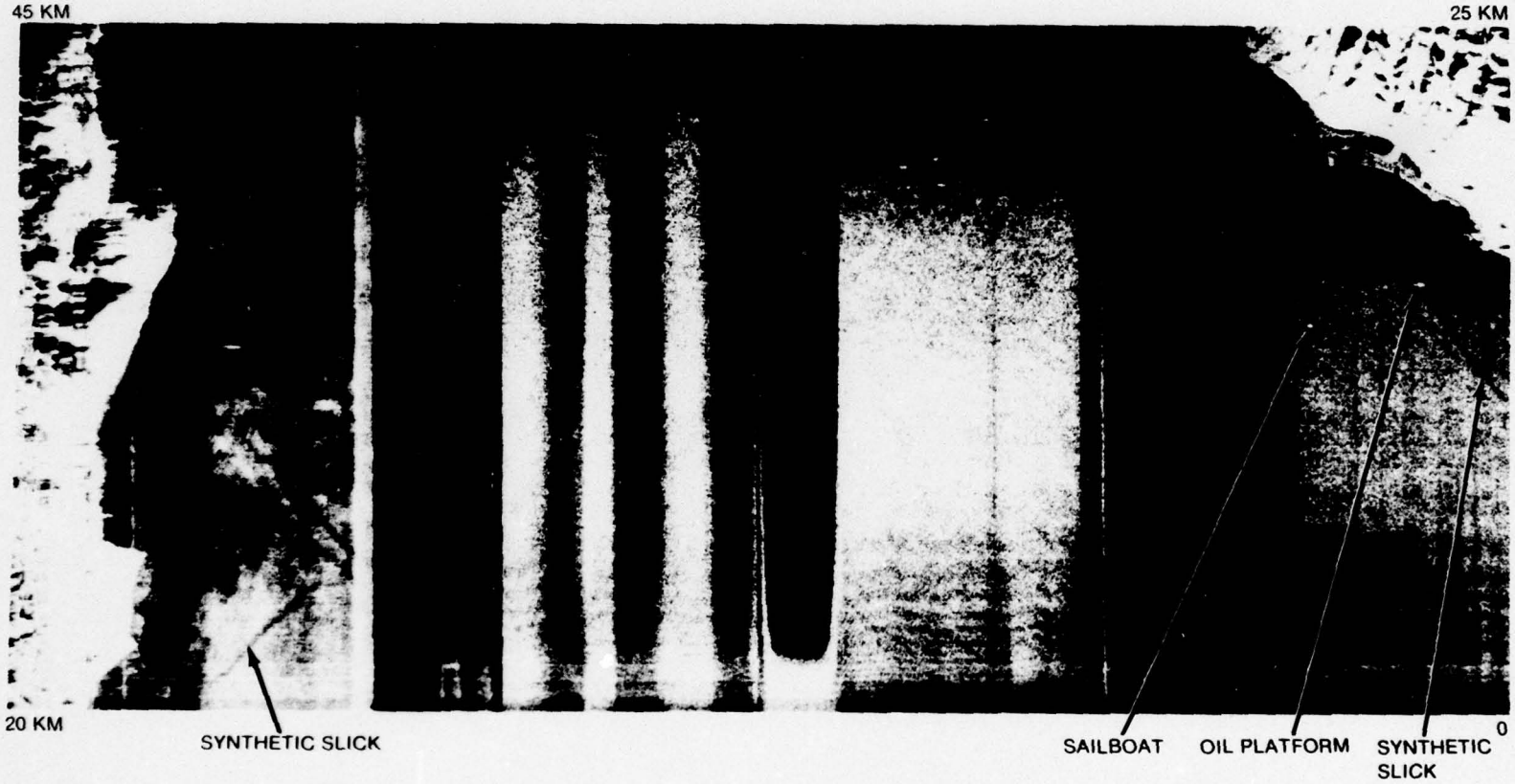

RUN 9

LAND MODE (3 LOOK)
ALT - 5500'
HEADING - 360°

RUN 8

LAND MODE (1 LOOK)
ALT - 5500'
HEADING - 270°

76-3361

E-11. COR, Runs 8 and 9, 5/19

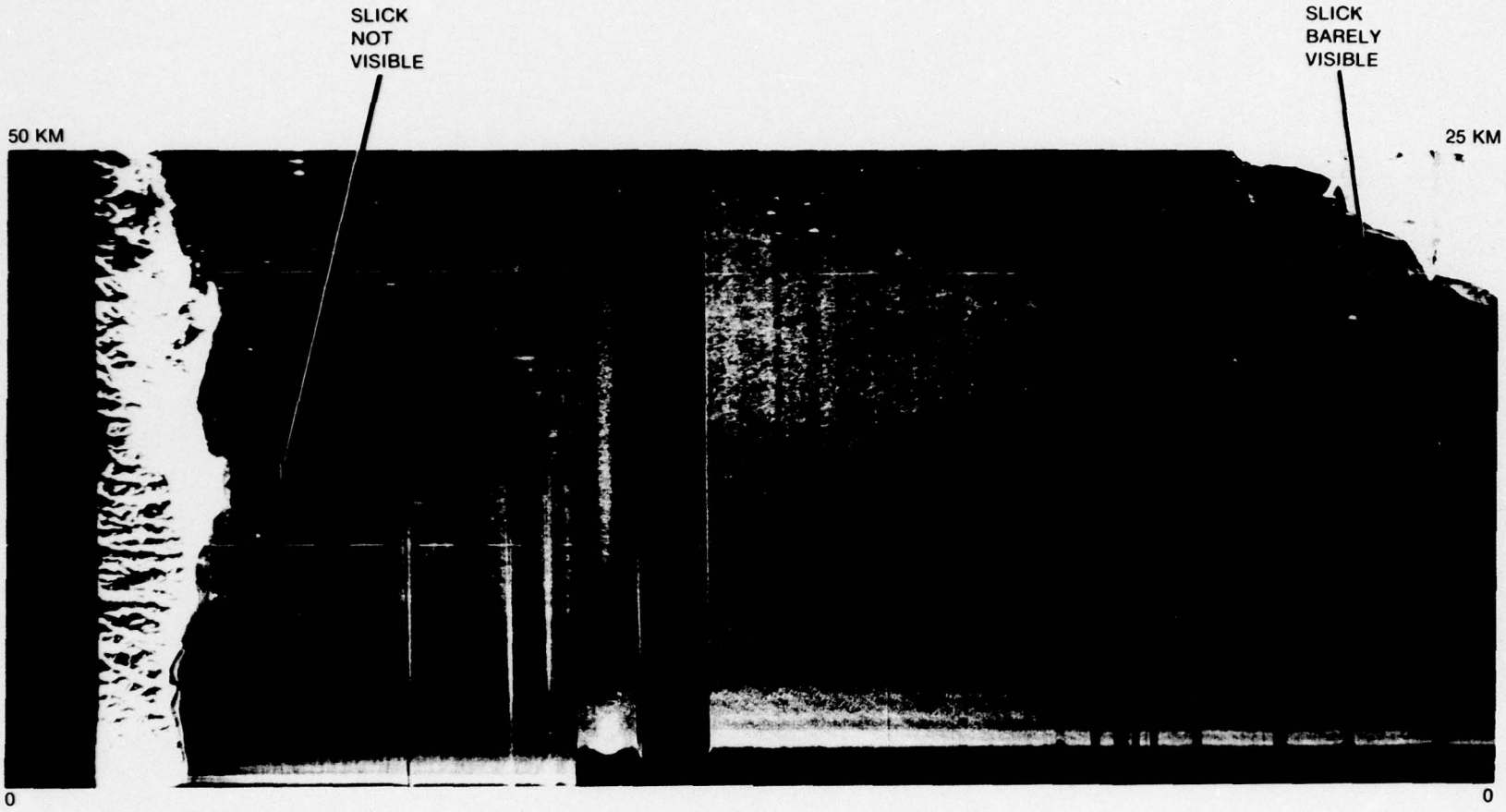

E-12. AN/APS-94D, Runs 8 and 9, 5/19

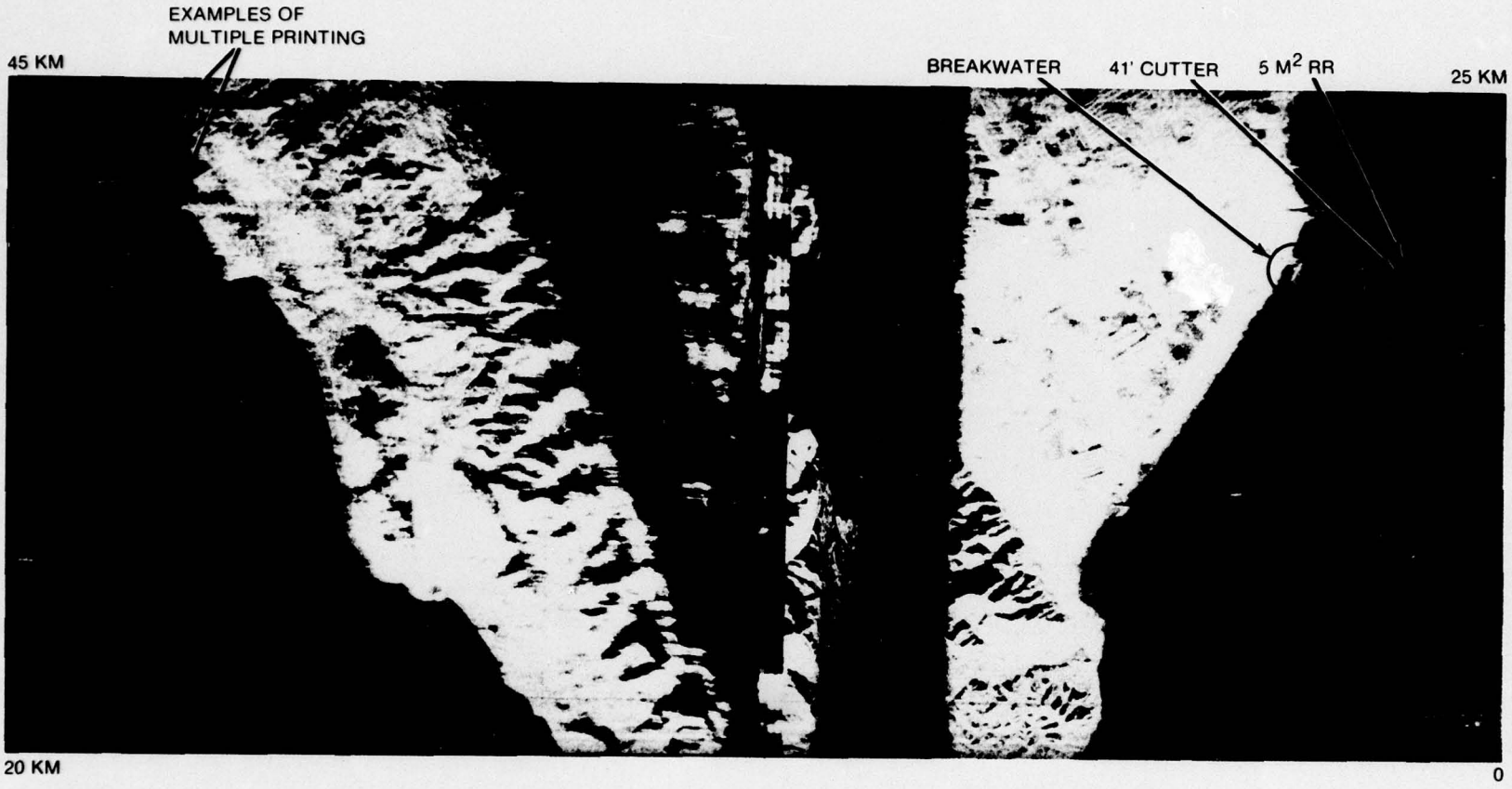

RUN 4

SANTA BARBARA
OVERWATER MODE
ALT - 5500'
HEADING - 216°

RUN 3

PORT HUENEME
OVERWATER MODE
ALT - 5500'
HEADING - 033°

76-3363

E-13. COR, Runs 3 and 4, 5/21

1815-36

RUN 17

OVERWATER MODE
ALT - 5500'
HEADING - 175°

RUN 16

OVERWATER MODE
ALT - 5500'
HEADING - 002°

76-3364

1815-40

E-14. COR, Morro Bay, 5/21

(31 JULY 1974, MIDAFTERNOON, 2 FT SWELL, WIND <6 KNOTS,
SOLID UNDERCAST EAST OF COAL OIL PT. CLEARING TO WEST)

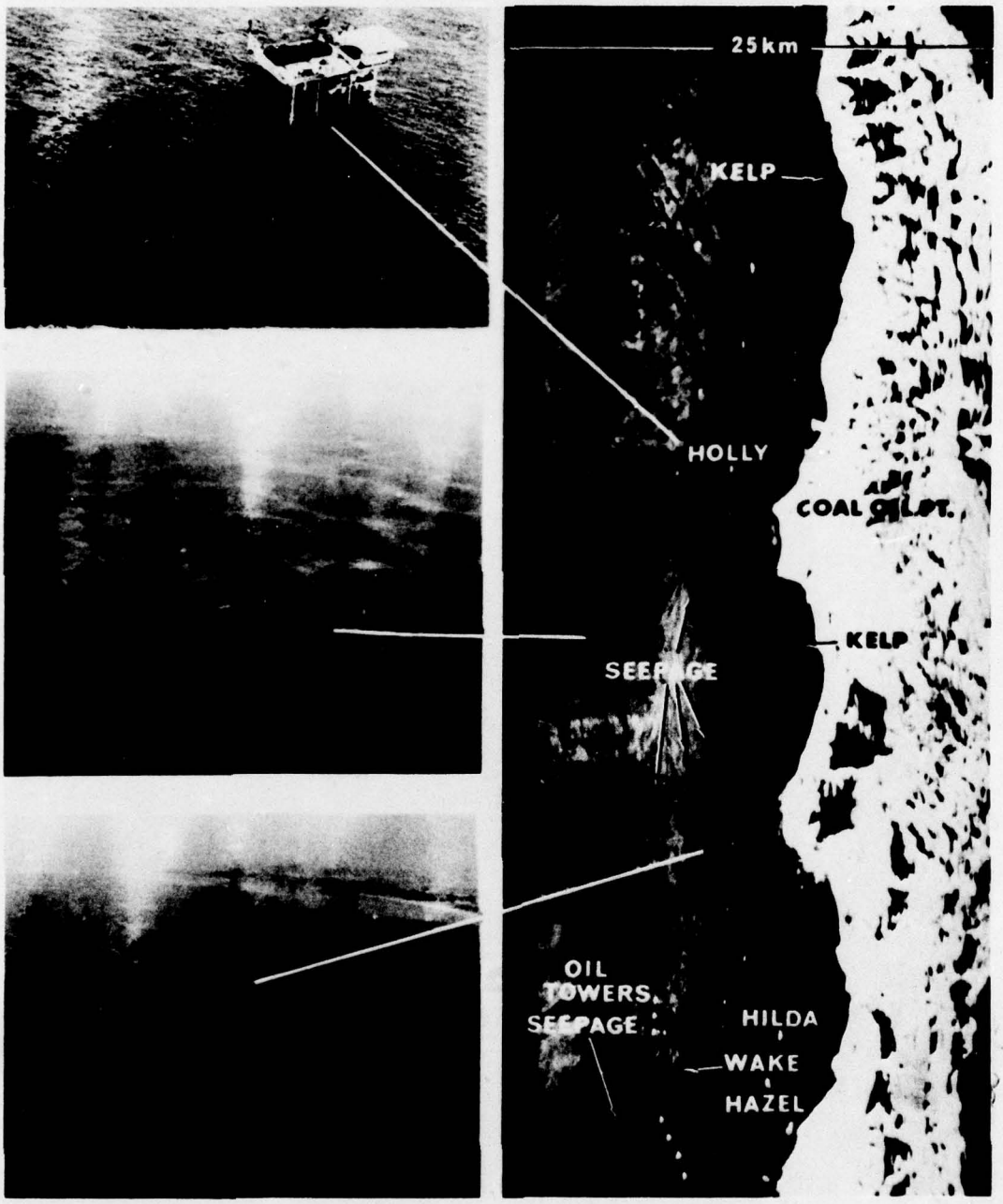

Figure E-15.

OSDR Radar Image and Conventional Photographs of Santa Barbara Coastal Waters.

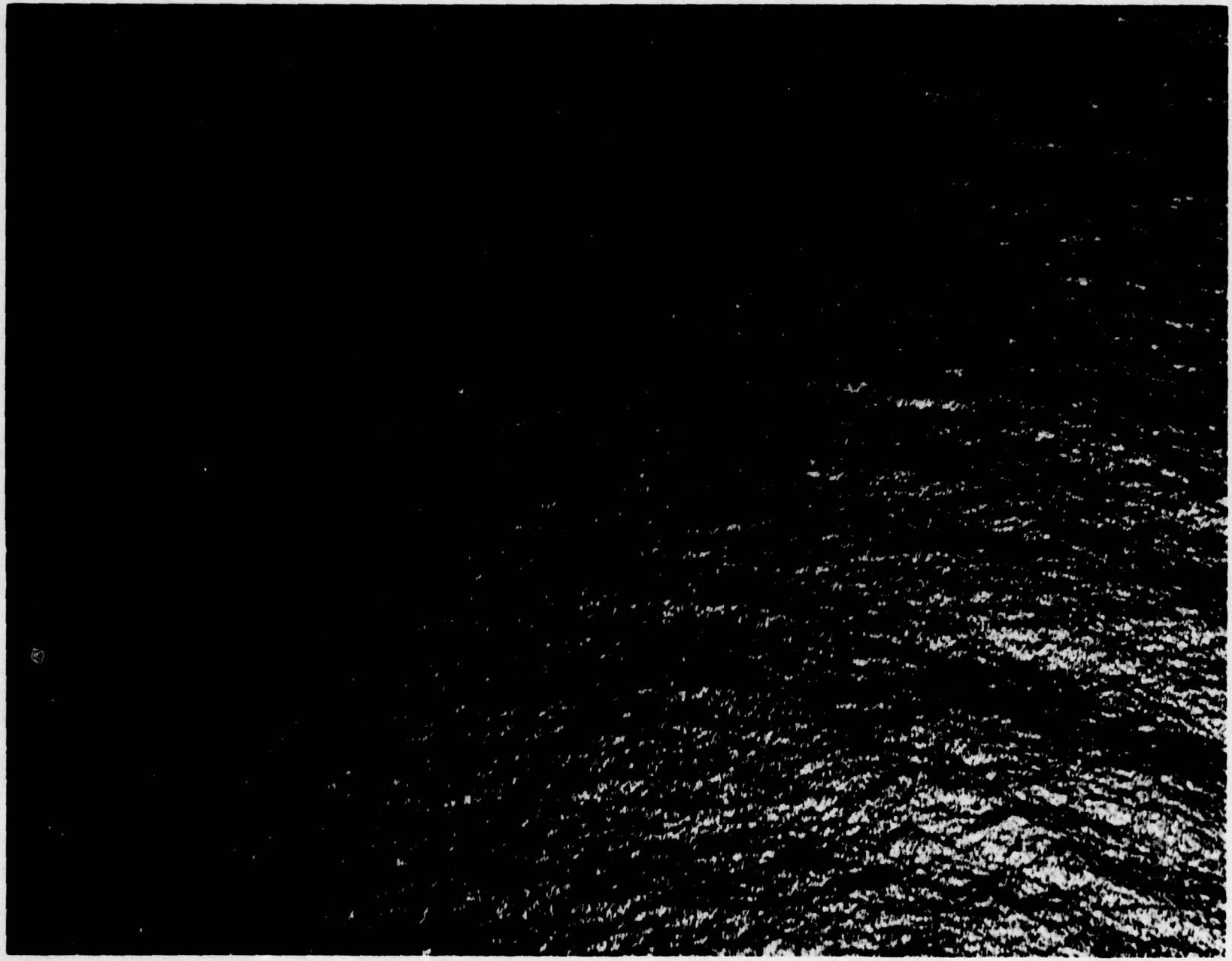

Figure E-16. Synthetic Oil Spill

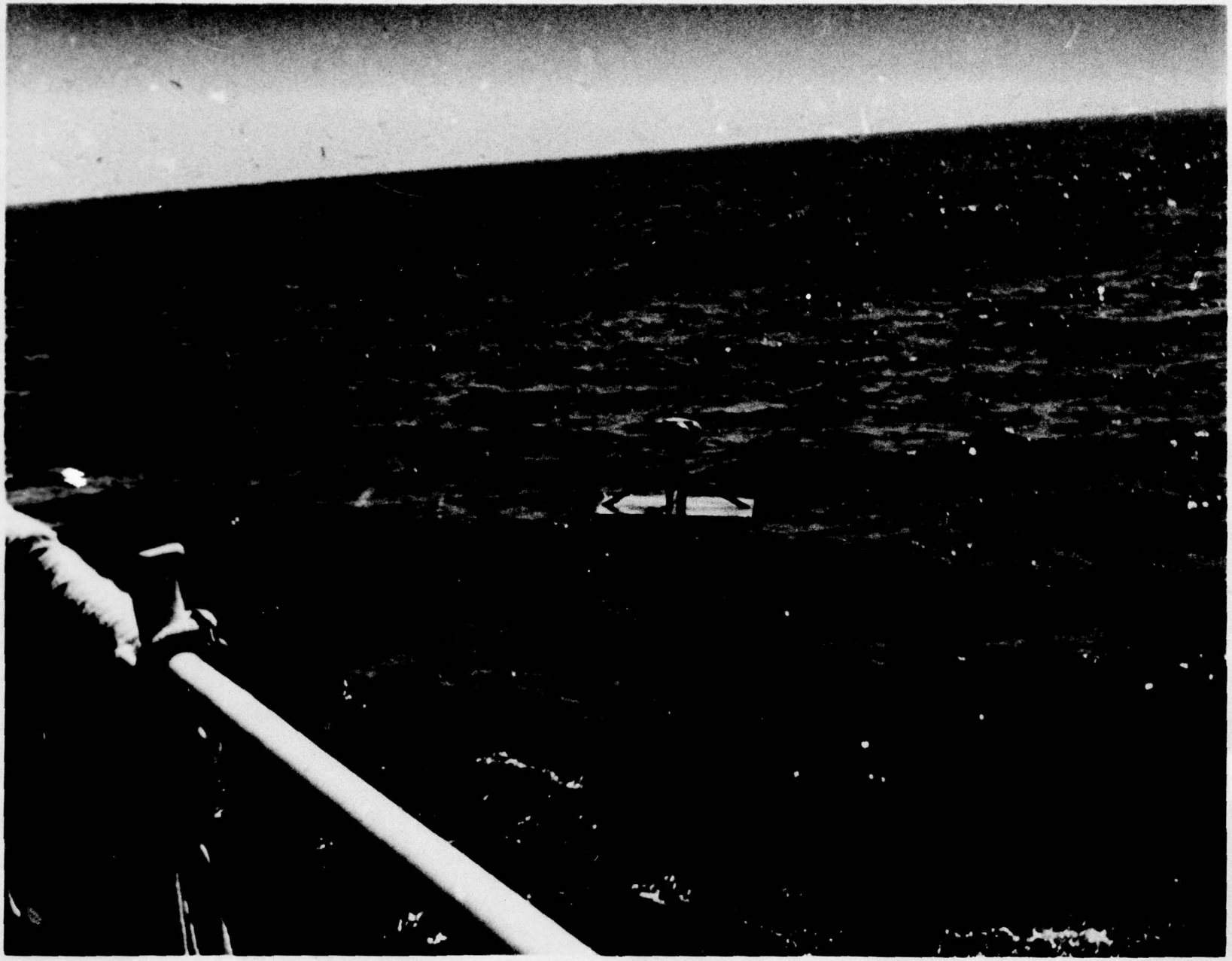

Figure E-17. $5M^2$ Radar Reflector

MOTOROLA

Figure E-18. Synthetic Oil Slick, Sea Level View

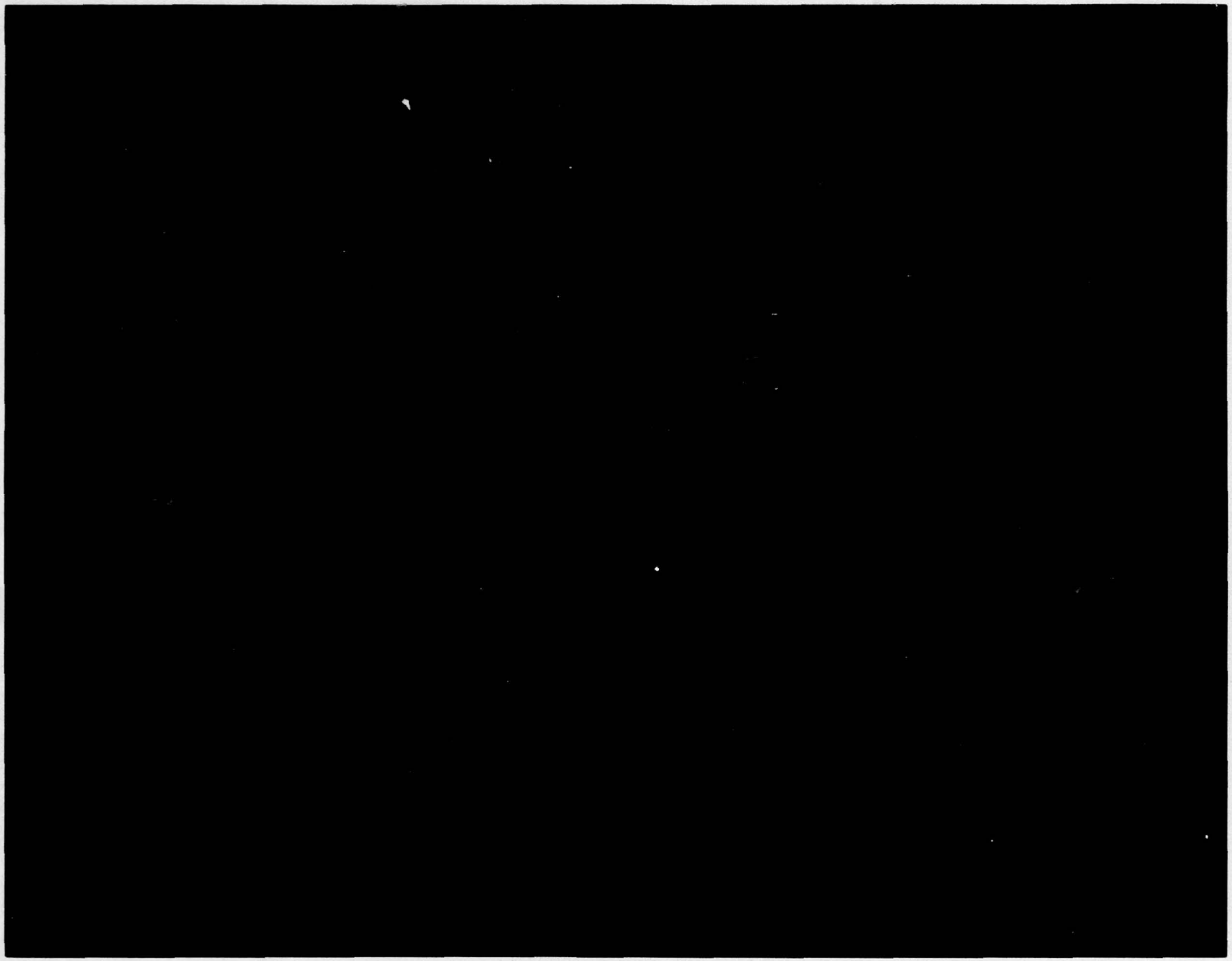

Figure E-19. Synthetic Oil Slick, Aircraft View